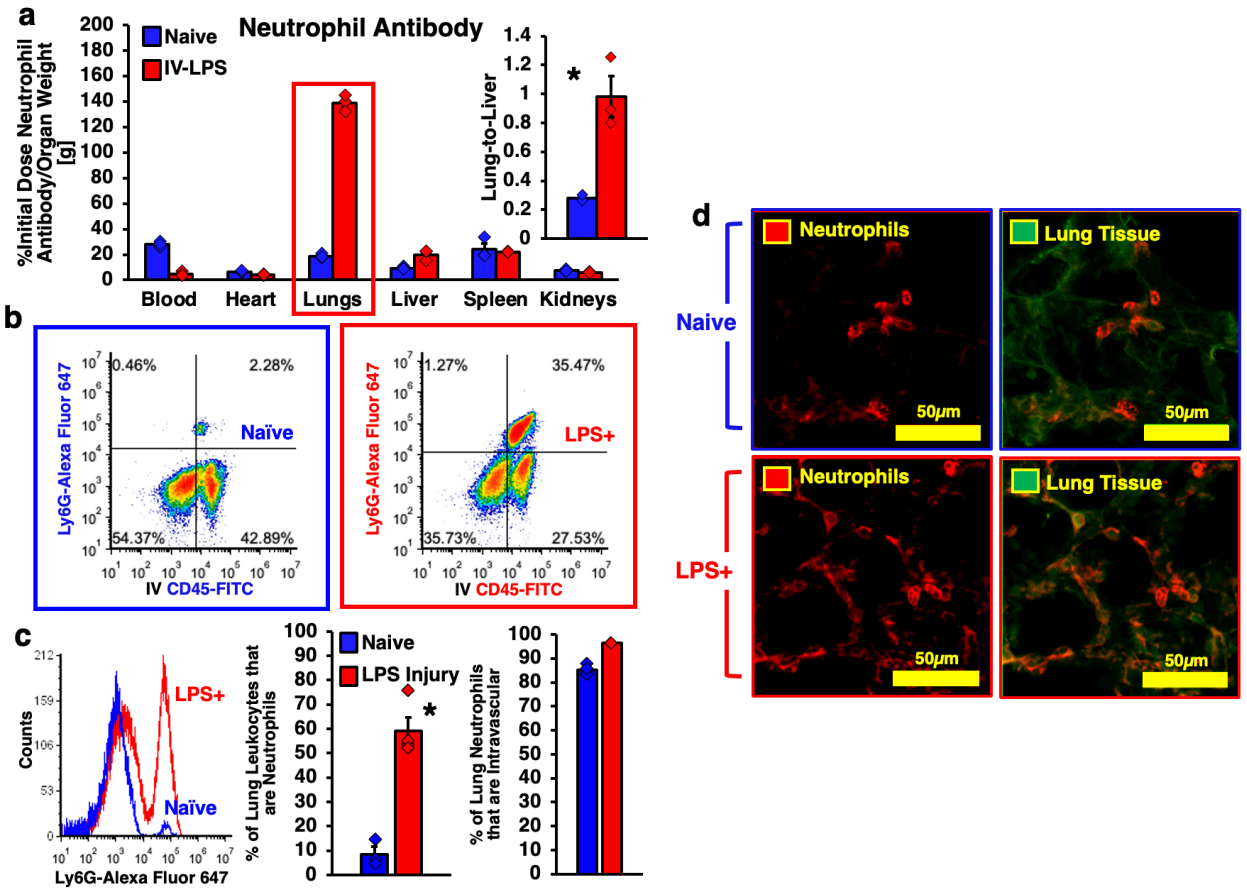

Supplementary Figure 1

Neutrophil Accumulation in Acutely Inflamed Pulmonary Vasculature. This data provides quantitative evidence that large numbers of neutrophils accumulate inside pulmonary blood vessels in the inflammation model chosen for our studies, and provides a basis for quantitative comparison between neutrophil accumulation in lung vasculature and nanoparticle accumulation in lung vasculature. (a) Biodistributions of intravenous radiolabeled anti-Ly6G antibody in naïve (n=3 animals) and IV-LPS-injured (n=3 animals) male C57BL/6 mice (*red box: $p<1x10^{-10}$, *: $p=0.037$*). Agreeing with previous studies addressing the role of neutrophils in systemic inflammation, the biodistribution of anti-Ly6G antibody indicated that systemic LPS injury profoundly increased the concentration of neutrophils in the lungs.[1–4] (b-c) Flow cytometric characterization of single cell suspensions prepared from naïve and IV-LPS-injured injured mouse lungs. (b) Vertical axis indicates anti-Ly6G staining for neutrophils and horizontal axis indicates stain induced by intravenous anti-CD45 antibody. (c) Flow cytometry data indicating increased neutrophil concentration in IV-LPS-injured mouse lungs, compared to naïve lungs, and correlation of *intravenous* leukocyte staining with neutrophils (n=3 animals for both naïve and LPS groups, **: p=0.00001*). Comparison to non-intravenous anti-CD45 staining indicated intravascular vs. extravascular populations. The presence of large populations of intravascular neutrophils following inflammatory injury is consistent with previously published observations.[1–5] (d) Fluorescence micrographs indicating increased concentration of neutrophils in IV-LPS-injured mouse lungs. Red: anti-Ly6G

stain. Green: tissue autofluorescence. Histology data reflect lungs from two naïve mice and two IV-LPS-affected mice. Statements of statistical significance are based on two-way ANOVA with Sidak's multiple comparisons test. All error bars indicate mean ± SEM.

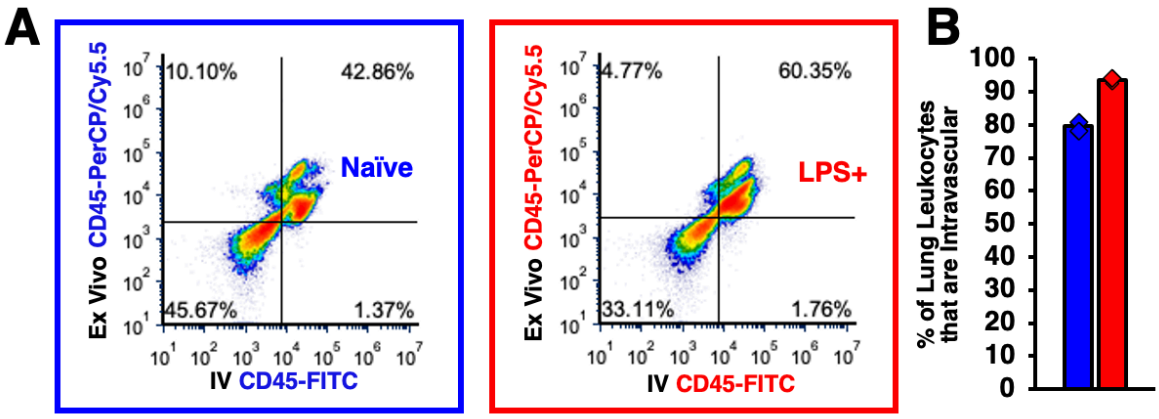

Supplementary Figure 2

Intravenous vs. Total Leukocyte Stains of Single Cell Suspensions Prepared from Mouse Lungs. (a) Fluorescence generated by anti-CD45 staining of single cell suspensions, distinguishing leukocytes in single cell suspensions, plotted against fluorescence generated by an intravenous labeled CD45 antibody, administered five minutes prior to sacrifice and lung removal to stain *intravenous* leukocytes. (b) With gates set by the quadrants delineated in (a), correlation between intravenous CD45 staining and staining of total cell populations indicated the percentage of leukocytes that were intravascular. In naïve mice (n=3 animals), ~80% of leukocytes were intravascular. In IV LPS-challenged mice (n=3 animals), ~95% of leukocytes were intravascular. Error bars indicate mean ± SEM.

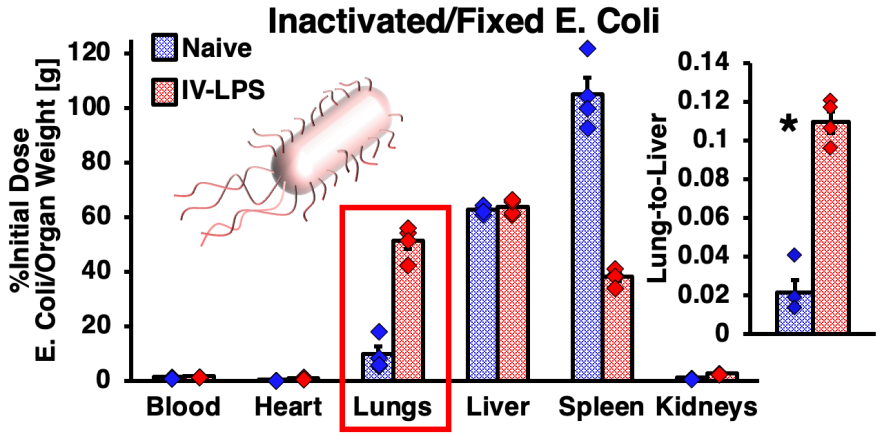

Supplementary Figure 3

Biodistributions of heat-inactivated, fixed, and ^{125}I-labeled E. coli in naïve and IV-LPS-injured mice. Previous work has traced the neutrophil response to bacteria in the lungs, determining that pulmonary neutrophils pursue and engulf active bacteria following either intravenous infection or infection of the airspace in the lungs.[4,6,7] In contrast to

studies with live bacteria described in the literature, we injected heat-inactivated, oxidized, and fixed *E. coli* in naïve (n=4 animals) and IV-LPS-injured (n=4 animals) mice. With the bacteria stripped of their functional behavior, *E. coli* did not accumulate in the lungs of naïve control mice. However, pre-treatment with LPS to recapitulate the inflammatory response to infection led to enhanced accumulation of the deactivated *E. coli* in the lungs (*red box: $p<1x10^{-10}$, *: p=0.00005)*. Statements of statistical significance are based on two-way ANOVA with Sidak's multiple comparisons test. All error bars indicate mean ± SEM.

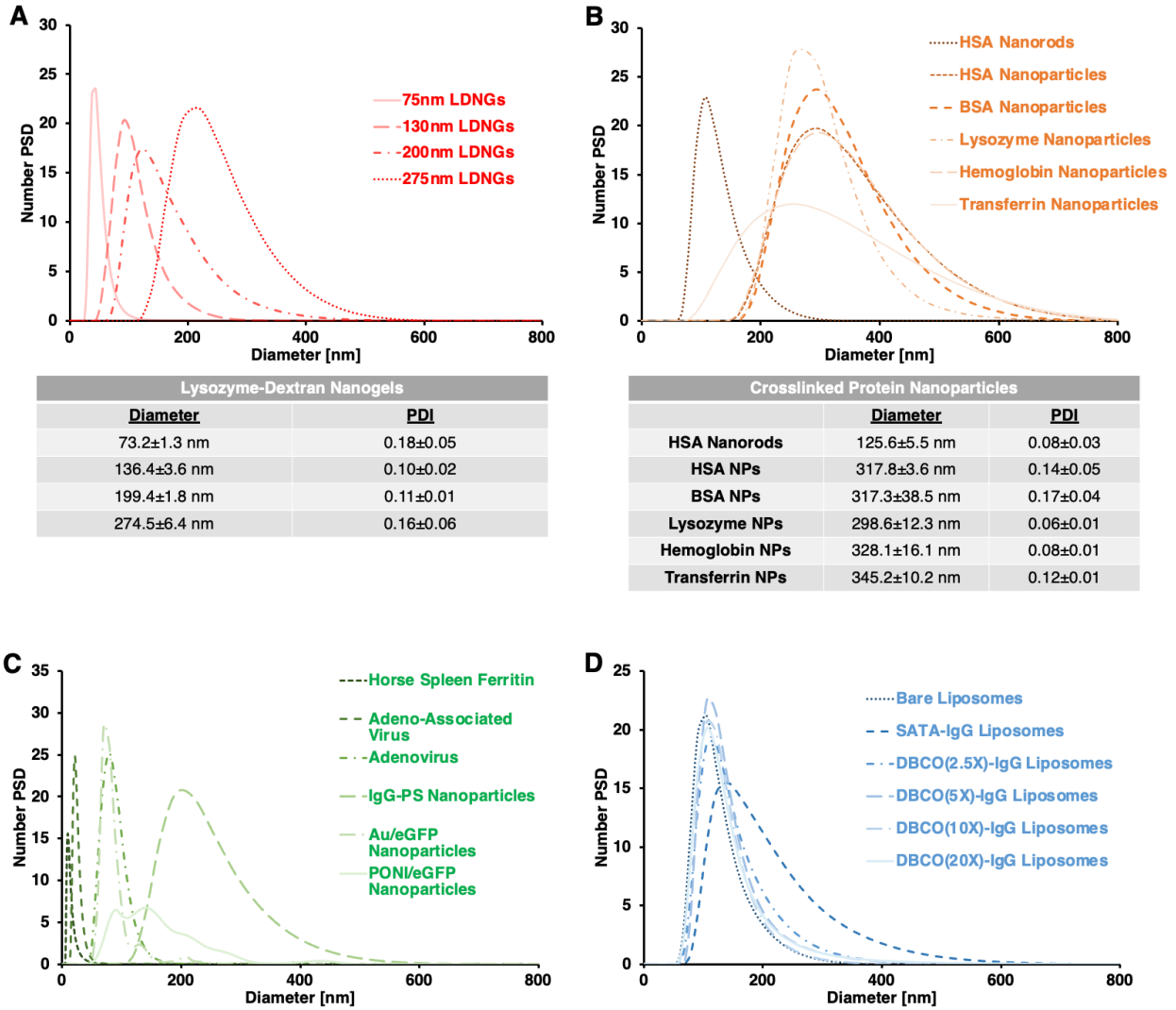

Lysozyme-Dextran Nanogels	
Diameter	**PDI**
73.2±1.3 nm	0.18±0.05
136.4±3.6 nm	0.10±0.02
199.4±1.8 nm	0.11±0.01
274.5±6.4 nm	0.16±0.06

Crosslinked Protein Nanoparticles		
	Diameter	**PDI**
HSA Nanorods	125.6±5.5 nm	0.08±0.03
HSA NPs	317.8±3.6 nm	0.14±0.05
BSA NPs	317.3±38.5 nm	0.17±0.04
Lysozyme NPs	298.6±12.3 nm	0.06±0.01
Hemoglobin NPs	328.1±16.1 nm	0.08±0.01
Transferrin NPs	345.2±10.2 nm	0.12±0.01

Miscellaneous		
	Diameter	**PDI**
Horse Spleen Ferritin	12.0±0.3 nm	0.05±0.00
Adeno-Associated Virus	23.2±1.0 nm	0.01±0.00
Adenovirus	82.5±10.7 nm	0.03±0.01
IgG-Polystyrene NPs	230.5±2.8 nm	0.14±0.01
Au/eGFP NPs	88.9±1.6 nm	0.13±0.04
PONI/eGFP NPs	158.9±6.2 nm	0.17±0.02

Liposomes		
	Diameter	**PDI**
Bare Liposomes	103.6±8.7 nm	0.09±0.01
SATA-IgG Liposomes	178.7±6.9 nm	0.23±0.03
DBCO(2.5X)-IgG Lip.	136.6±5.7 nm	0.16±0.03
DBCO(5X)-IgG Lip.	133.0±0.2 nm	0.14±0.01
DBCO(10X)-IgG Lip.	122.9±7.6 nm	0.08±0.01
DBCO(20X)-IgG Lip.	128.2±4.3 nm	0.17±0.03

Supplementary Figure 4

Dynamic Light Scattering or Nanosight Characterization of Tested Nanoparticles. (a) Size measurements of lysozyme-dextran nanogel variants (LDNGs). Nanogels with 2:1 mol:mol rhodamine-dextran:lysozyme composition had a diameter of 73.2±1.3 nm, PDI 0.18±0.05. Nanogels with 1:1 mol:mol rhodamine-dextran:lysozyme composition had a diameter of 136.4±3.6 nm, PDI 0.10±0.02. Nanogels with 1:1 mol:mol FITC-dextran:lysozyme composition had a diameter of 199.4±1.8 nm, PDI 0.11±0.01. Nanogels with 1:1 mol:mol rhodamine-dextran:lysozyme composition, formed at pH 10.70, had a diameter of 274.5±6.4 nm, PDI 0.16±0.06. (b) Size measurements of crosslinked protein nanoparticle variants. Nanoparticles or nanorods were formed via co-jetting of PEG-NHS-ester-crosslinker with human albumin, bovine albumin, hen lysozyme, human hemoglobin, or human transferring. (d) Size measurements of other nanoparticles used in the study. Naturally occurring horse spleen ferritin, adeno-associated virus, and adenovirus diameters were confirmed by DLS. Horse spleen ferritin had a diameter of 12.0±0.4 nm, PDI 0.05±0.00. Adeno-associated virus (serotype 8) had a diameter of 23.2±1.0 nm, PDI 0.01±0.00. Adenovirus had a diameter of 82.5±10.7 nm, PDI 0.03±0.01. Carboxylated polystyrene nanoparticles (initial diameter ~150nm) were conjugated to IgG via EDCI-mediated carboxy-amine reaction, yielding particles with diameter of 230.5±2.8 nm, PDI 0.14±0.01. Polyglutamate-tagged green fluorescent protein (eGFP) was combined with arginine-tagged gold nanoclusters (Au) or arginine-poly(oxanorborneneimide) (PONI), forming particles with diameter, as assessed by nanoparticle tracking analysis, of 88.9±1.6 nm (PDI 0.14±0.04) for Au-eGFP and 158.9±6.2 (PDI 0.17±0.03) for PONI-eGFP. (c) Size measurements of variant liposome formulations. Bare liposomes had a diameter of 103.6±8.7 nm, PDI 0.09±0.01. Maleimide liposomes conjugated to SATA-functionalized IgG had a diameter of 176.8±6.9 nm, PDI 0.23±0.03. Azide-presenting liposomes conjugated to DBCO-functionalized IgG had diameters of approximately 130nm, with small variations registered for different DBCO densities on IgG.

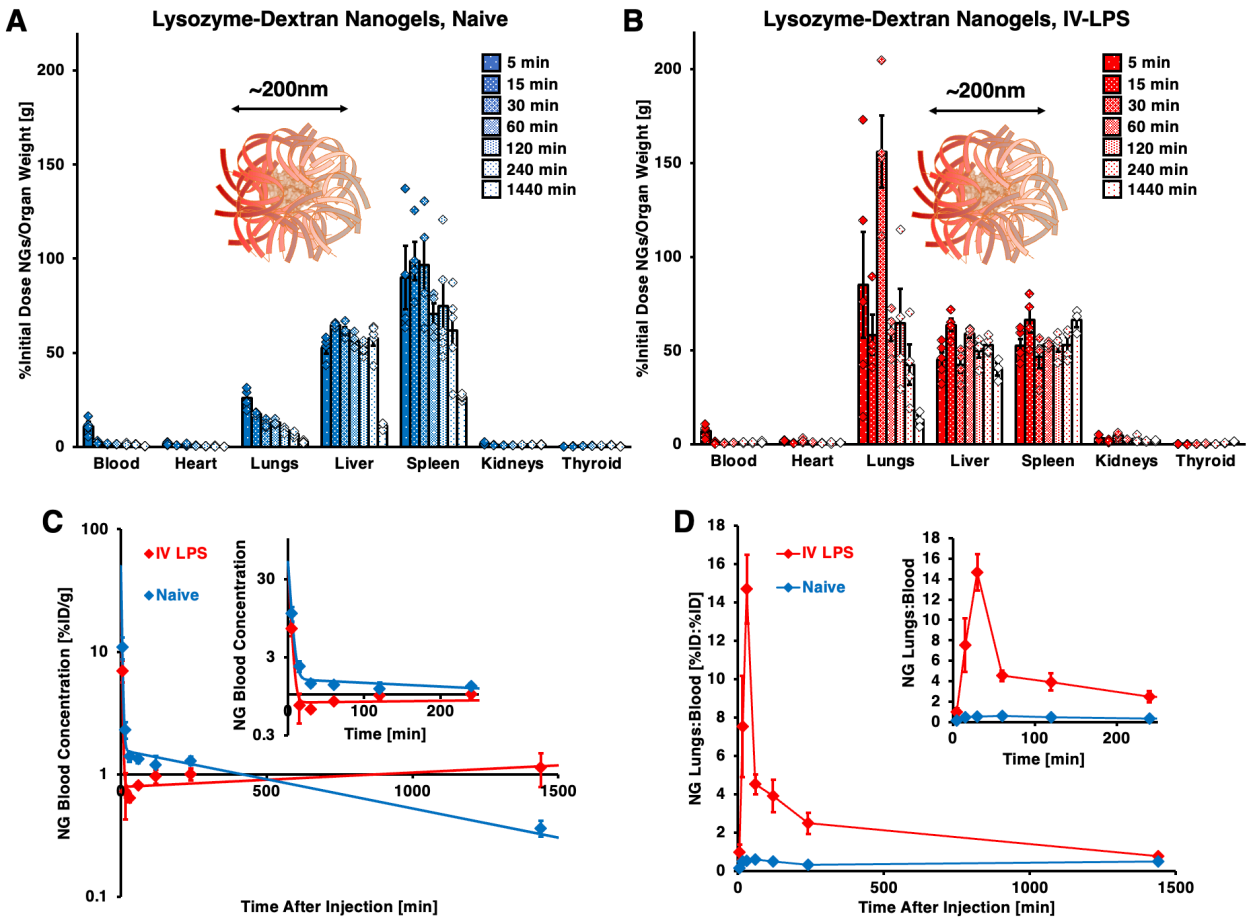

Supplementary Figure 5

Pharmacokinetics of Lysozyme-Dextran Nanogels in Naïve and IV-LPS-Injured Mice. Lysozyme-dextran nanogel (NGs) pharmacokinetics were evaluated in naïve and IV-LPS-injured mice. NG biodistributions were determined for naïve (a) and IV-LPS-challenged (b) mice at 5 (n=4 animals naïve, n=5 animals IV-LPS), 15 (n=4 animals naïve, n=4 animals IV-LPS), 30 (n=4 animals naïve, n=4 animals IV-LPS), 60 (n=4 animals naïve, n=4 animals IV-LPS), 120 (n=5 animals naïve, n=4 animals IV-LPS), 240 (n=5 animals naïve, n=4 animals IV-LPS), and 1440 minutes (n=5 animals naïve, n=3 animals IV-LPS) after bolus NG injection. (c) Log-linear representation of NG clearance from the blood over 24 hours after injection (inset: 0-4 hour clearance data) indicating rapid clearance in both naïve and LPS-challenged mice, with blood levels of NGs being lower in LPS-challenged mice between 0 and 4 hours after injection, but greater in LPS-challenged mice at 24 hours after injection. (d) NG lung uptake:blood level ratio in naïve and LPS-challenged mice. Lungs:blood metric reaches a clear peak at 30 minutes after nanogel injection in LPS-injured mice (inset: 0-4 hour lungs:blood data), matching a peak measured by absolute level of lung uptake. All error bars indicate mean ± SEM.

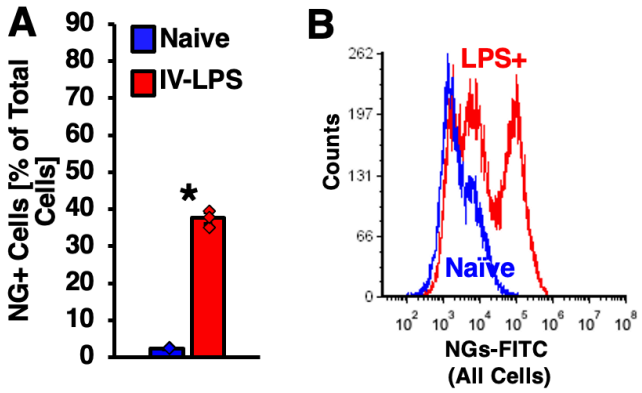

Supplementary Figure 6

Flow Cytometric Characterization of Lysozyme-Dextran Nanogel Uptake in Naïve and Inflamed Lungs. (a) Fluorescence from FITC-labeled NGs was measured in single cell suspensions prepared from mouse lungs harvested after 30 minutes nanogel circulation. With gates set as depicted in main text figure 1d, the number of cells positive for NG fluorescence increased between naïve (n=3 animals) and LPS-challenged lungs (n=3 animals, **: p=0.0001)*. (b) Likewise, a population of high-fluorescence cells was detected in IV LPS-challenged lungs, but not naïve lungs. Statistical significance is based on unpaired t-test. All error bars indicate mean ± SEM.

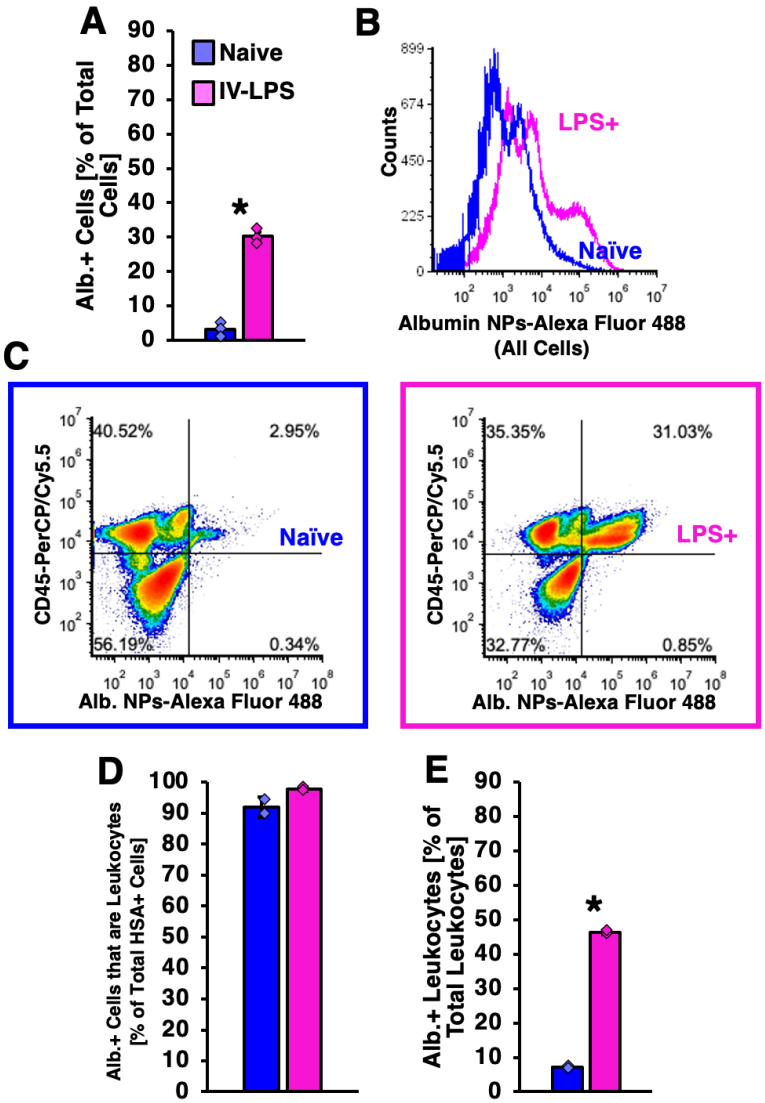

Supplementary Figure 7

Flow Cytometric Characterization of Crosslinked Albumin Nanoparticle Uptake in Leukocytes in Naïve and Inflamed Lungs. (a) Fluorescence from Alexa Fluor 488-labeled crosslinked albumin nanoparticles was measured in single cell suspensions prepared from mouse lungs harvested after 30 minutes nanoparticle circulation. With gates set as depicted in main text figure 1e, the number of cells positive for albumin nanoparticle fluorescence increased between naïve (n=3 animals) and LPS-challenged lungs (n=3 animals, **: $p=2.5x10^{-10}$*). (b) A population of high-fluorescence cells was detected in IV LPS-challenged lungs, but not naïve lungs. (c) Fluorescence generated by anti-CD45 staining, distinguishing leukocytes in single cell suspensions, plotted against human albumin nanoparticle fluorescence in single cell suspensions prepared from naïve and IV LPS-challenged lungs. (d) With gates set by the quadrants delineated in (c), correlation between nanoparticle fluorescence and CD45 staining indicated the percentage of albumin nanoparticle-bearing cells that were leukocytes as >90% in both naïve (n=3 animals) and IV LPS-challenged (n=3 animals) lungs. (e) Similar analysis of the same samples indicated that the fraction of leukocytes containing albumin

nanoparticles increased in LPS-challenged vs. naïve lungs (**: p<1x10^{-10}*). Statements of statistical significance are based on two-way ANOVA with Sidak's multiple comparisons test. All error bars indicate mean ± SEM.

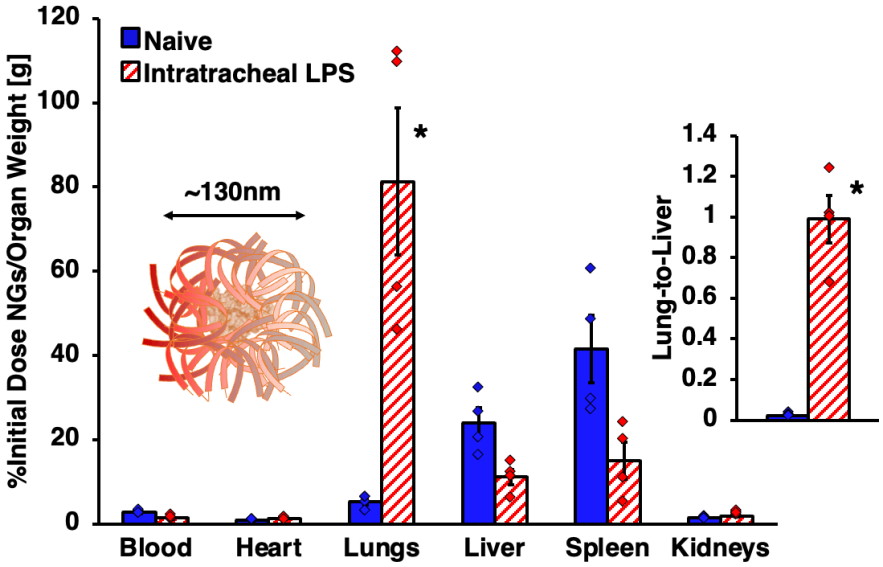

Supplementary Figure 8

Biodistributions of Lysozyme-Dextran Nanogels in Naïve and Intratracheal LPS-Injured Mice. As an alternative to intravenous LPS injection, mice were administered LPS via intratracheal (IT) instillation, prior to bolus dosing with NGs. As with IV LPS-injured mice, IT LPS injury led to dramatically increased pulmonary uptake of NGs (n=4 animals), along with depression in hepatic and splenic uptake, relative to values in naïve mice (**: p<1x10^{-10} for lungs, p=0.0002 for lung:liver ratio*). Statements of statistical significance are based on two-way ANOVA with Sidak's multiple comparisons test. All error bars indicate mean ± SEM.

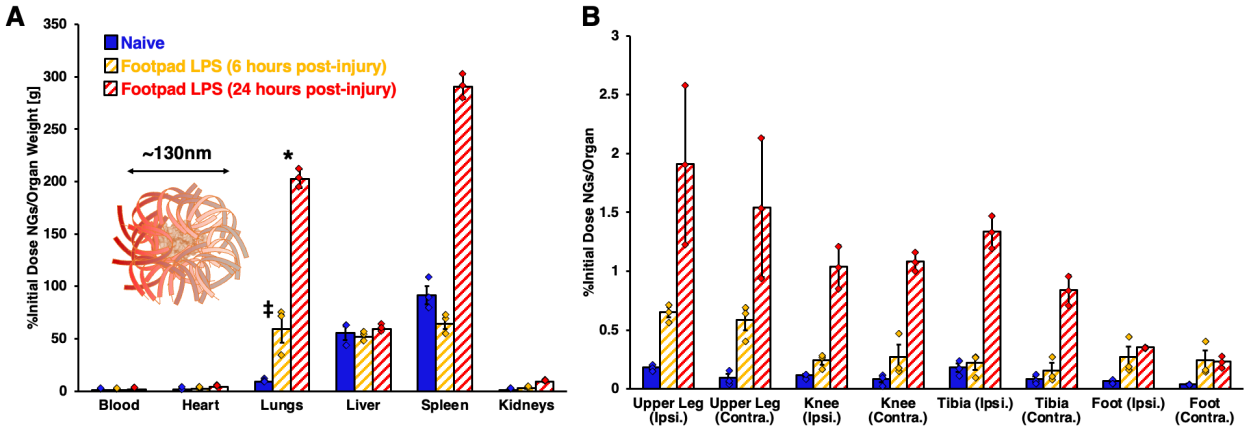

Supplementary Figure 9

Biodistributions of Lysozyme-Dextran Nanogels After Footpad Administration of LPS. As an additional mouse model for LPS-induced inflammation, LPS was dosed in the footpad, either 6 or 24 hours prior to dosing with NGs. NG uptake in the lungs, legs, and

feet increased with time after footpad LPS administration. Pulmonary uptake at both 6 (n=3 animals) and 24 hours (n=3 animals) after LPS was significantly increased relative to uptake in naïve mice (‡: $p=2.2x10^{-8}$, *: $p<1x10^{-10}$). No significant differences were noted in NG uptake in ipsilateral vs. contralateral legs. Statements of statistical significance are based on two-way ANOVA with Tukey's multiple comparisons test. All error bars indicate mean ± SEM.

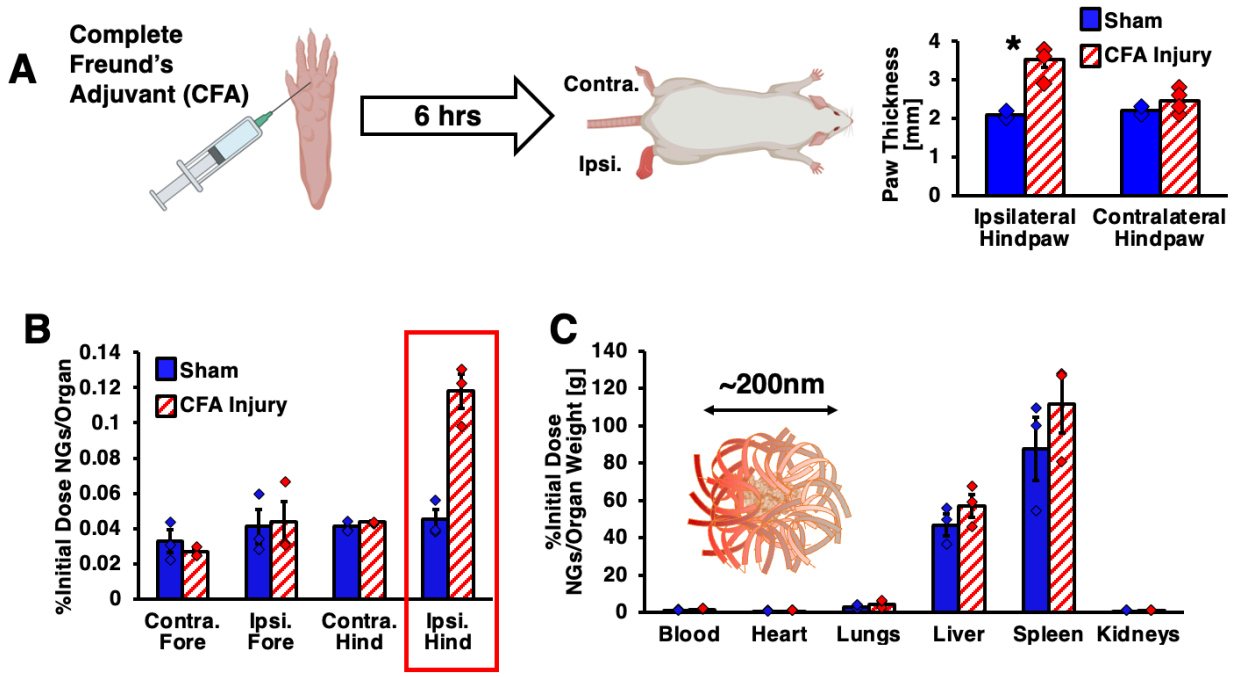

Supplementary Figure 10

Biodistributions of Lysozyme-Dextran Nanogels in A Localized Footpad Inflammation Model. (a) Complete Freund's adjuvant (CFA) was injected into one hindlimb footpad six hours prior to NG tracing experiments (Schematic created with BioRender.com). Inflammation in CFA-injected feet (n=4 animals) vs. sham-injected feet (n=3 animals) was evident via ~75% increase in ipsilateral lateral paw thickness. Contralateral paw thickness was unaffected (*: $p=0.002$). (bNGs were traced in mice with CFA-injected hind paw (n=3 animals) or sham-injected hind paw (n=3 animals). NGs accumulated in the injured hind paw at ~2.5-fold greater concentrations than in sham-injected and contralateral paws (*red box:* $p=8.8x10^{-6}$). (c) CFA induced no significant differences in nanogel accumulation in other organs. Statements of statistical significance are based on two-way ANOVA with Sidak's multiple comparisons test. All error bars indicate mean ± SEM.

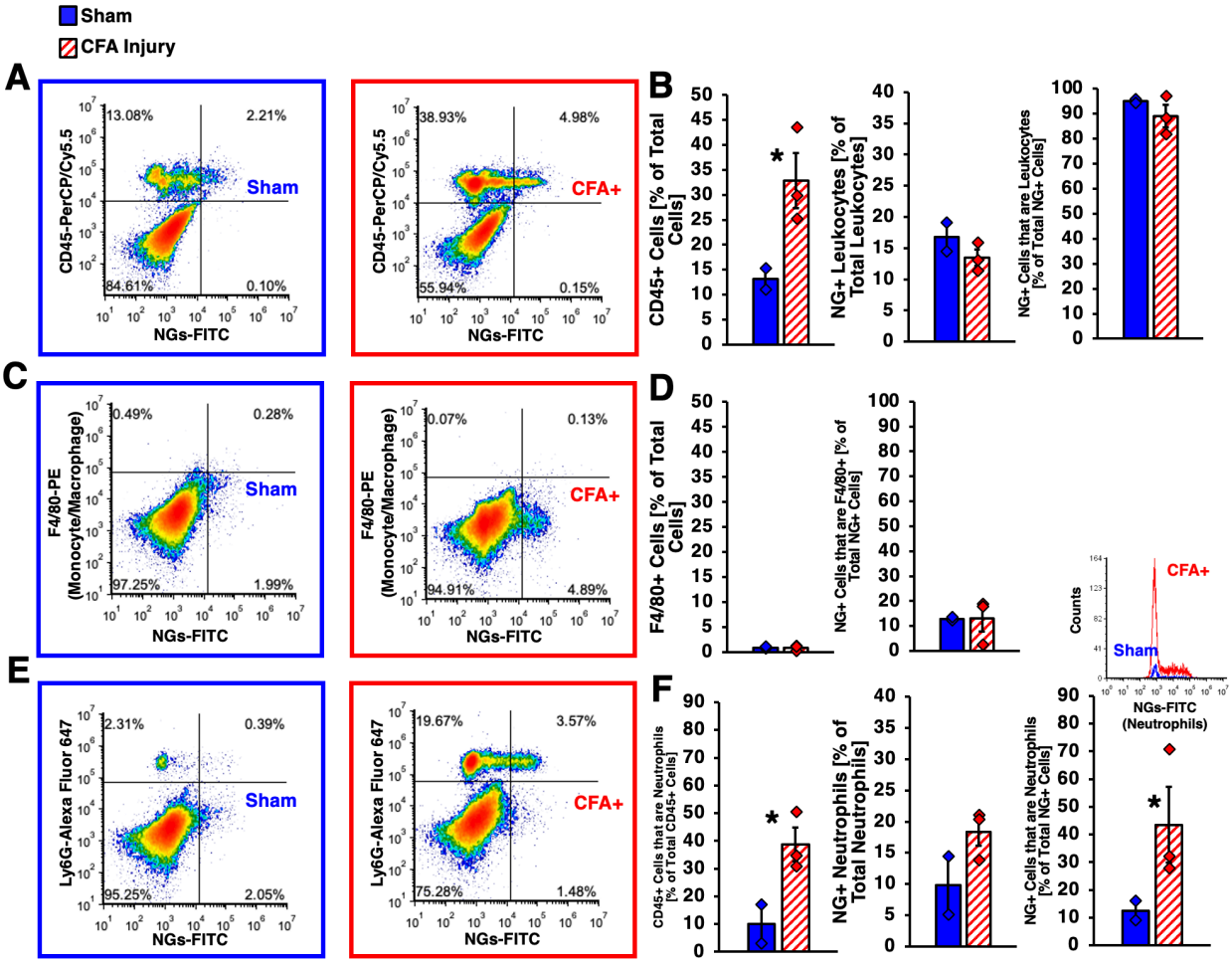

Supplementary Figure 11

Flow Cytometric Characterization of Lysozyme-Dextran Nanogel Uptake in Different Cell Types in Inflamed and Naïve Footpads. Feet injected with complete Freund's adjuvant (CFA, n=3 animals) or saline sham (n=3 animals) were disaggregated after intravenous administration of fluorescent NGs and resultant single cell suspensions were analyzed with flow cytometry. (a) Plots of CD45/leukocyte-associated fluorescence against NG fluorescence in sham-injured and CFA-injured feet. (b) Analysis according to the quadrant gates depicted in (a) determined a ~3-fold increase in the number of leukocytes in CFA-injured feet (**: p=0.038*) and showed that ~90% of NG uptake in both CFA-injured and sham-injured feet was attributable to leukocytes. (c) Plots of F480/macrophage/monocyte-associated fluorescence against NG fluorescence in sham-injured and CFA-injured feet. (d) Analysis of monocyte/macrophage-NG association according to the gates depicted in (c). Macrophages form a negligible fraction of the leukocyte infiltrates in injured paws and have minimal role in uptake of NGs in the inflamed feet. (e) Plots of Ly6G/neutrophil-associated fluorescence against NG fluorescence in sham-injured and CFA-injured feet. (f) Analysis of neutrophil-NG association according to the gates depicted in (e). The number of neutrophils (**: p=0.0009*) and the quantity of NG signal associated with neutrophils (**: p=0.0003*) significantly increased in CFA-injured feet, relative to sham injury. Inset: histogram of

NG fluorescence in neutrophils in sham- and CFA-injured feet. Statements of statistical significance are based on two-way ANOVA with Sidak's multiple comparisons test. All error bars indicate mean ± SEM.

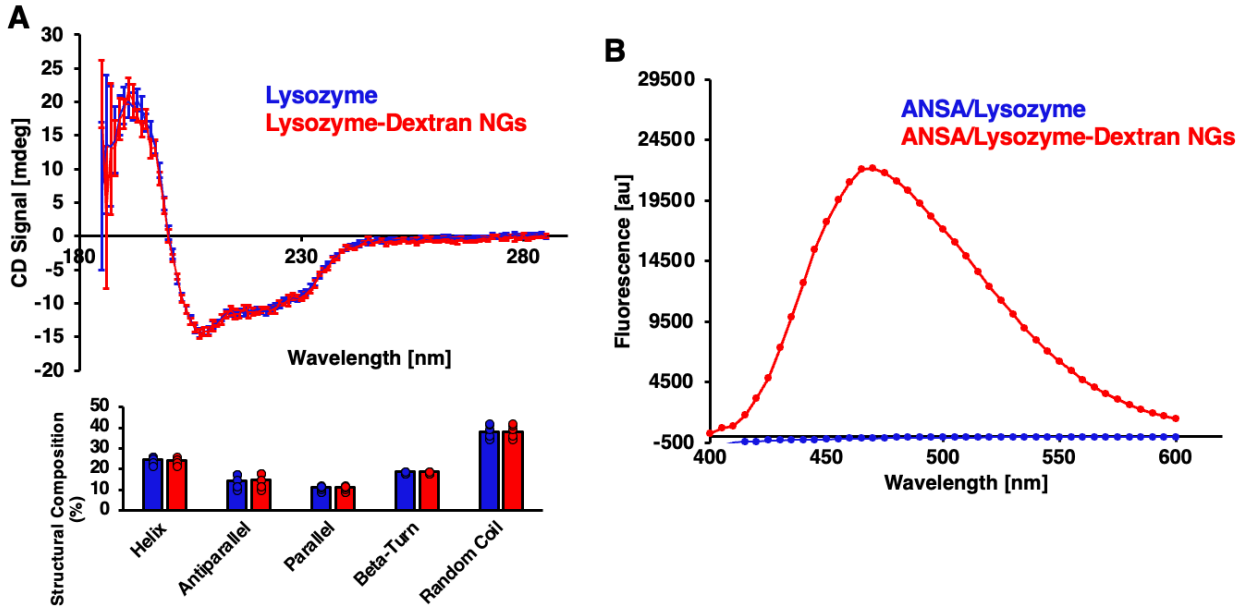

Supplementary Figure 12

Circular Dichroism Spectroscopic Characterization of Lysozyme Secondary Structure and ANSA Characterization of Hydrophobic Domain Accessibility for Lysozyme-Dextran Nanogels. (a) Circular dichroism spectra for NGs (n=5 nanoparticle samples) and free lysozyme (n=5 protein solutions), with free lysozyme concentration set to match the concentration of lysozyme in the NGs. Inset: neural network deconvolution of CD spectra indicating no differences in secondary structure composition between isolated lysozyme and lysozyme in nanogels. (b) 8-anilino-1-naphthalenesulfonic acid (ANSA) staining of free lysozyme or NGs. Increased ANSA fluorescence indicates increased accessibility of hydrophobic domains in the NGs, compared to lysozyme. All error bars indicate mean ± SEM.

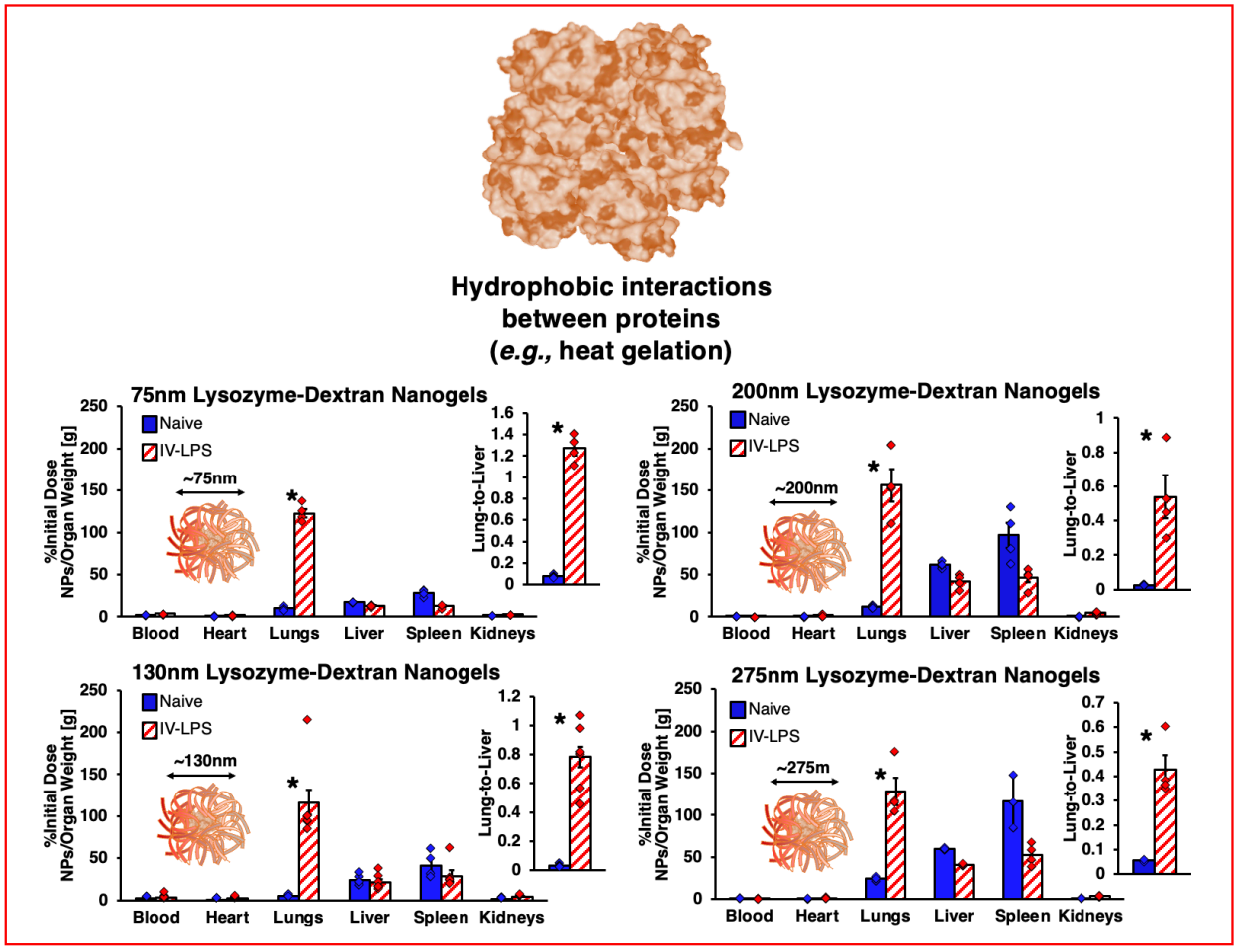

Supplementary Figure 13

Biodistributions of Structural Variants of Lysozyme-Dextran Nanogels in Naïve and IV-LPS-Injured Mice. Lysozyme-dextran nanogel formulations of 75 nm (n=4 IV-LPS animals, n=4 naïve animals, **: $p<1x10^{-10}$ for lungs and p=0.0004 for lungs:liver*), 130 nm (n=8 IV-LPS animals, n=4 naïve animals, **: $p<1x10^{-10}$ for lungs and p=0.00008 for lungs:liver*), 200 nm (n=4 IV-LPS animals, n=4 naïve animals, **: $p<1x10^{-10}$ for lungs and p=0.03 for lungs:liver*), and 275 nm (n=4 IV-LPS animals, n=3 naïve animals, **: $p<1x10^{-10}$ for lungs and p=0.008 for lungs:liver*) diameters as described in supplementary figure 4a, were traced in naïve and intravenous LPS-challenged mice. LPS treatment enhanced pulmonary nanogel uptake for all nanogel variants. Lung, liver, and blood data for 75 nm, 130 nm, and 200 nm nanogels are reproduced in figure 2a in the main text. Statements of statistical significance are based on two-way ANOVA with Sidak's multiple comparisons test. All error bars indicate mean ± SEM.

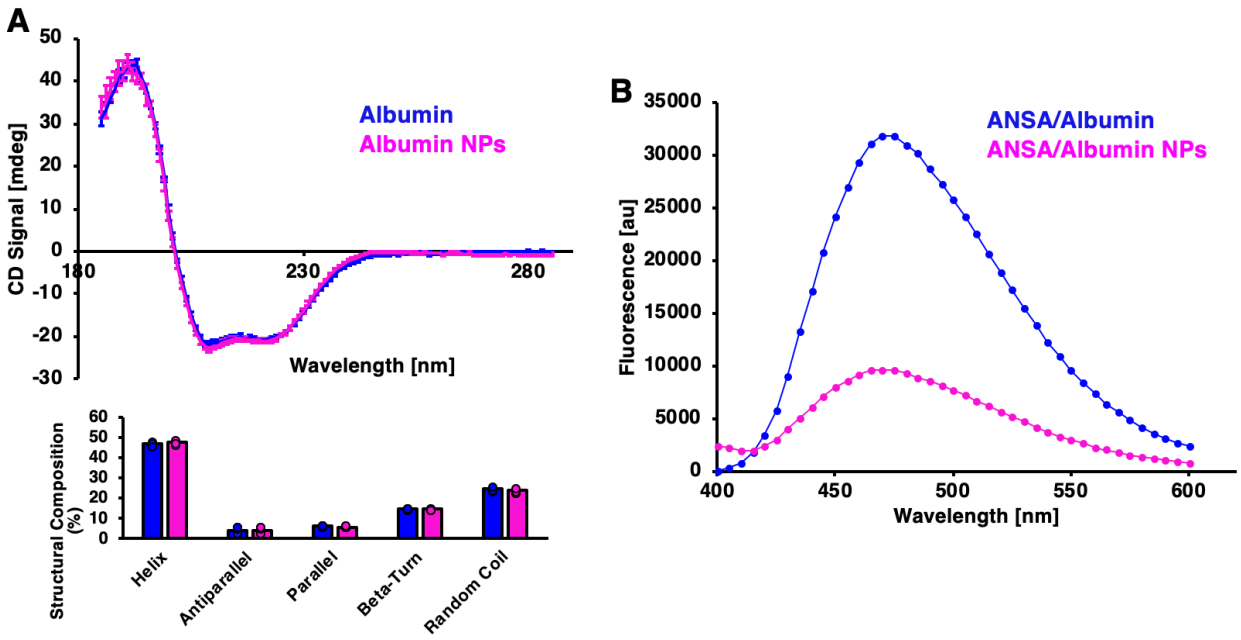

Supplementary Figure 14

Circular Dichroism Spectroscopic Characterization of Albumin Secondary Structure and ANSA Characterization of Hydrophobic Domain Accessibility for Crosslinked Albumin Nanoparticles. (a) Circular dichroism spectra for crosslinked human albumin nanoparticles (n=5 nanoparticle samples) and free human albumin (n=5 protein solutions), with free albumin concentration set to match the concentration of albumin in the nanoparticles. Inset: neural network deconvolution of CD spectra indicating no differences in secondary structure composition between isolated albumin and albumin in nanoparticles. (b) ANSA staining of free human albumin and albumin nanoparticles. Reduced ANSA fluorescence indicates lesser accessibility of hydrophobic domains in the nanoparticles, compared to albumin. All error bars indicate mean ± SEM.

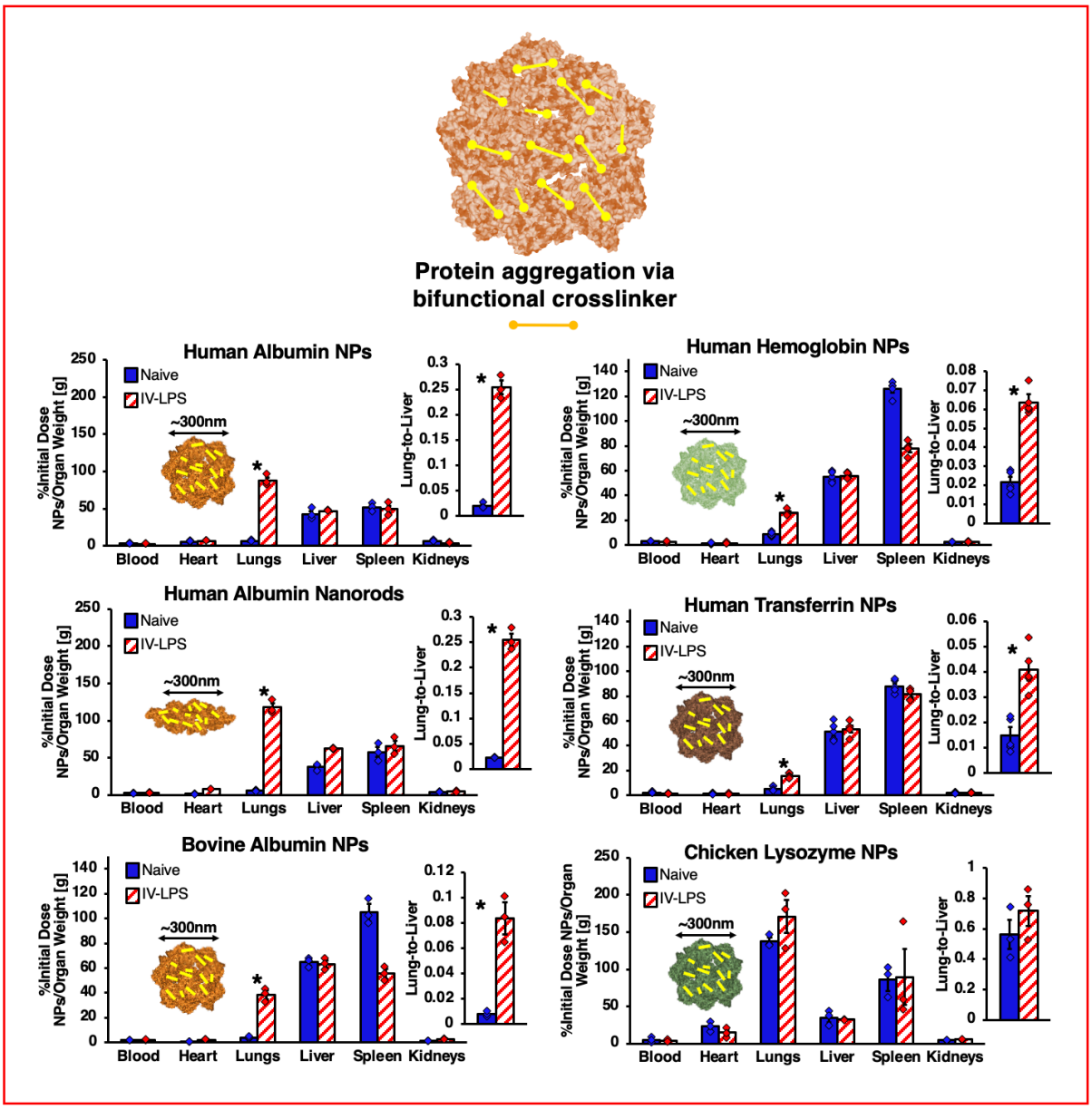

Supplementary Figure 15

Biodistributions of Structural and Compositional Variants of Crosslinked Protein Nanoparticles in Naïve and IV-LPS-Injured Mice. Different crosslinked protein nanoparticle formulations, as described in supplementary figure 4b, were traced in naïve and intravenous LPS-challenged mice. LPS treatment enhanced pulmonary nanoparticle uptake for all crosslinked human albumin nanoparticles (n=3 IV-LPS animals, n=3 naïve animals, **: $p<1x10^{-10}$ for lungs and p=0.004 for lungs:liver*), human albumin nanorods (n=3 IV-LPS animals, n=3 naïve animals, **: $p<1x10^{-10}$ for lungs and p=0.003 for lungs:liver*), bovine albumin nanoparticles (n=3 IV-LPS animals, n=3 naïve animals, **: $p<1x10^{-10}$ for lungs and p=0.02 for lungs:liver*), human hemoglobin nanoparticles (n=4 IV-LPS animals, n=5 naïve animals, **: $p<1x10^{-10}$ for lungs and p=0.0005 for lungs:liver*), and human transferrin nanoparticles (n=5 IV-LPS animals, n=5 naïve animals, **: p=0.00002 for lungs and p=0.005 for lungs:liver*). For lysozyme

particles (n=3 IV-LPS animals, n=3 naïve animals), uptake in both injured and naïve lungs exceeded 20% of initial dose. Lung, liver, and blood data for human albumin nanoparticles, human albumin nanorods, and bovine albumin nanoparticles are reproduced in figure 2b in the main text. Statements of statistical significance are based on two-way ANOVA with Sidak's multiple comparisons test. All error bars indicate mean ± SEM.

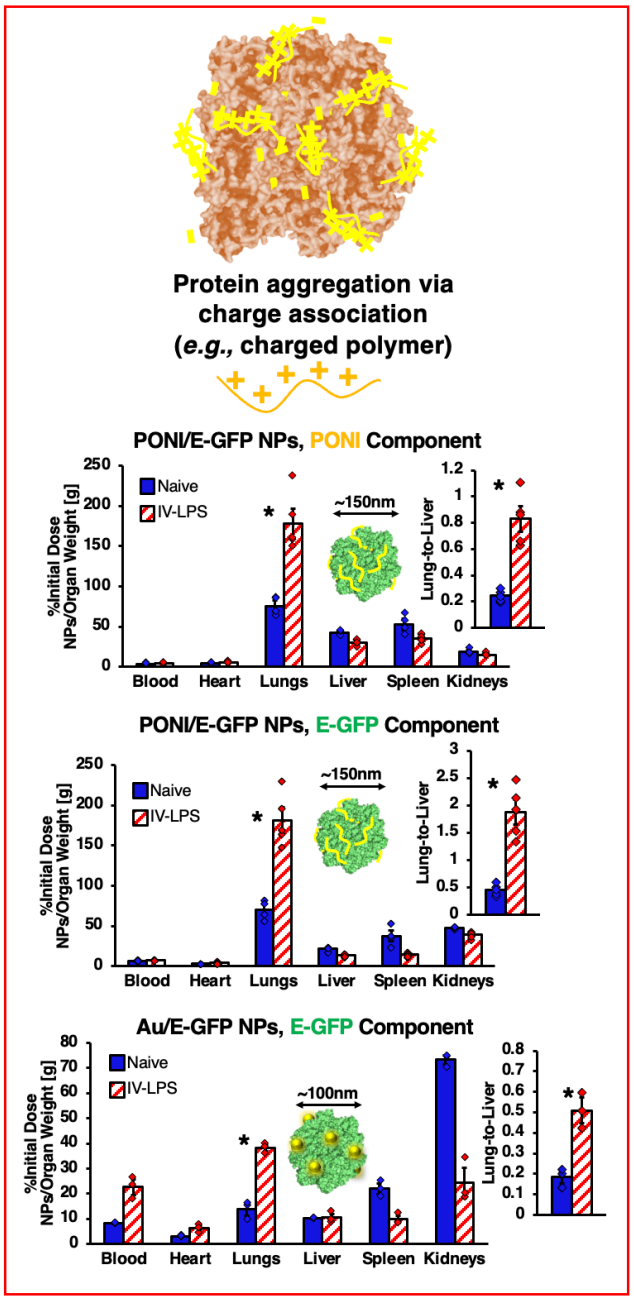

Supplementary Figure 16
Biodistributions of Compositional Variants of Charge-Agglutinated Green Fluorescent Protein Nanoparticles in Naïve and IV-LPS-Injured Mice. Nanoparticles formed by combining glutamate-tagged green fluorescent protein with arginine-tagged gold

nanoclusters (Au) or arginine-poly(oxanorborneneimide) (PONI) (see supplementary figure 4c) were traced in naïve and intravenous LPS-challenged mice. PONI-eGFP nanoparticles were traced by labeling eGFP with ^{125}I and PONI with ^{131}I. LPS treatment enhanced pulmonary nanoparticle uptake both PONI/E-GFP (n=5 IV-LPS animals and n=4 naïve animals) and Au/E-GFP (n=3 IV-LPS animals and n=3 naïve animals) nanoparticles. Simultaneous PONI and eGFP tracing indicated that both nanoparticle components localized to the lungs after LPS injury. For PONI tracing of PONI/E-GFP nanoparticles, **: $p<1x10^{-10}$ for lungs and p=0.003 for lungs:liver*. For E-GFP tracing of PONI/E-GFP nanoparticles, **: $p<1x10^{-10}$ for lungs and p=0.003 for lungs:liver*. For E-GFP tracing of Au/E-GFP nanoparticles, **: $p=1.6x10^{-9}$ for lungs and p=0.047 for lungs:liver*. Lung, liver, and blood data are reproduced in figure 2c in the main text. Statements of statistical significance are based on two-way ANOVA with Sidak's multiple comparisons test. All error bars indicate mean ± SEM.

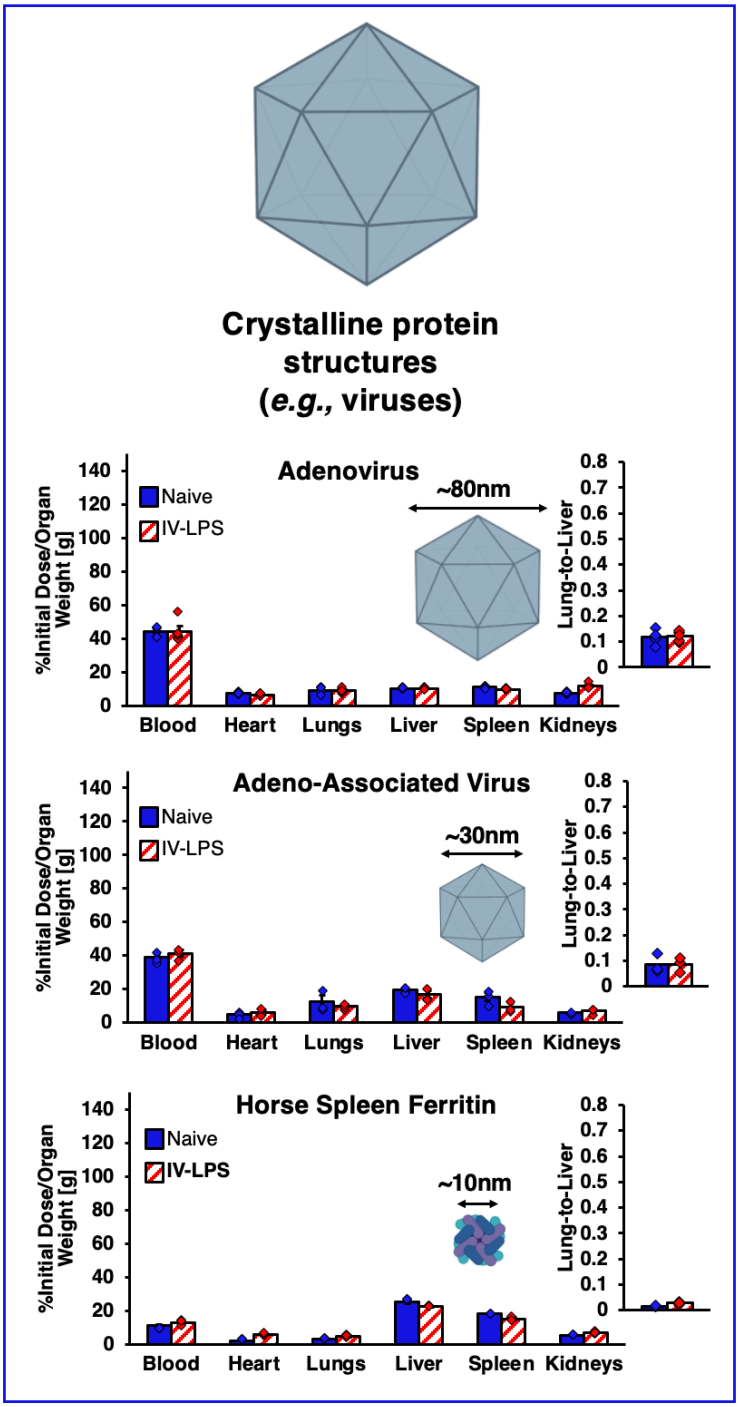

Supplementary Figure 17

Biodistributions of Adenovirus, Adeno-Associated Virus, and Horse Spleen Ferritin Nanocages in Naïve and IV-LPS-Injured Mice. Three naturally occurring crystalline protein nanostructures (see supplementary figure 4c for DLS data) were traced in naïve and intravenous LPS-challenged mice (nanoparticle schematics created with BioRender.com). LPS treatment had no effect on the biodistributions of radiolabeled adenovirus (n=5 IV-LPS animals, n=5 naïve animals), adeno-associated virus (n=3 IV-LPS animals, n=3 naïve animals), and horse spleen ferritin (n=5 IV-LPS animal, n=5

naïve animals. Lung, liver, and blood data are reproduced in figure 3d in the main text. All error bars indicate mean ± SEM.

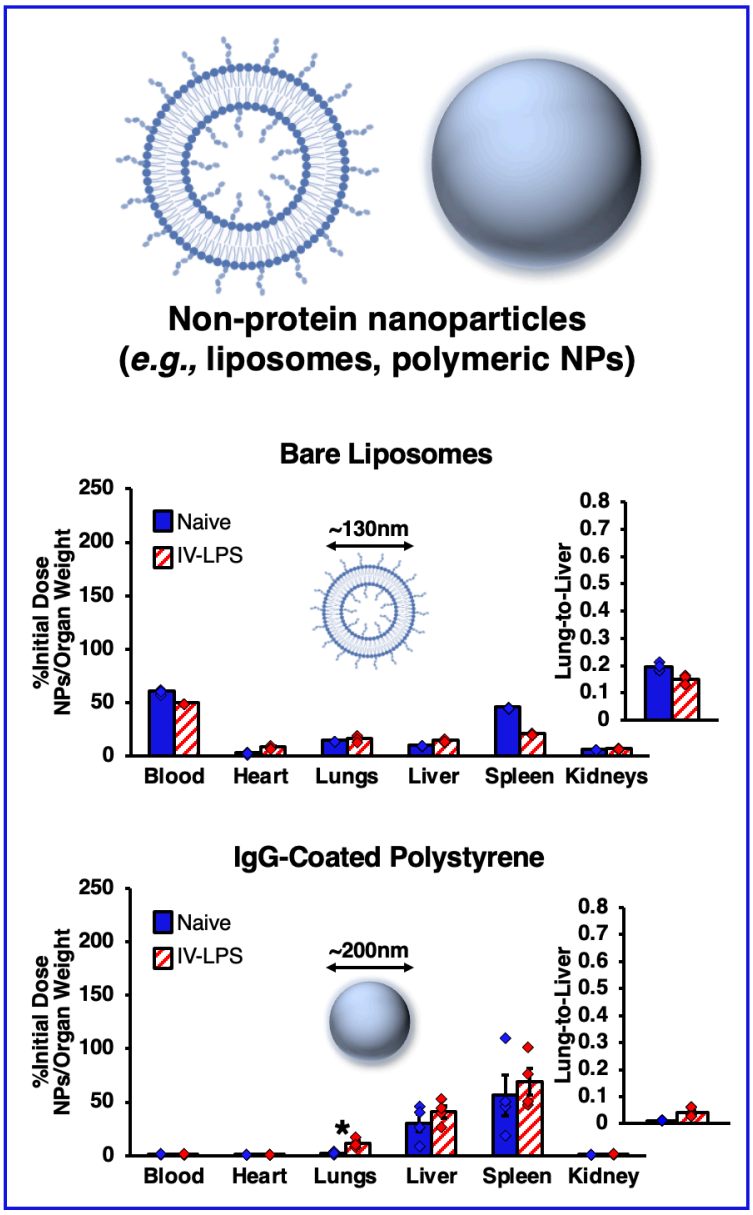

Supplementary Figure 18

Biodistributions of Bare Liposomes and IgG-Coated Polystyrene Nanoparticles in Naïve and IV-LPS-Injured Mice. As example nanoparticles not based on assembly of protein, bare liposomes (schematic created with BioRender.com, see supplementary figure 4d for DLS data) and IgG-coated polystyrene nanoparticles (see supplementary figure 4c for DLS data) were traced in naïve and intravenous LPS-challenged mice. LPS treatment had no effect on the biodistribution of bare liposomes (n=4 IV-LPS animals, n=4 naïve animals). LPS treatment did enhance pulmonary uptake of IgG-coated polymeric nanoparticles (n=4 IV-LPS animals, n=4 naïve animals, *: p=0.0004), albeit with lower levels of lung uptake than observed with variant nanogels, crosslinked

protein particles, or charge associated protein particles. Lung, liver, and blood data are reproduced in figure 2e in the main text. Statements of statistical significance are based on two-way ANOVA with Sidak's multiple comparisons test. All error bars indicate mean ± SEM.

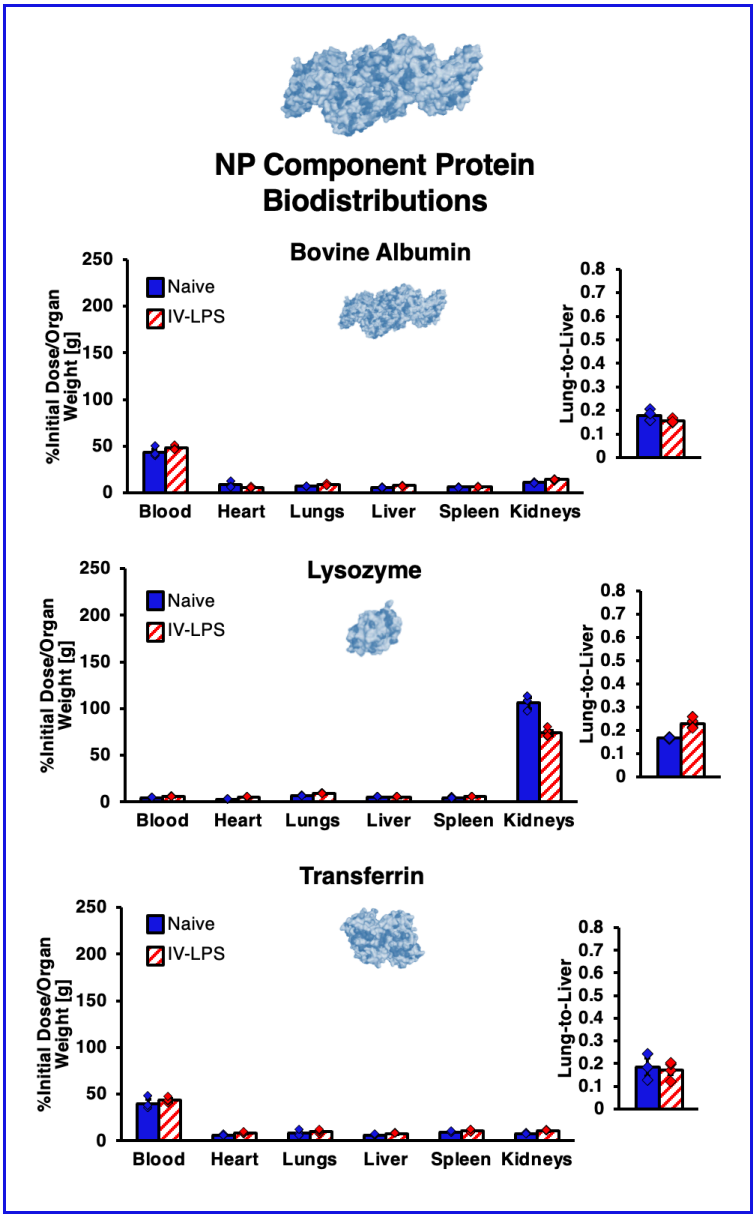

Supplementary Figure 19

Biodistributions of Isolated Albumin, Lysozyme, and Transferrin in Naïve and IV-LPS-Injured Mice. Different radiolabeled isolated proteins were traced in naïve and intravenous LPS-challenged mice. LPS treatment had no effect on the biodistributions of bovine albumin (n=4 IV-LPS animals, n=4 naïve animals), hen lysozyme (n=4 IV-LPS animals, n=3 naïve animals), or human transferrin (n=4 IV-LPS animals, n=3 naïve animals). All error bars indicate mean ± SEM.

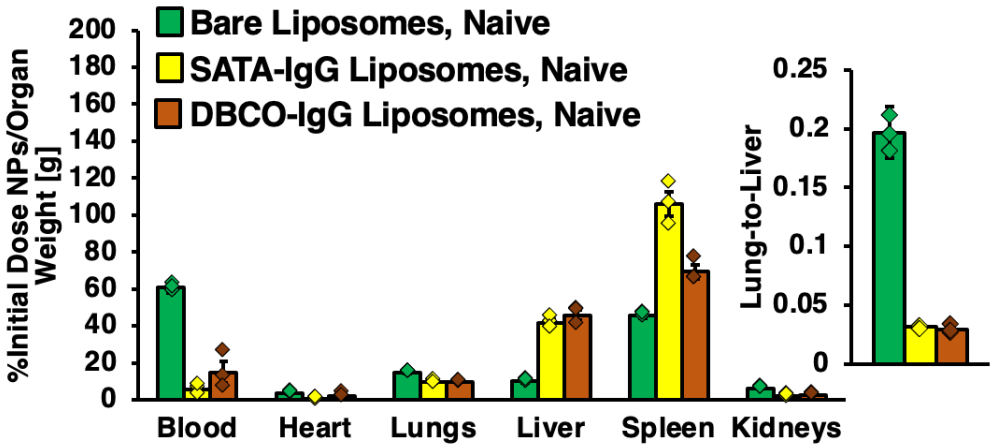

Supplementary Figure 20

Biodistributions in Naïve Mice for Bare Liposomes, Liposomes Conjugated to IgG via SATA-Maleimide Reaction, and Liposomes Conjugated to IgG via DBCO-Azide Reaction. In juxtaposition to biodistribution data in IV LPS-challenged mice, as presented in figure 3b in the main text, bare liposomes (n=3 animals), IgG-SATA liposomes (n=3 animals), and IgG-dibenzocyclooctyne (DBCO) liposomes (n=3 animals) were traced in naïve mice. Whereas IgG-DBCO liposomes had uniquely high levels of pulmonary uptake in LPS-challenged mice, no significant differences were noted in pulmonary uptake of the different liposome formulations in naïve mice. All error bars indicate mean ± SEM.

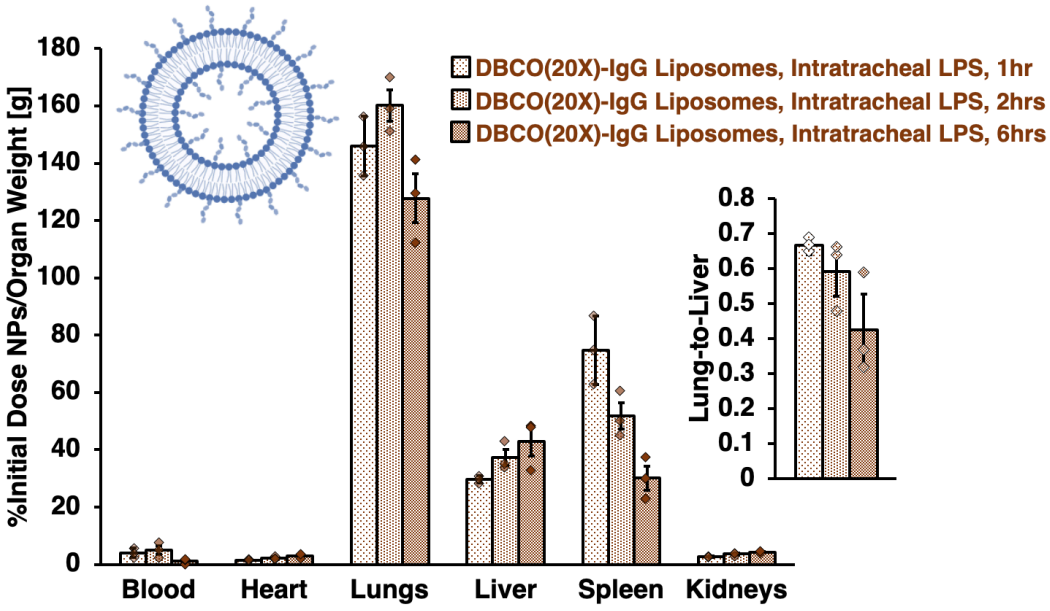

Supplementary Figure 21

Biodistributions of DBCO:IgG (20:1) Liposomes in Mice 1, 2, and 6 Hours After Intratracheal LPS Injury. As an alternative to intravenous LPS injection, mice were administered LPS via intratracheal (IT) instillation, prior to bolus dosing with liposomes coated with IgG conjugated to a 20-fold excess of DBCO (liposome schematic created with BioRender.com). As with IV LPS-injured mice, IT LPS injury led to high levels of

pulmonary uptake for DBCO(20X)-IgG liposomes. Similar levels of pulmonary uptake were observed at 1 (n=3 animals), 2 (n=3 animals), and 6 hours (n=3 animals) after IT LPS instillation, with liposomes circulating for 30 minutes for each data set. All error bars indicate mean ± SEM.

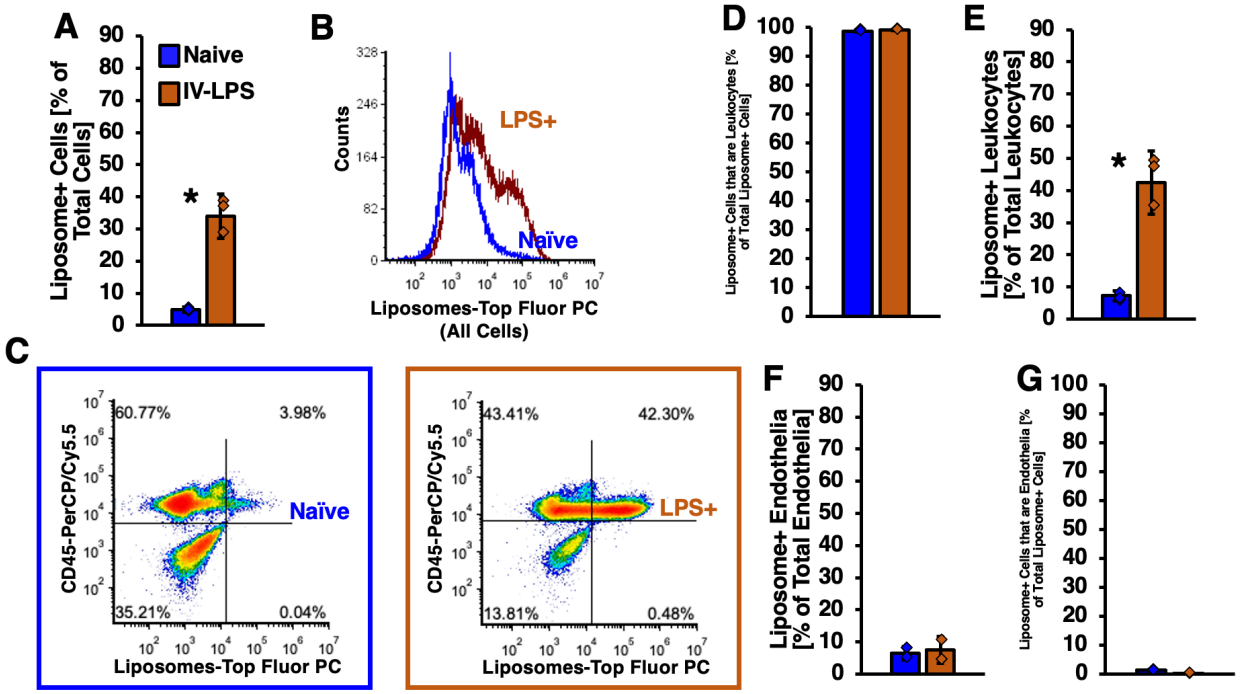

Supplementary Figure 22

Flow Cytometric Characterization of DBCO:IgG (20:1) Liposome Uptake in Leukocytes and Endothelial Cells in Naïve and Inflamed Lungs. (a) Fluorescence from DBCO-IgG liposomes containing green fluorescent TopFluor lipid was measured in single cell suspensions prepared from mouse lungs harvested after 30 minutes liposome circulation. With gates set as depicted in main text figure 3c, the number of cells positive for liposome fluorescence increased between naïve (n=3 animals) and LPS-challenged (n=3 animals) lungs (**: $p=8.9x10^{-10}$*). (b) A population of high-fluorescence cells was detected in IV LPS-challenged lungs, but not naïve lungs. (c) Fluorescence generated by CD45 staining, distinguishing leukocytes in single cell suspensions, plotted against DBCO-IgG liposome fluorescence in single cell suspensions prepared from naïve and IV LPS-challenged lungs. (d-e) With gates set by the quadrants delineated in (c), correlation between liposome fluorescence and CD45 staining indicated the percentage of liposome-bearing cells that were leukocytes as >95% in both naïve and IV LPS-challenged lungs. Similar analysis indicated that the fraction of leukocytes containing liposomes increased in LPS-challenged vs. naïve lungs (**: $p<1x10^{-10}$*). (f-g) Single cell suspensions were stained with CD31 antibody to indicate endothelial cells. Correlation between CD31 staining and liposome fluorescence indicated that <10% of endothelial cells contained liposomes and <1% of all liposome-positive cells in the suspensions were endothelial cells. Statements of statistical significance are based on two-way ANOVA with Sidak's multiple comparisons test. All error bars indicate mean ± SEM.

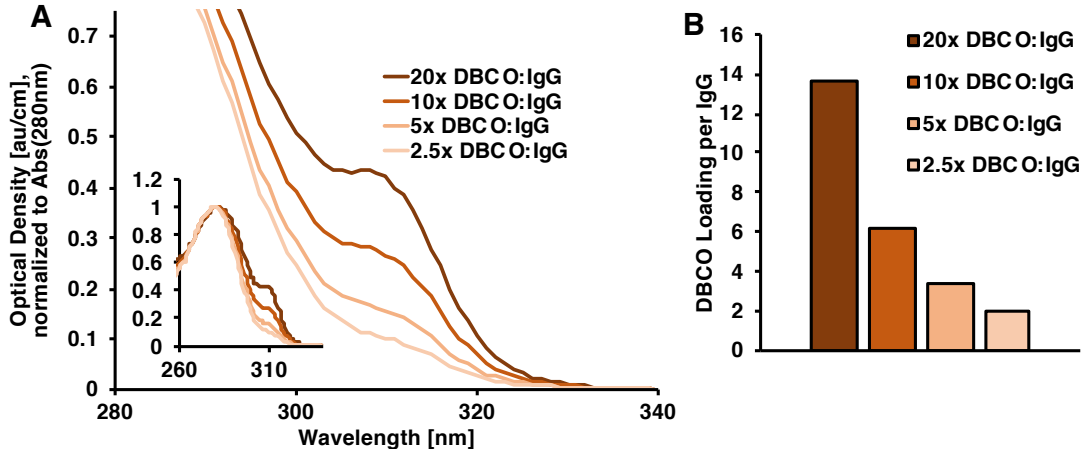

Supplementary Figure 23

Spectrophotometric Characterization of DBCO Conjugation to IgG. (a) IgG was reacted with 2.5-fold, 5-fold, 10-fold, and 20-fold excesses of DBCO-PEG$_4$-NHS ester and optical density of the resulting conjugates was determined between 220nm and 350nm. Absorbance at 309nm indicated DBCO on the IgG and absorbance at 280nm was indicative of IgG concentration (see inset for absorbance data at 280nm). (b) Spectral overlap of DBCO absorbance with IgG absorbance was noted by correcting absorbance at 280nm according to $Abs_{280C} = Abs_{280} - 1.089 \times Abs_{309}$. Molar IgG concentration was determined according to $[IgG] = \frac{Abs_{280C}}{\varepsilon_{280,IgG}}$, where $\varepsilon_{280,IgG}$ is the IgG extinction coefficient at 280nm, 204000 L mol^{-1}cm^{-1}. Molar DBCO concentration was determined according to $[DBCO] = \frac{Abs_{309}}{\varepsilon_{309,DBCO}}$, where $\varepsilon_{309,DBCO}$ is the DBCO extinction coefficient at 309nm, 12000 L mol^{-1}cm^{-1}. Number of DBCO per IgG was determined as the ratio $\frac{[DBCO]}{[IgG]}$.

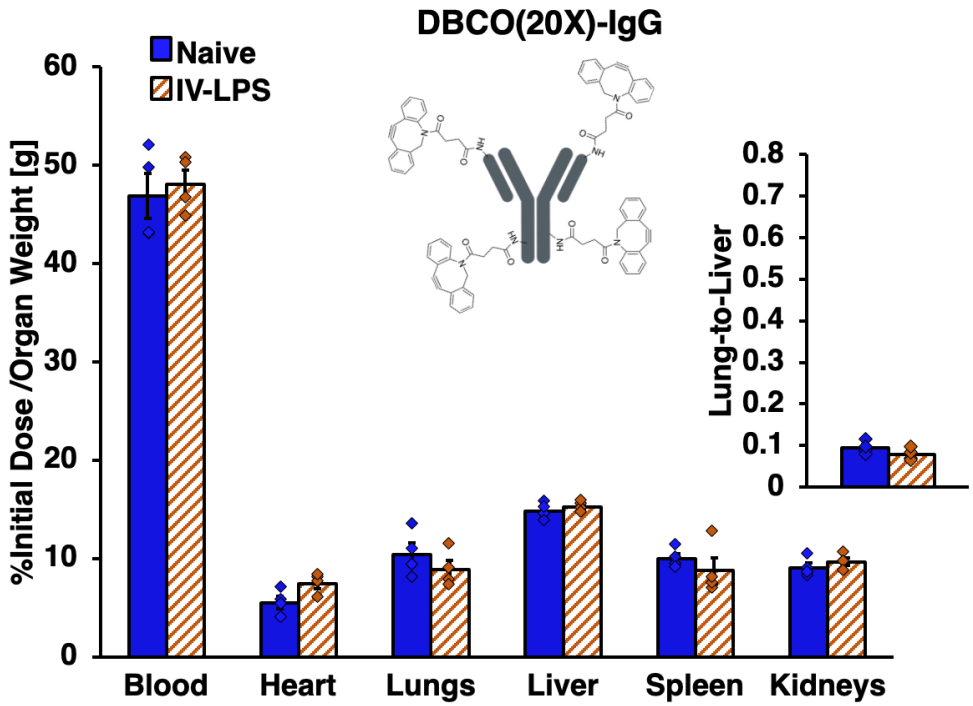

Supplementary Figure 24

Biodistributions of Isolated DBCO:IgG (20:1) in Naïve and IV-LPS-Injured Mice. IgG conjugated to a 20-fold excess of DBCO was traced in naïve (n=4 animals) and IV LPS-challenged (n=4 animals) mice. No significant differences were observed in isolated DBCO(20X)-IgG biodistributions between naïve and injured mice. All error bars indicate mean ± SEM.

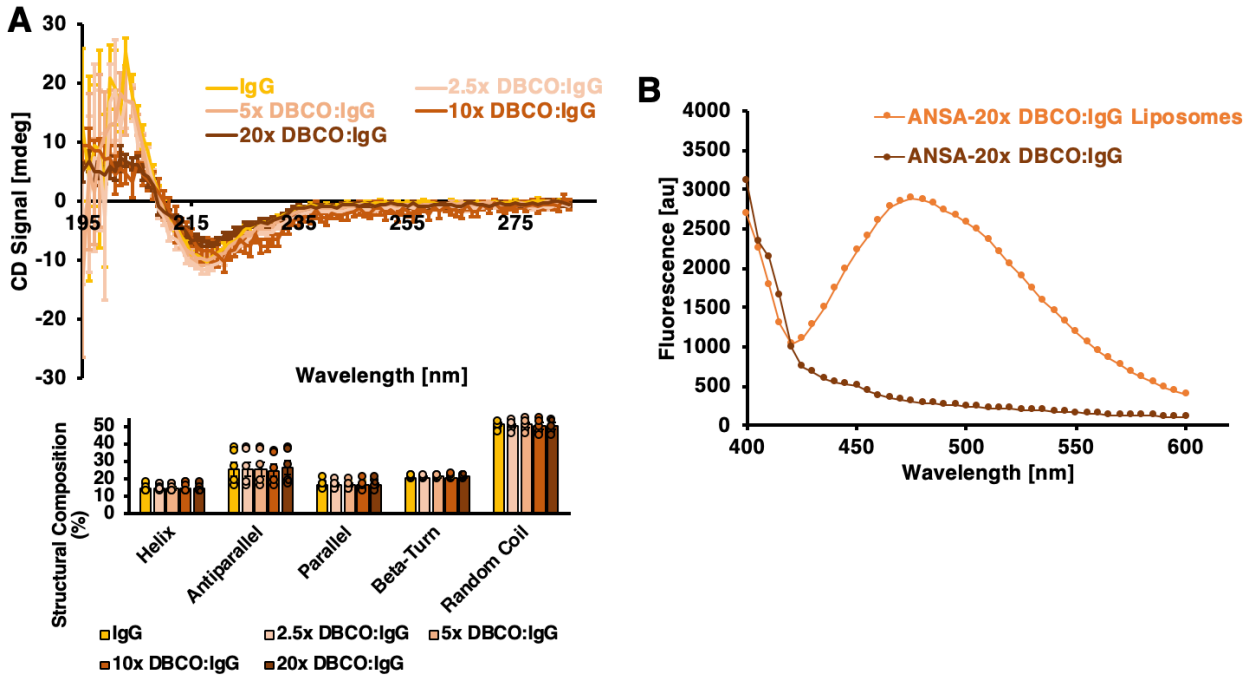

Supplementary Figure 25

Circular Dichroism Spectroscopic Characterization of Protein Secondary Structure in DBCO-Modified IgG and ANSA Characterization of Hydrophobic Domain Accessibility on DBCO:IgG (20:1) Liposomes. (a) Circular dichroism spectra for IgG modified with different concentrations of DBCO-PEG$_4$-NHS ester and unmodified IgG (n=5 protein solutions for each DBCO modification density). Inset: neural network deconvolution of CD spectra indicating that IgG secondary structure composition was unchanged by modification with all tested densities of DBCO. (b) 8-anilino-1-naphthalenesulfonic acid (ANSA) staining of IgG modified with a 20-fold excess of DBCO or liposomes conjugated to DBCO(20X)-IgG, with free DBCO(20X)-IgG concentration matched to the DBCO(20X)-IgG concentration on the liposomes. Increased ANSA fluorescence indicates increased accessibility of hydrophobic domains on the liposomes, compared to free DBCO(20X)-IgG. All error bars indicate mean ± SEM.

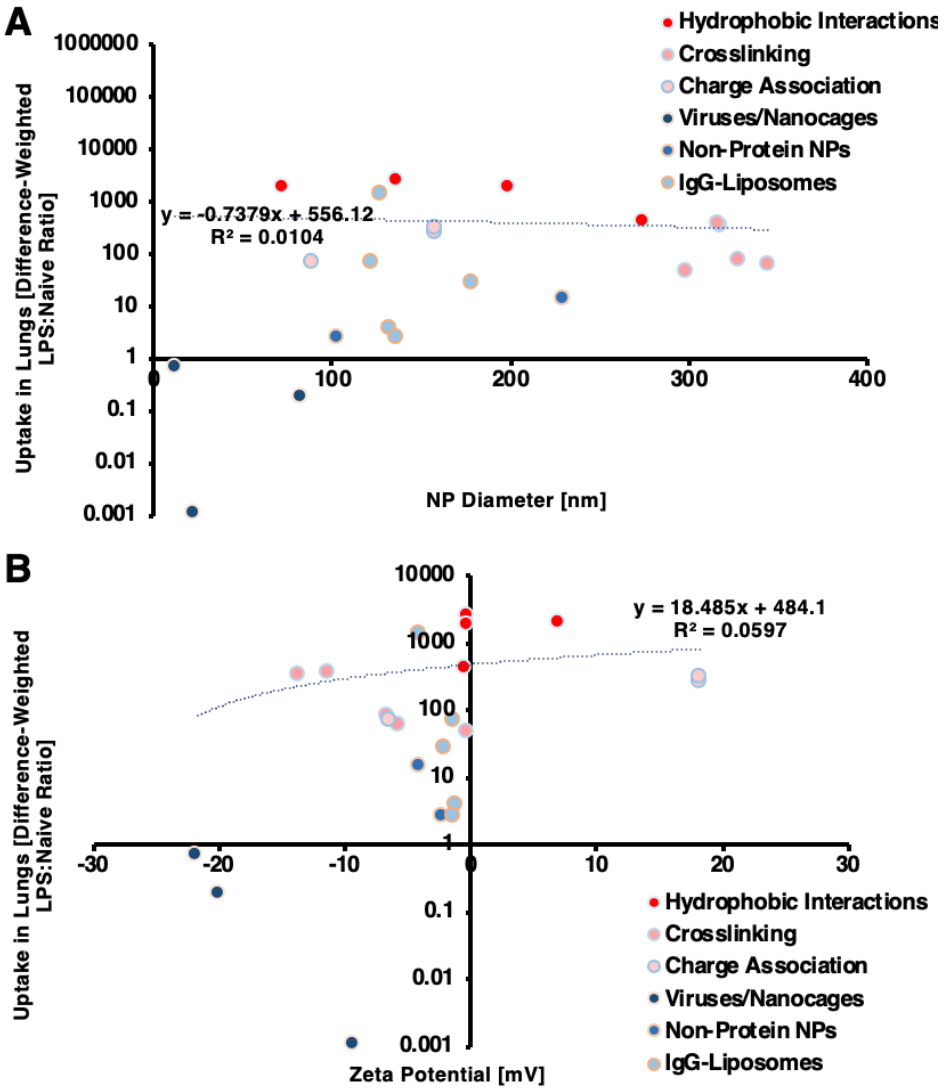

Supplementary Figure 26

Correlation or Nanoparticle Tropism for Inflamed Lungs with Nanoparticle Size and Surface Charge. As a metric for nanoparticle selectivity for inflamed lungs, weighted

LPS:naïve shifts in nanoparticle uptake in the lungs were determined according to $LPS{:}\,naive = (\overline{\%ID_{LPS}} - \overline{\%ID_{Naive}}) \times \frac{\overline{\%ID_{LPS}}}{\overline{\%ID_{Naive}}}$. Nanoparticle selectivity for inflamed lungs is plotted as log-linear data against nanoparticle diameter (a, based on data in Supplementary Figure 4) and zeta potential (b, based on data in Supplementary Table 1). Linear fits of selectivity data provided r-squared values of 0.01 and 0.06 for plots against size and zeta potential, respectively. Therefore, selectivity for inflamed lungs did not linearly correlate with either parameter.

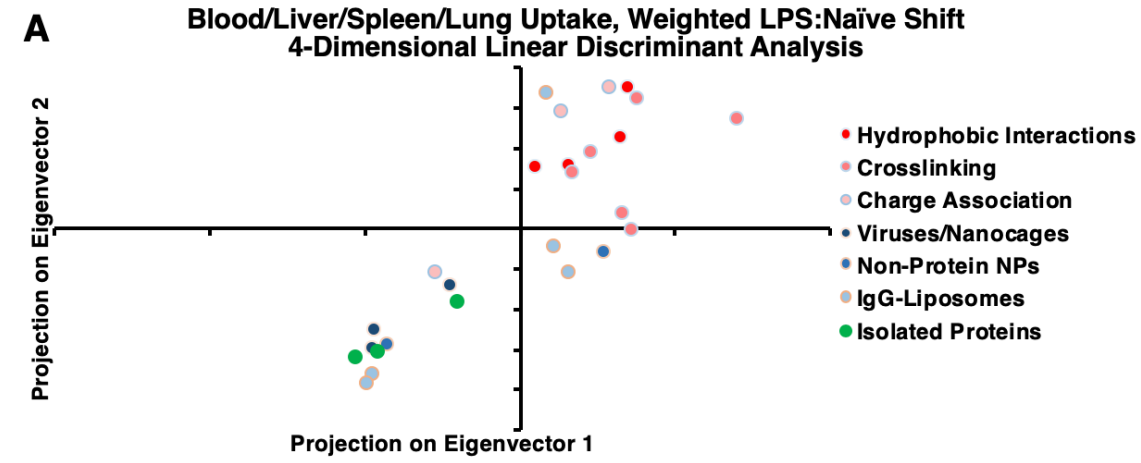

	Eigenvector 1	Eigenvector 2	Eigenvector 3	Eigenvector 2	Eigenvalues
Blood	-0.28233	-0.10194	0.59684	0.218224	3.881353
Liver	-0.32578	0.75672	-0.25106	0.819177	3.190054
Spleen	-0.88632	-0.18302	0.40374	-0.528561	0.225852
Lungs	0.16911	0.61927	0.64633	0.044156	0.051049

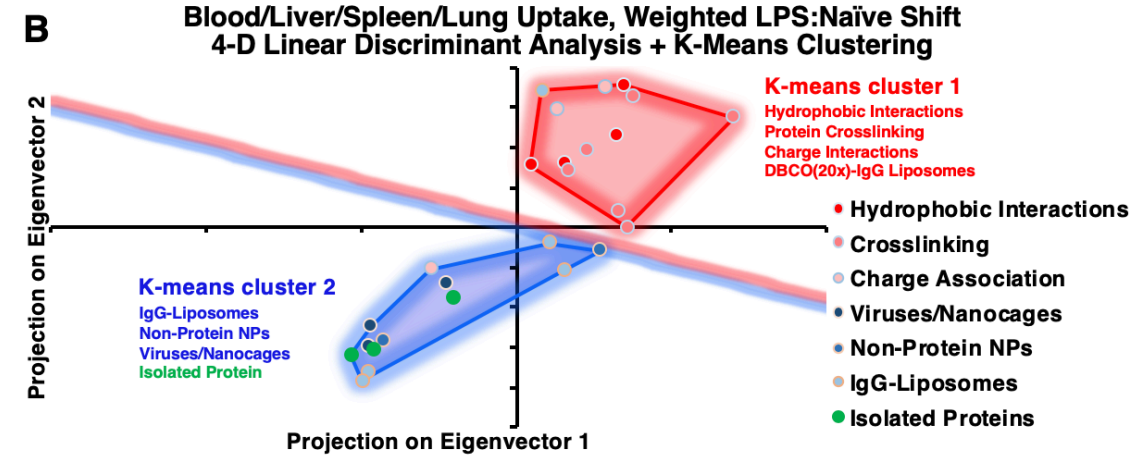

Supplementary Figure 27

Linear Discriminant Analysis of Nanoparticle Biodistributions in Naïve and LPS-Injured Mice. Nanoparticle and protein retention in blood, lungs, liver, and spleen in naïve and IV LPS-challenged mice was compiled for all tested nanoparticles and proteins. For

each organ, weighted LPS:naïve shifts in nanoparticle uptake were determined according to $LPS{:}\,naive = (\overline{\%ID_{LPS}} - \overline{\%ID_{Naive}}) \times \frac{\overline{\%ID_{LPS}}}{\overline{\%ID_{Naive}}}$. LPS:naïve shift data for each organ were then centered and normalized via $LPS{:}\,naive_{norm} = (LPS{:}\,naive - \overline{LPS{:}\,naive})/\overline{LPS{:}\,naive}$. Centered and normalized LPS:naïve shifts were subjected to linear discriminant analysis, with data divided into subclasses defined as: hydrophobic interactions (NGs), crosslinking (crosslinked protein nanoparticles), charge association (PONI/E-GFP and Au/E-GFP nanoparticles), viruses/nanocages (adenovirus, adeno-associated virus, and ferritin), non-protein NPs (polystyrene nanoparticles and bare liposomes), IgG-liposomes (encompassing SATA-maleimide and all variant DBCO conjugation chemistries), and isolated proteins. Projection of shift data along the first two eigenvectors is depicted in (a), with each eigenvector and corresponding eigenvalue enumerated in the inset table. Eigenvectors 1 and 2, accounting for >95% of variability in the data, were dominated by variation in splenic and pulmonary/hepatic uptake, respectively. (b) Projections in (a) were subjected to K-means clustering analysis, indicating two clusters with nanoparticles with agglutinated protein (lysozyme-dextran nanogels, DBCO(20X)-IgG liposomes, crosslinked protein nanoparticles, and glutamate-tagged GFP nanoparticles) forming a single cluster.

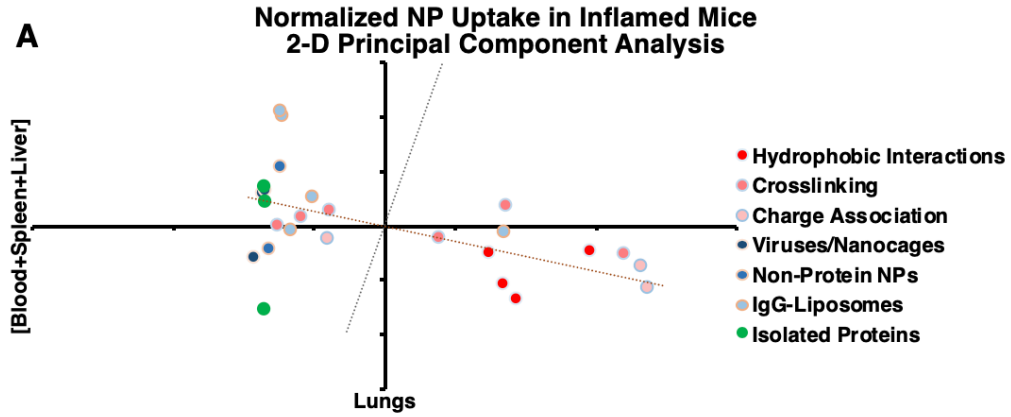

	Eigenvector 1	Eigenvector 2	Eigenvalues
Lungs	-0.96438	-0.26453	1.03398
[Blood+Liver+Spleen]	0.26453	-0.96438	0.14179

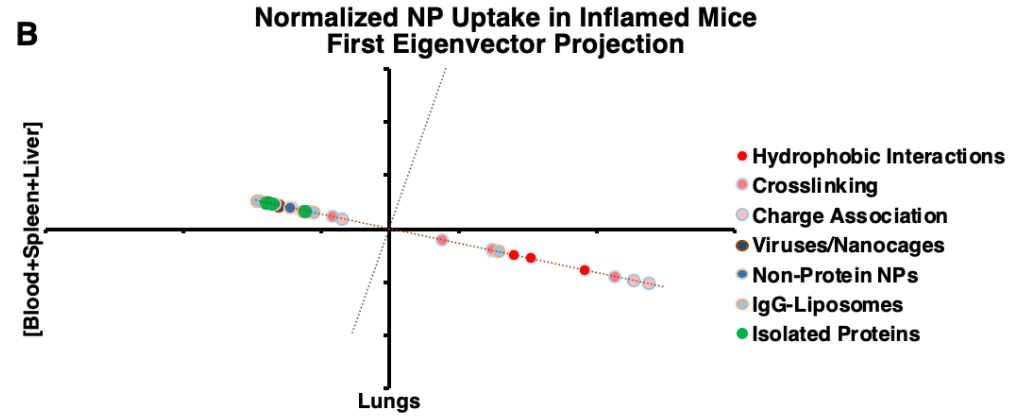

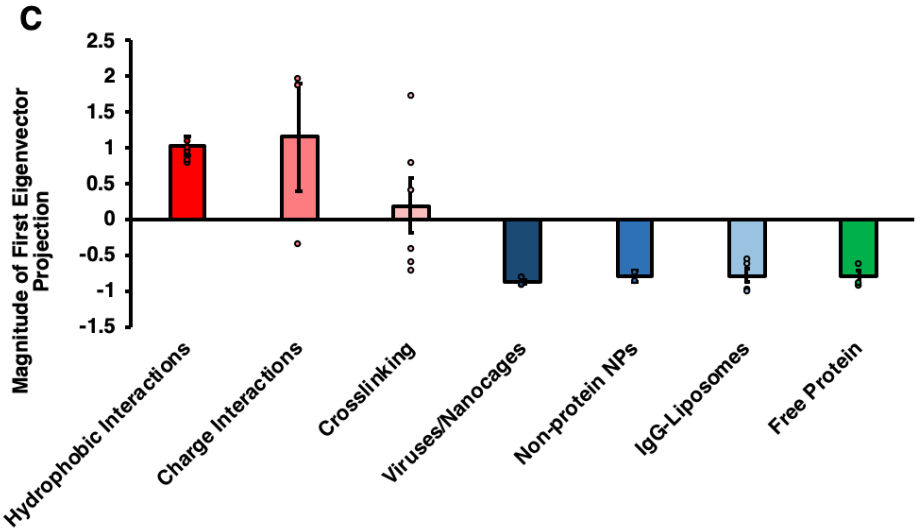

Supplementary Figure 28

Principal Component Analysis of Nanoparticle Biodistribution Data in LPS-Injured Mice. (a) Nanoparticle and protein retention in lungs vs. all other organs in IV-LPS-challenged

mice was compiled for all tested nanoparticles and proteins. Data was centered and normalized according to $\%ID_{norm} = (\%ID - \overline{\%ID})/\overline{\%ID}$. Principal component analysis assessed eigenvectors depicted as dashed axes in (a) and enumerated in the inset table. (b) Centered and normalized data was projected along the first eigenvector. (c) Magnitude of the data projection along the first eigenvector was assessed and first eigenvector projection values were compiled in the nanoparticle classes described in supplementary figure 27, with DBCO(20X)-IgG liposomes excluded. Classes grouped into K-means cluster 1 (red/pink, see supplementary figure 27b) had significantly different first eigenvector projections, compared to classes grouped into K-means cluster 2 (blue/green). Statements of statistical significance are based on one-way ANOVA with Tukey's multiple comparisons test and p-values are tabulated below. All error bars indicate mean ± SEM.

	Hydrophobic	Charge	Crosslinking
Viruses	0.0029	0.0047	0.0417
Non-protein NPs	0.0046	0.007	0.0643
IgG-Liposomes	0.002	0.0038	0.0361
Free Protein	0.0042	0.0064	0.0585

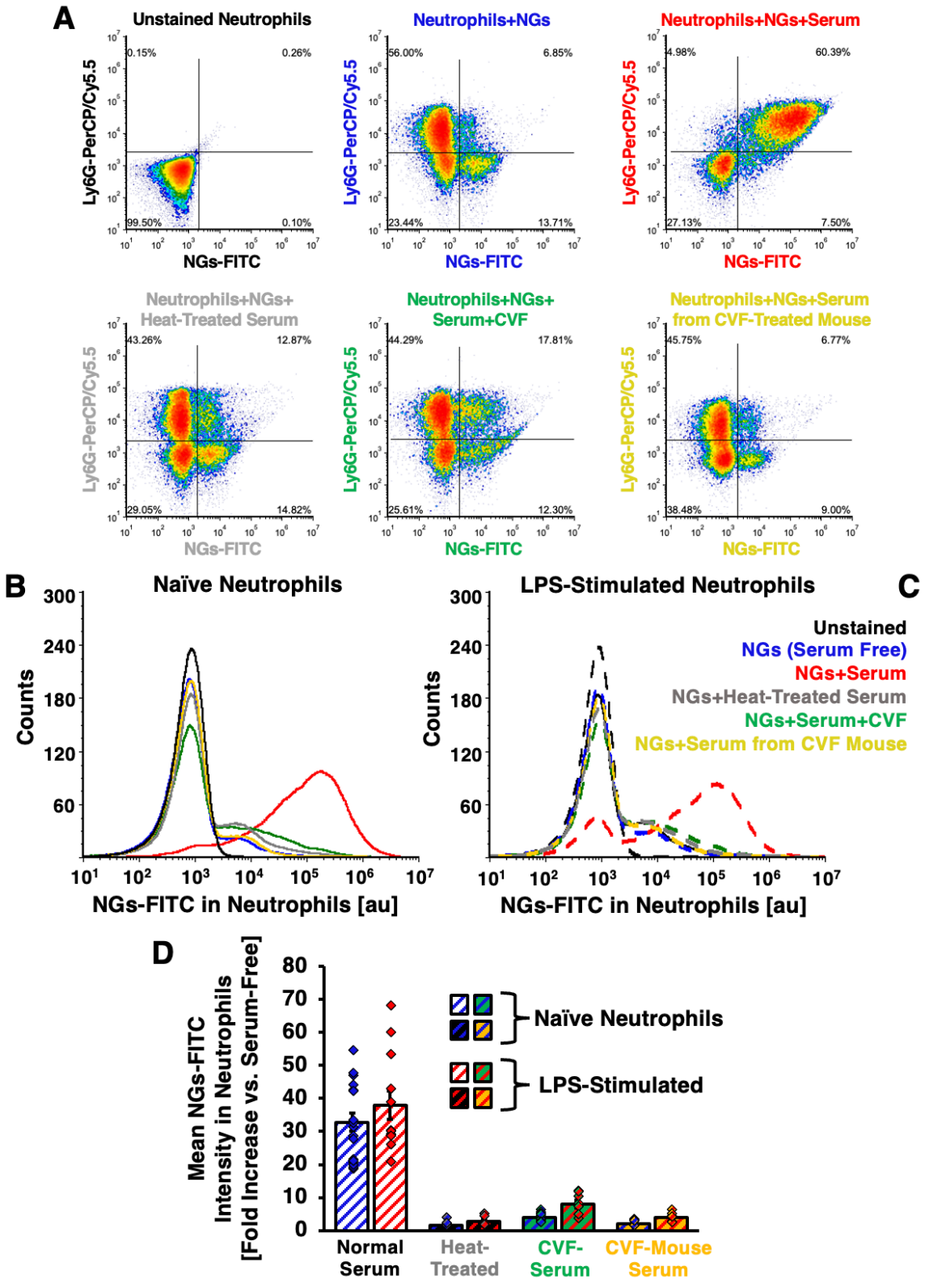

Supplementary Figure 29

Flow Cytometric Characterization of Lysozyme-Dextran Nanogels Uptake in Neutrophils In Vitro Under Different Serum Conditions. (a) Gating strategies indicating determination

of lysozyme-dextran nanogel fluorescence vs. levels of anti-Ly6G neutrophil staining after treatment of lysozyme-dextran nanogels with different serum conditions. (b-c) Example histograms of lysozyme-dextran nanogel fluorescence in naïve (b) and LPS-stimulated (c) neutrophils with lysozyme-dextran nanogels treated with different serum conditions. (d) Quantification of mean lysozyme-dextran nanogel fluorescence intensity in naïve and LPS-stimulated neutrophils after treatment of lysozyme-dextran nanogels with; normal serum (n=18 naïve neutrophil preparations, n=12 LPS-stimulated neutrophil preparations); heat-treated serum (n=10 naïve neutrophil preparations, n=5 LPS-stimulated neutrophil preparations); CVF-treated serum (n=11 naïve neutrophil preparations, n=7 LPS-stimulated neutrophil preparations); serum from a mouse treated with CVF (n=8 naïve neutrophil preparations, n=7 LPS-stimulated neutrophil preparations). Data show complement-dependent serum opsonization, but not LPS stimulation of neutrophils, correlates to nanogel uptake in neutrophils *in vitro*, as in figures 4c and 4d, but with data from nanogels incubated with serum from CVF-treated mice added. All error bars indicate mean ± SEM.

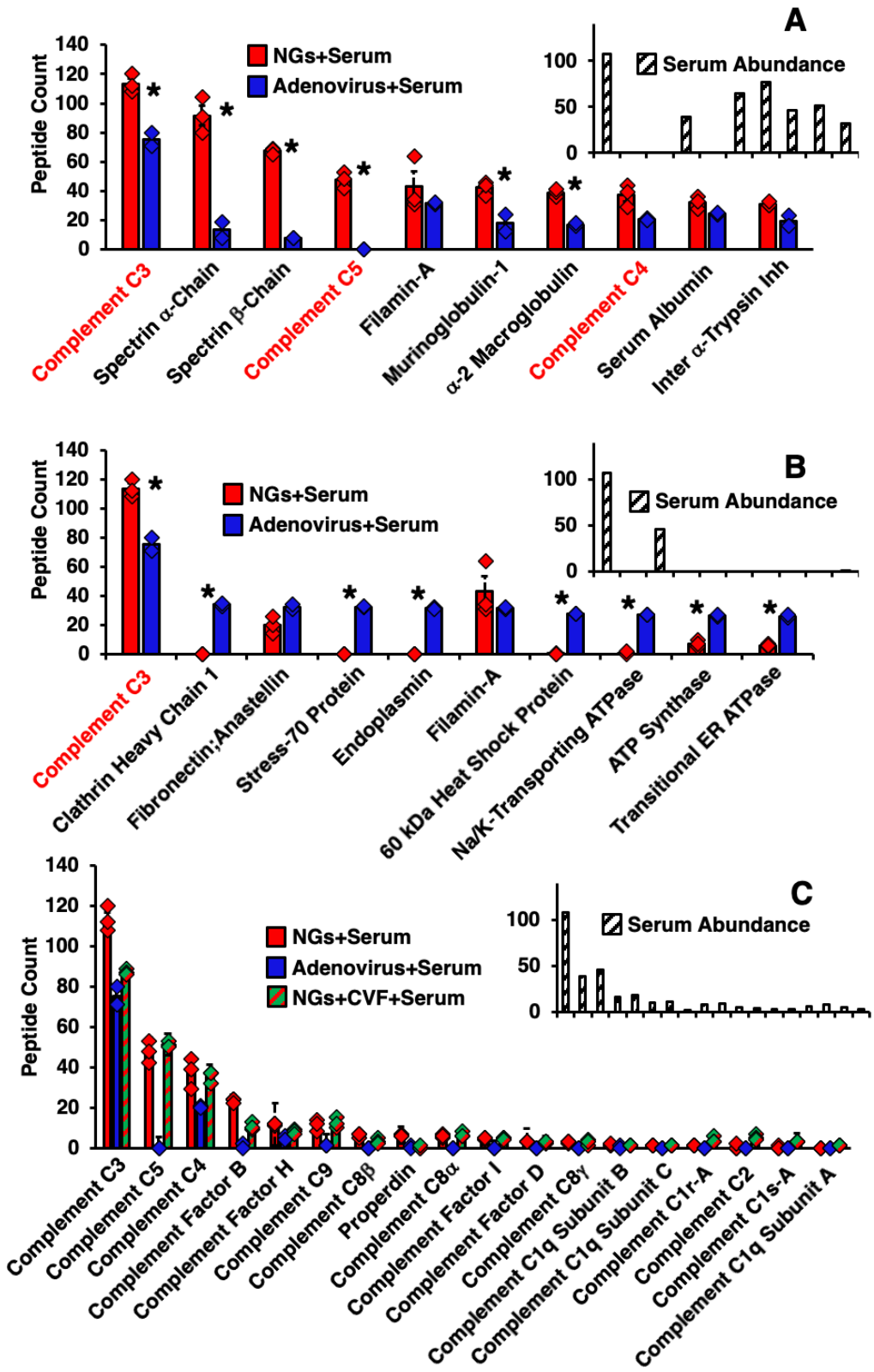

Supplementary Figure 30

Mass Spectromotry Characterization of Serum Opsonization of Lysozyme-Dextran Nanogels and Human Adenovirus. (a) Peptide counts from mass spectrometry data

indicating the ten most abundant proteins identified on the surface of NGs (n=3 nanoparticle-serum preparations) after incubation with mouse serum, with quantities of the same proteins on human adenovirus capsids (n=3 nanoparticle-serum preparations) included for comparison (**: left to right, $p=3.4x10^{-8}$, $p<1x10^{-10}$, $p<1x10^{-10}$, $p<1x10^{-10}$, $p=0.0002$, $p=0.001$, $p=0.02$*). NGs were opsonized by significantly greater quantities of complement proteins C3 and C5 than adenovirus. (b) Peptide counts from mass spectrometry data indicating the ten most abundant proteins identified on the surface of human adenovirus capsids after incubation with mouse serum, with quantities of the same proteins on lysozyme-dextran nanogels included for comparison. Excluding Filamin-A and complement protein C3, abundant proteins on adenovirus were not found on lysozyme-dextran nanogels (**: left to right, $p<1x10^{-10}$, $p=5.4x10^{-10}$, $p=1.7x10^{-9}$, $p=4x10^{-9}$, $p=9.3x10^{-8}$, $p=3.7x10^{-7}$, $p=0.0001$, $p=0.00006$*). (c) Peptide counts indicating mass spectrometry quantification of complement proteins on the surface on lysozyme-dextran nanogels and human adenovirus capsids after incubation with mouse serum, with peptide counts on lysozyme-dextran nanogels after incubation with complement-depleted cobra venom factor (CVF)-treated mouse serum (n=3 nanoparticle-serum preparations) represented for comparison. For all measured peptides, levels of complement proteins on adenovirus were lower than those on nanogels after incubation with *complement-depleted* serum. Insets: Mass spectrometry measurement of abundance of corresponding proteins in serum preparations. Statements of statistical significance are based on two-way ANOVA with Sidak's multiple comparisons test. All error bars indicate mean ± SEM.

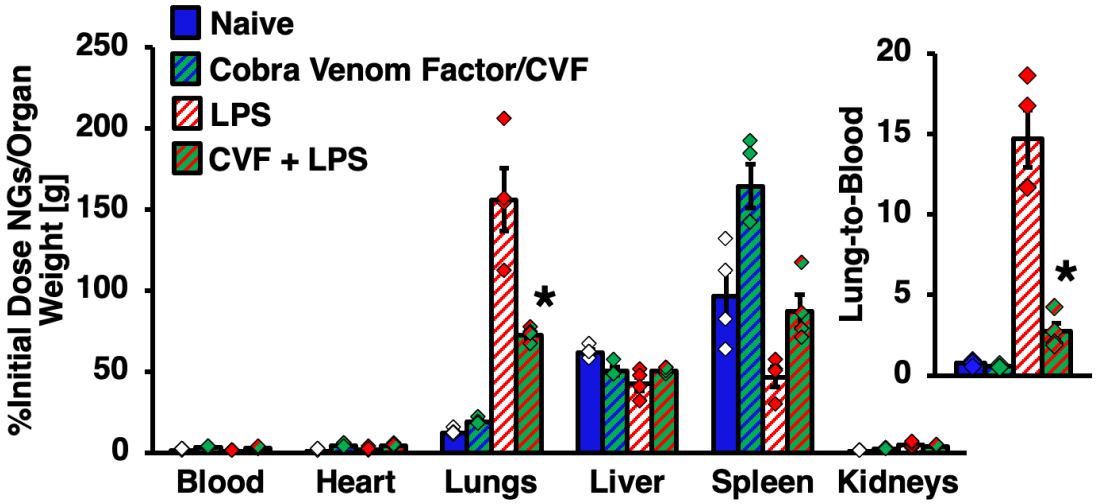

Supplementary Figure 31

Biodistributions of Lysozyme-Dextran Nanogels in Mice Treated with Cobra Venom Factor and/or Intravenous LPS. In vivo biodistributions of NGs in; naïve mice (n=4 animals); mice treated with CVF (n=4 animals); mice treated with intravenous LPS (n=4 animals) and; mice treated with intravenous LPS and CVF (n=4 animals). Data show that CVF reduces nanogel uptake in inflamed lungs, as in figure 4e, but with addition of heart, kidneys and lung:blood data. For comparison of LPS and CVF+LPS data, **: $p=1.6x10^{-10}$ for lungs and $p=5.2x10^{-6}$ for lungs:blood*. Statements of statistical

significance are based on two-way ANOVA with Tukey's multiple comparisons test. All error bars indicate mean ± SEM.

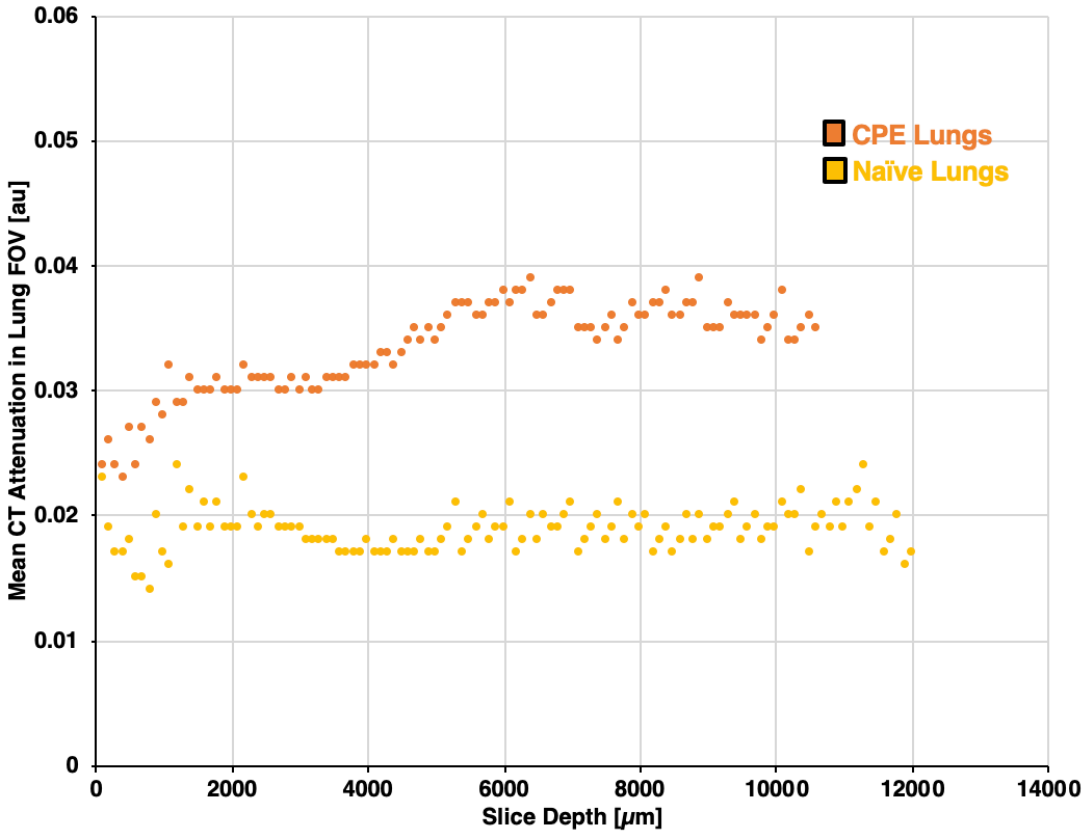

Supplementary Figure 32

Quantification of CT Attenuation in Edematous and Naïve Mouse Lungs. CT images, depicted in three-dimensional reconstructions in figure 5a in the main text, were obtained for a naïve mouse and a mouse afflicted with cardiogenic pulmonary edema. For each axial slice in the CT images, mean CT attenuation was determined in manually drawn fields of view encompassing the lungs. Mean CT attenuation is plotted above as a function of slice depth. Average attenuation over all slices is depicted in figure 5c in the main text.

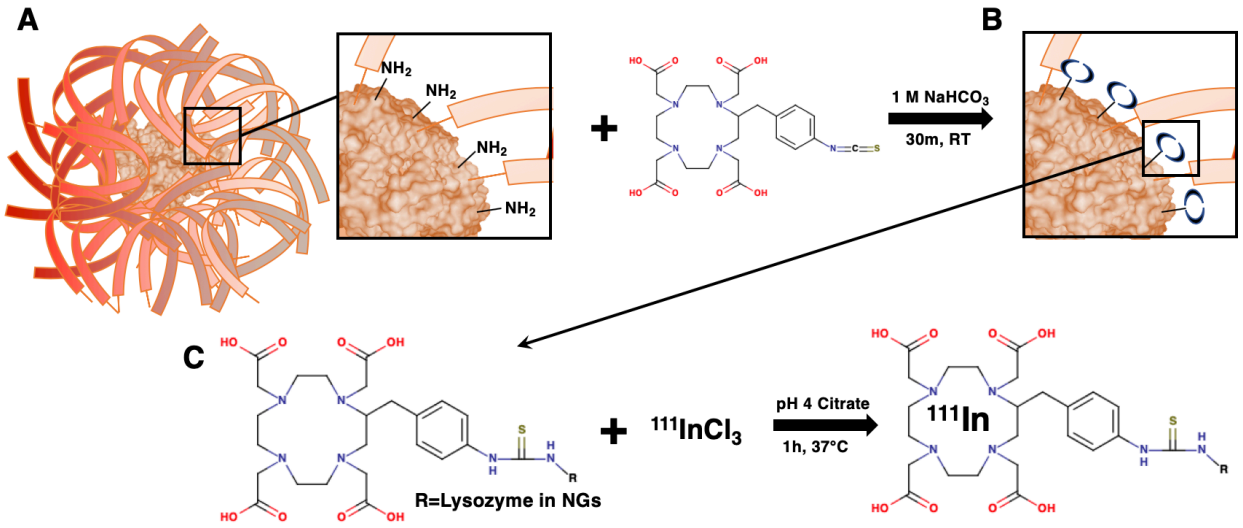

Supplementary Figure 33

Schematic of Lysozyme-Dextran Nanogel Functionalization with Chelate and Subsequent Labeling with ^{111}In. (a) NGs were conjugated to S-2-(4-Isothiocyanatobenzyl)-1,4,7,10-tetraazacyclododecane tetraacetic acid (p-SCN-Bn-DOTA, via isothiocyanate reaction with amine groups and sulfhydryl groups on lysozyme in the nanogel core, yielding (b) NGs with chelate groups after removal of free chelate by centrifugation. (c) Chelate-conjugated NGs were exposed to $^{111}InCl_3$ in metal-free pH 4 citrate buffer for one hour at 37°C to yield ^{111}In-labeled nanoparticles. Unchelated ^{111}In was removed by DTPA treatment and centrifugation, prior to verifying efficiency and stability of ^{111}In chelation by thin film chromatography.

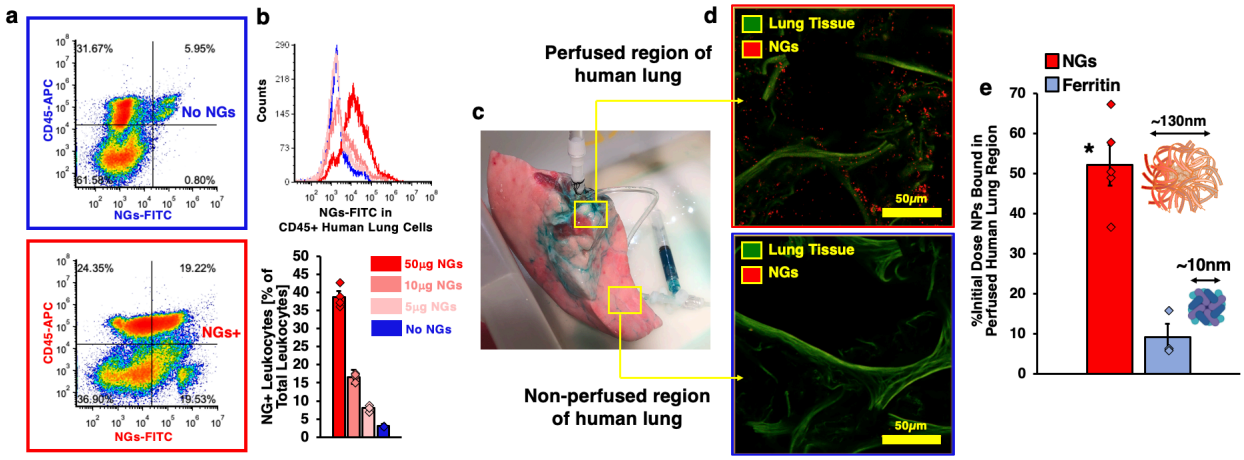

Supplementary Figure 34

Uptake of NAPs in Ex Vivo Human Lungs. (a-b) Flow cytometry characterization of single cell suspensions prepared from donor human lungs rejected for transplant. (a) CD45 staining vs. NG uptake in cells for cells without NGs (n=4 cell-NG preparations) and cells incubated with NGs (50µg NGs per $2x10^6$ cells, n=4 cell-NG preparations). (b) Upper panel: Nanogel fluorescence in CD45-positive cells, after cell incubation with different quantities of NGs. Lower panel: Percentage of leukocytes with NGs after incubation of cells with different quantities of NGs (n=4 cell-NG preparations for each

NG quantity). (c) Photograph depicting cannulation of human lung for nanoparticle and tissue dye infusion, with green tissue dye indicating perfused regions of the lung. (d) Micrographs indicating fluorescent nanogel uptake in perfused, but not non-perfused, regions of human lung. A single segment was taken from each type of region in one lung lobe to produce images in (d). (e) Radiotracer-determined quantity of nanoparticle uptake in human lungs for lysozyme-dextran nanogels (n=5 injections in lung lobes from separate donors) and ferritin (n=3 injections in lung lobes from separate donors, ferritin schematic created with BioRender.com). In experiments with ferritin, lysozyme-dextran nanogels and ferritin were simultaneously infused in the same lungs (**: p=0.00097*). Statistical significance is based on unpaired t-test and all error bars indicate mean ± SEM.

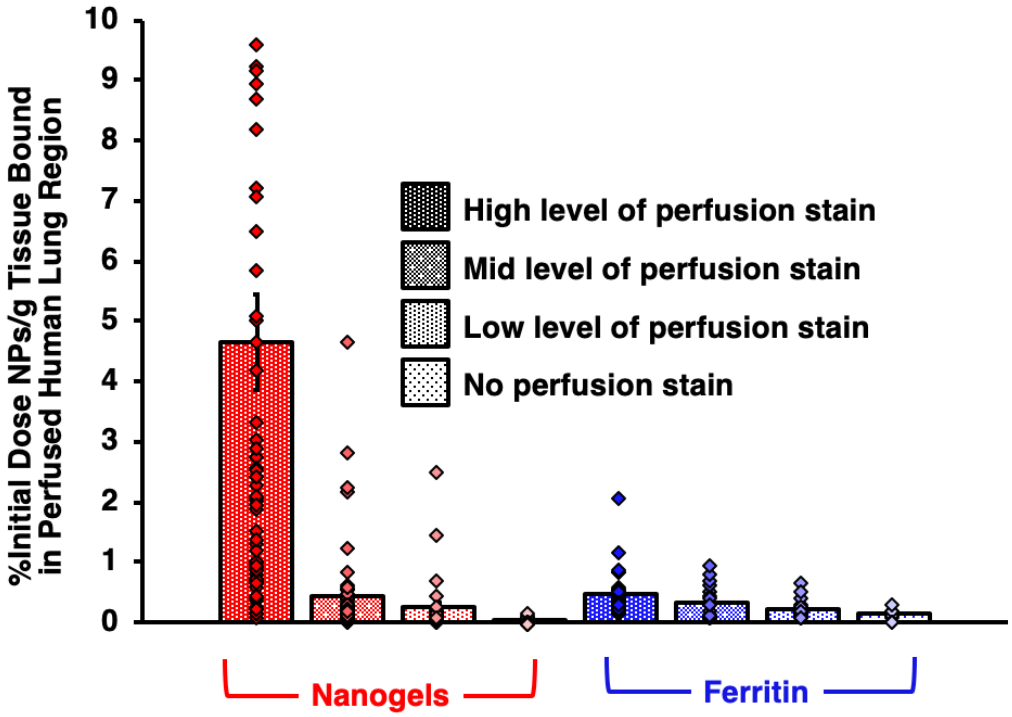

Supplementary Figure 35

Lysozyme-Dextran Nanogel and Ferritin Nanocage Uptake in Human Lungs as a Function of Tissue Perfusion. Human lungs were divided into ~1g segments according to levels of staining induced by tissue dye introduced via the same catheter used for nanoparticle administration, with staining divided by the experimenter into high, medium, and low levels of tissue staining. NGs: n=68 high-perfusion segments, n=62 mid-perfusion segments, n=35 low-perfusion segments, and n=17 unstained segments. Ferritin: n=36 high-perfusion segments, n=20 mid-perfusion segments, n=18 low-perfusion segments, and n=8 unstained segments. Nanoparticle retention in each segment was subsequently assessed by detection of radiolabel (^{125}I on NGs, ^{131}I on ferritin). Levels of NG or ferritin retention in each type of segment are plotted above, indicating that NG retention is highly focused in more directly perfused tissue. All error bars indicate mean ± SEM.

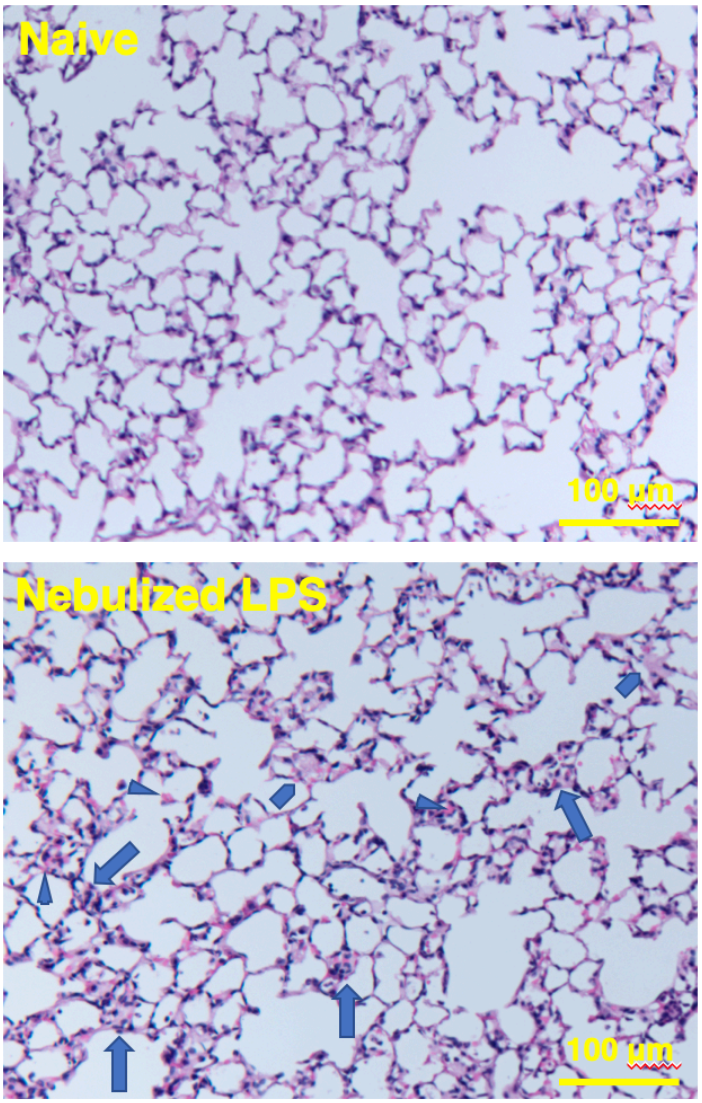

Supplementary Figure 36

Hematoxylin and Eosin Staining of Lung Sections from Naïve Mice and Mice After Nebulized LPS Inhalation. Histology data indicates severity of the acute lung injury after LPS inhalation. A naïve mouse (top panel) and a mouse that had been exposed to nebulized LPS (lower panel) were sacrificed at 24 hours post-LPS. The lungs were paraformaldehyde fixed and paraffin embedded, sliced to 20 micron thickness, and stained with hematoxylin & eosin. The nebulized LPS lungs have diffuse neutrophilia (increased number of purple puncta throughout), with severe airspace infiltration by neutrophils (arrows), formation of pink hyaline membranes (oblong pentagons), and punctate hemorrhage (triangles).

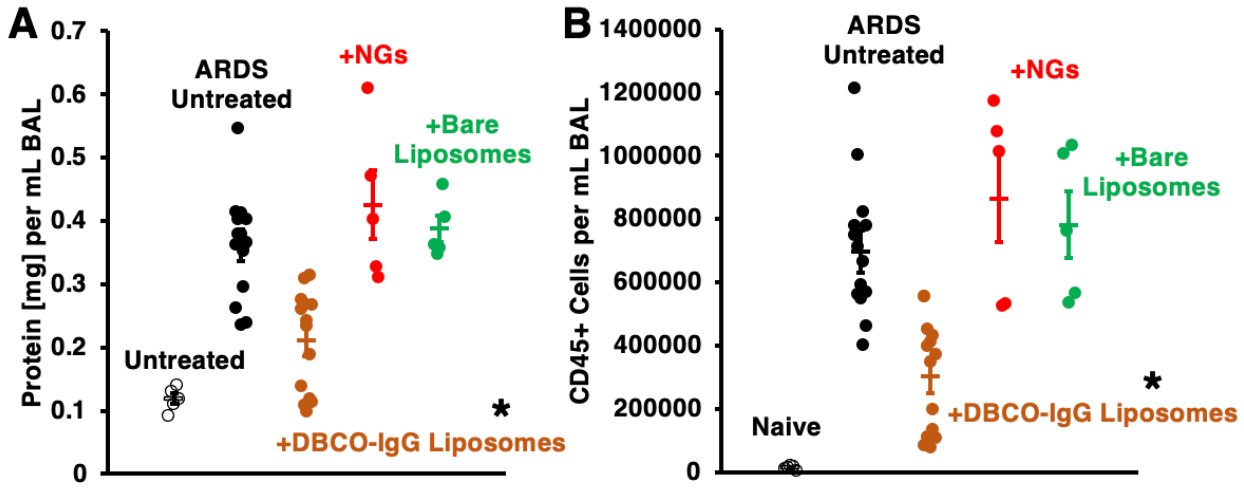

Supplementary Figure 37

Raw Quantification of Pulmonary Edema and Leukocyte Leak into Alveoli in Model ARDS with Different Nanoparticle Treatments. Data as in Figures 6a and 6b, represented in terms of raw quantity of protein and leukocyte accumulation in alveoli under naïve, injured, and different nanoparticle treatment conditions. See Figures 6a and 6b for numbers of replicates. In (a), **: p=0.00007, 0.00005, and 0.0009* for comparison of DBCO-IgG liposome treatment with sham treatment, NG treatment, and bare liposome treatment, respectively. In (b), **: p=0.00007, 0.00005, and 0.0006* for comparison of DBCO-IgG liposome treatment with sham treatment, NG treatment, and bare liposome treatment, respectively. All error bars indicate mean ± SEM.

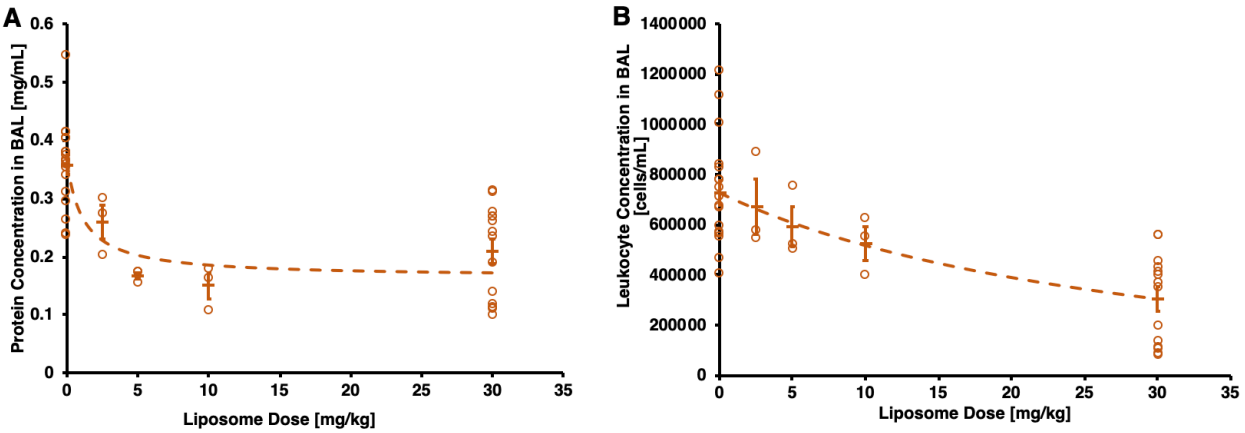

Supplementary Figure 38

Dose-Response for Raw Quantification of Pulmonary Edema and Leukocyte Leak into Alveoli in Model ARDS with DBCO-IgG Liposome Treatment. Data as in Figures 6c and 6d, represented in terms of raw quantity of protein and leukocyte accumulation in alveoli after treatment with different doses of DBCO-IgG liposomes. See Figures 6c and 6d for numbers of replicates. All error bars indicate mean ± SEM.

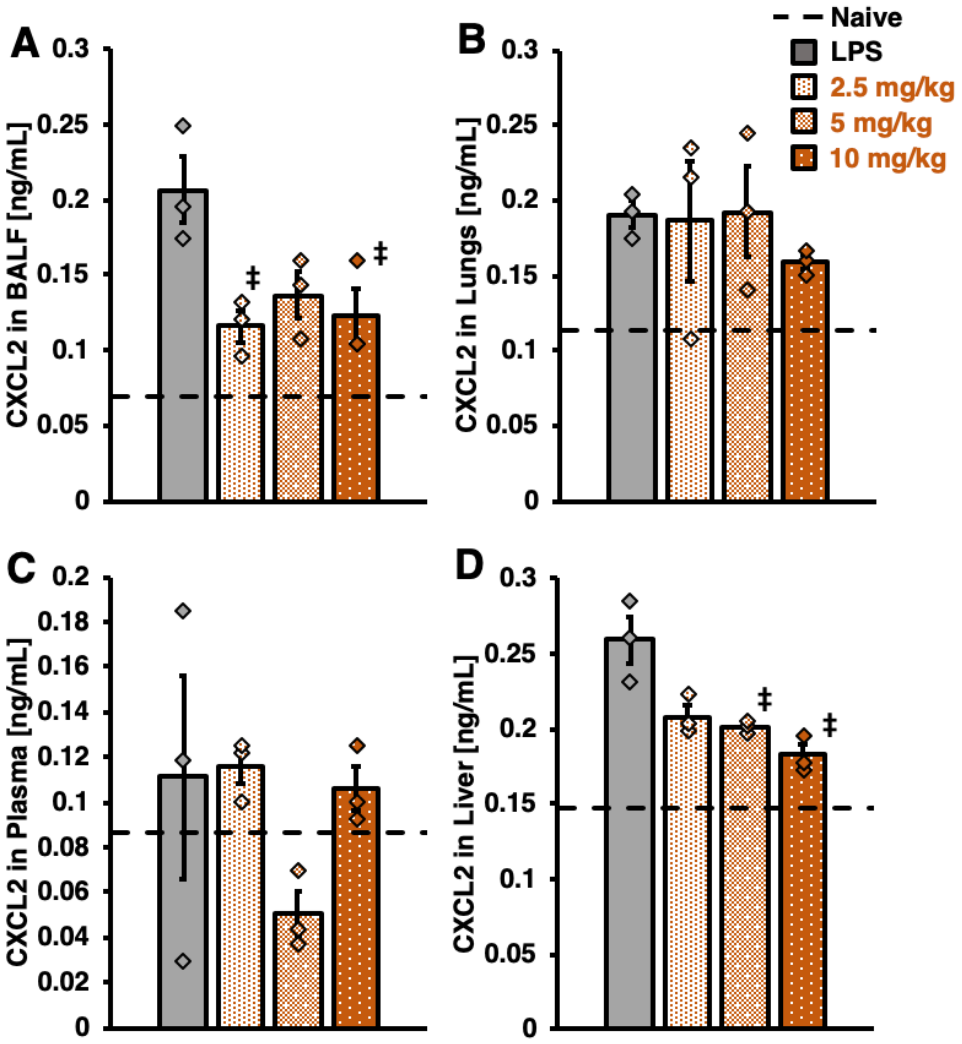

Supplementary Figure 39

Dose-Response for Chemokine CXCL2 Concentration in Bronchoalveolar Lavage Fluid, Lung Tissue, Plasma, and Liver Tissue after DBCO-IgG Liposome Treatment in Model ARDS. Chemokine CXCL2 levels in different tissues of mice with model ARDS (n=3 animals) treated with 2.5 mg/kg (n=3 animals), 5 mg/kg (n=3 animals), or 10 mg/kg (n=3 animals) liposomes. Dashed line indicates CXCL2 levels in naïve mice. Data in (a) is equivalent to data in Figure 1e (*‡: p=0.024 and 0.034 f*or BALF CXCL2 levels in untreated mice vs. 2.5 mg/kg and 10 mg/kg DBCO-IgG liposomes treatment, respectively). For data in (d), *‡: p=0.0098 and 0.0017* for liver CXCL2 levels in untreated mice vs. 5 mg/kg and 10 mg/kg DBCO-IgG liposomes treatment, respectively. Statistical significance is derived from one-way ANOVA with Tukey's multiple comparisons test. All error bars indicate mean ± SEM.

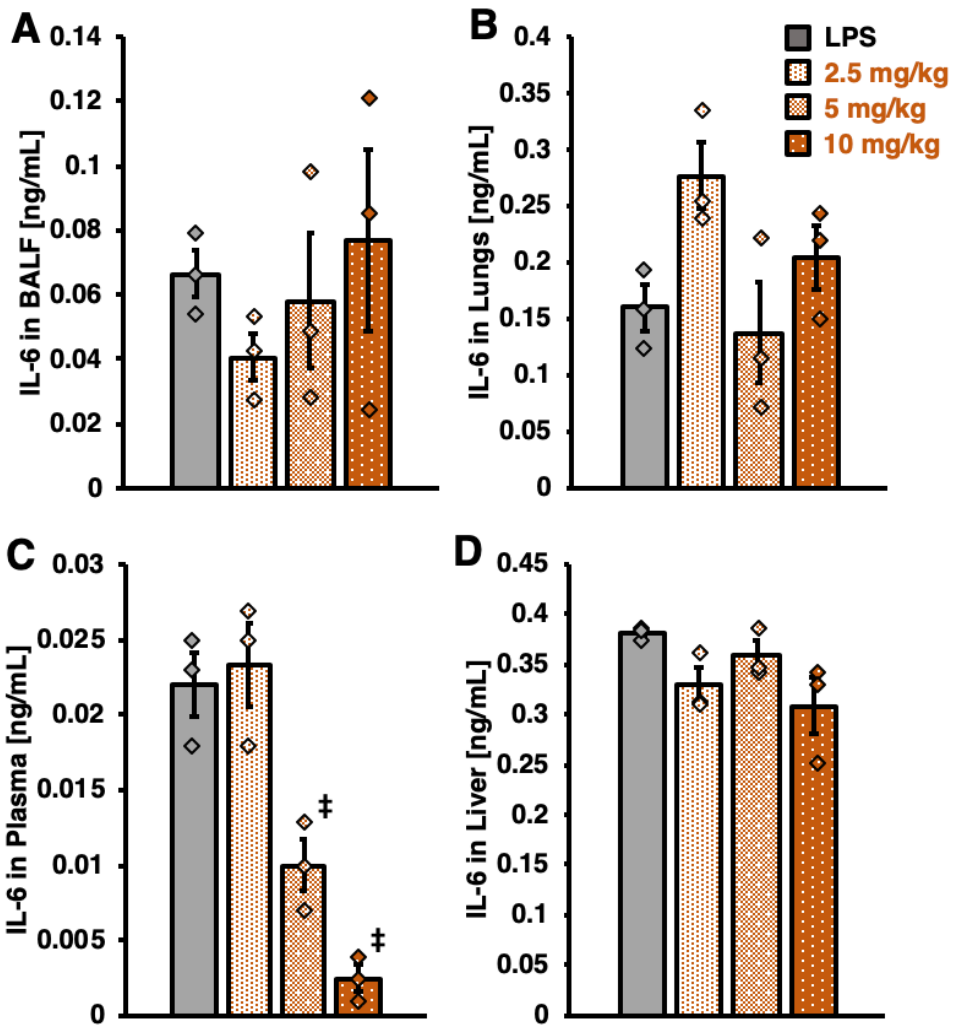

Supplementary Figure 40

Dose-Response for Cytokine IL-6 Concentration in Bronchoalveolar Lavage Fluid, Lung Tissue, Plasma, and Liver Tissue after DBCO-IgG Liposome Treatment in Model ARDS. Cytokine IL-6 levels in different tissues of mice with model ARDS (n=3 animals) treated with 2.5 mg/kg (n=3 animals), 5 mg/kg (n=3 animals), or 10 mg/kg (n=3 animals) liposomes. For data in (c), *‡: p=0.011 and 0.0005* for plasma CXCL2 levels in untreated mice vs. 5 mg/kg and 10 mg/kg DBCO-IgG liposomes treatment, respectively. Statistical significance is derived from one-way ANOVA with Tukey's multiple comparisons test. All error bars indicate mean ± SEM.

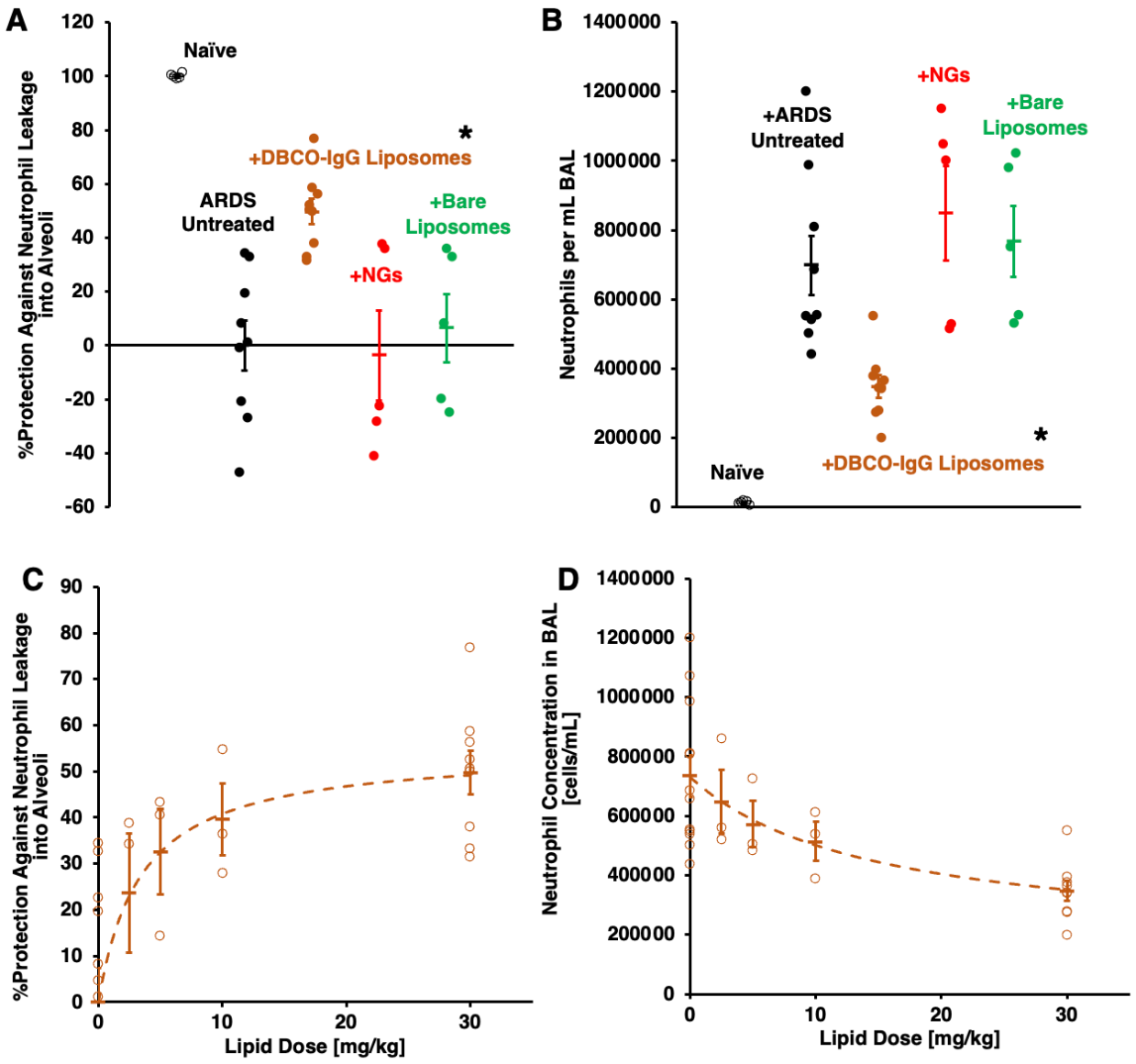

Supplementary Figure 41

Quantification of Neutrophil Leak into Alveoli in Model ARDS with Different Nanoparticle Treatments. (a-b) Concentration of neutrophils in BAL fluid of naïve mice (n=5 animals), untreated mice with model ARDS (n=9 animals), and mice with model ARDS after treatment with DBCO-IgG liposomes (n=9 animals), NGs (n=5 animals), and bare liposomes (n=5 animals). In (a), quantities are represented as degree of protection against neutrophil infiltration into alveoli, as extrapolated from levels in naïve mice (100% protection) and untreated mice with LPS-induced injury (0% protection). (b) Data as in (a), represented as raw quantities of neutrophils in alveoli. In (a), **: p=0.0015, 0.0043, and 0.027* for comparison of DBCO-IgG liposome treatment with sham treatment, NG treatment, and bare liposome treatment, respectively. In (b), **: p=0.0094, 0.0013, and 0.0083* for comparison of DBCO-IgG liposome treatment with sham treatment, NG treatment, and bare liposome treatment, respectively. (c-d) Dose-response for neutrophil infiltration in alveoli of LPS-injured mice treated with different

doses of DBCO-IgG liposomes (n=3 animals for 2.5 mg/kg, 5 mg/kg, and 10 mg/kg liposome doses). Data in (c) represent protection against neutrophil infiltration and data in (d) represent raw quantities of neutrophils in the alveoli. All error bars indicate mean ± SEM.

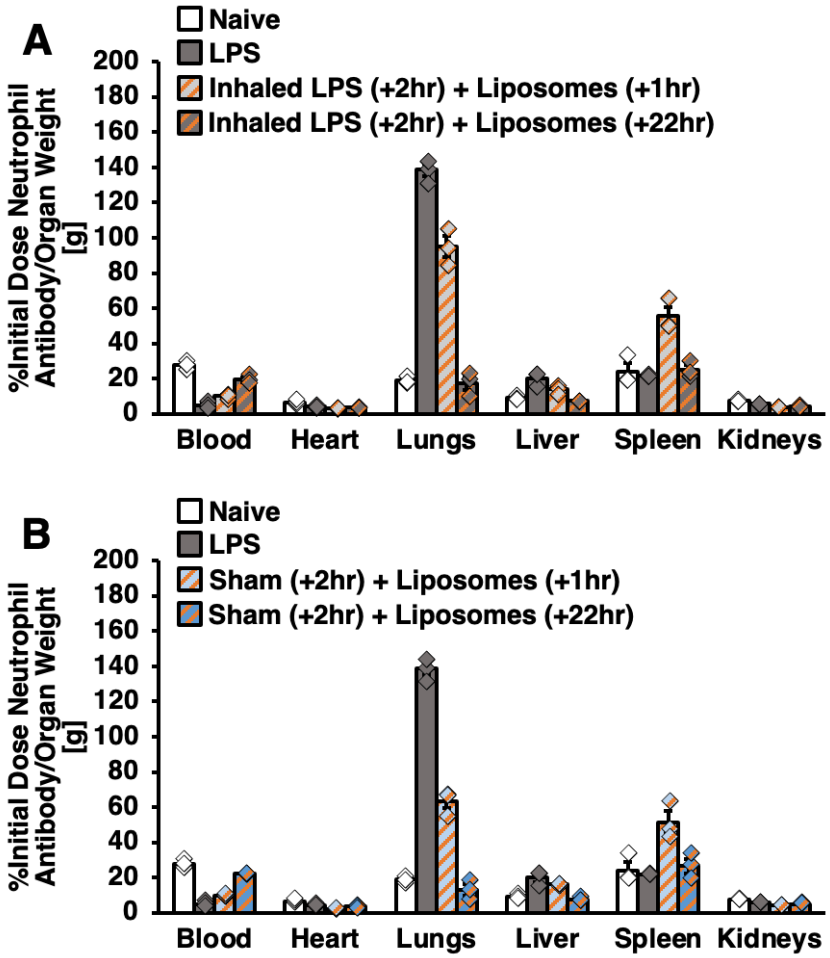

Supplementary Figure 42

Intravascular Neutrophil Tracing in Mice After DBCO-IgG Liposome Treatment. Representation of data as in Figure 6g (a), with tracing of anti-Ly6G neutrophil antibody in sham-injured liposome-treated mice added for comparison (b). n=3 animals for all groups. All error bars indicate mean ± SEM.

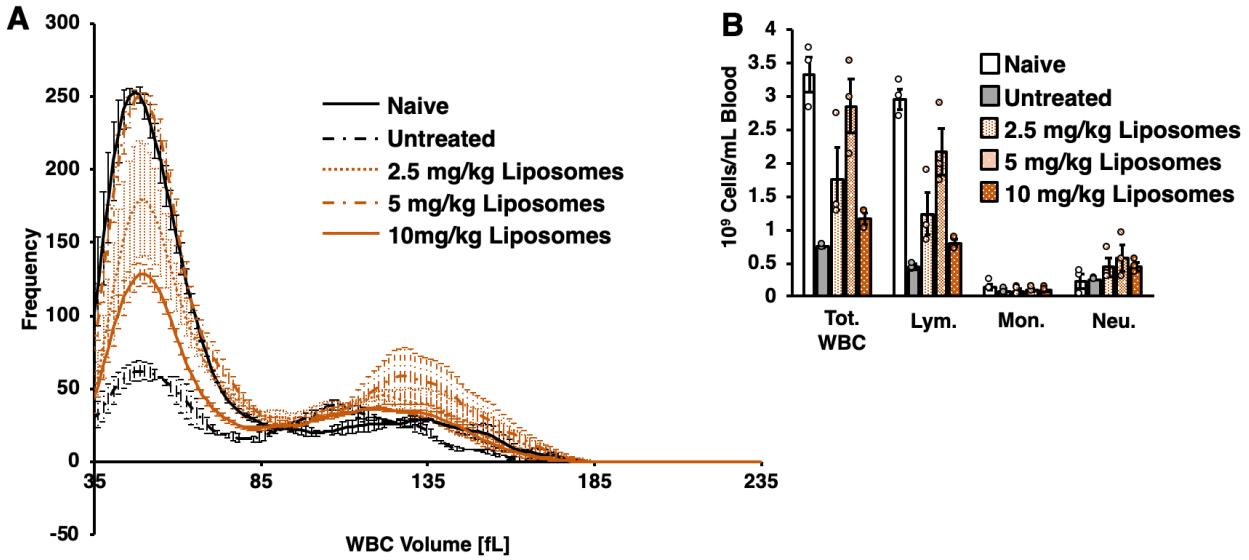

Supplementary Figure 43

Complete Blood Count Analysis Assessment of Circulating Leukocyte Concentrations and Size Distributions in Mice Treated with DBCO-IgG Liposomes and/or LPS. (a) Complete blood count analysis data indicating circulating leukocyte size distributions in naïve mice (n=3 animals), LPS-injured mice (n=3 animals), mice treated with 2.5 mg/kg DBCO-IgG liposomes (n=3 animals), mice treated with 5 mg/kg DBCO-IgG liposomes (n=3 animals), and mice treated with 10 mg/kg DBCO-IgG liposomes (n=3 animals). Blood was sampled 22 hours after liposome treatment and 24 hours after induction of LPS injury. Leftmost peak indicates circulating lymphocytes and rightmost peak indicates circulating neutrophils. (b) Complete blood count quantification of circulating leukocyte concentrations as derived from data in (a). Data for 10 mg/kg liposome dose and untreated controls are as in Figure 6h. All error bars indicate mean ± SEM.

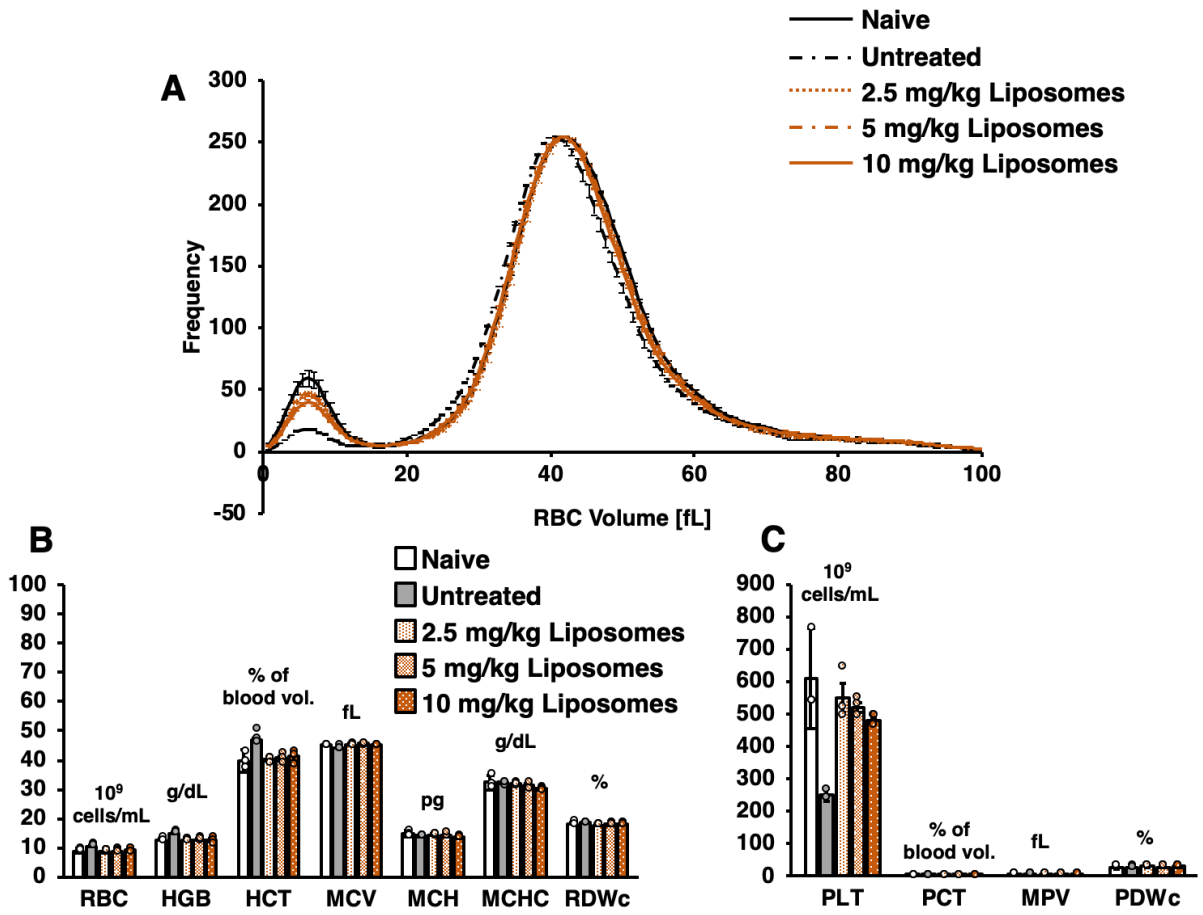

Supplementary Figure 44

Complete Blood Count Analysis Assessment of Circulating Platelet and Red Blood Cell Concentrations and Size Distributions in Mice Treated with DBCO-IgG Liposomes and/or LPS. (a) Complete blood count analysis data indicating circulating platelet (leftmost peak) and red cell (larger rightmost peak) size distributions in naïve mice (n=3 animals), LPS-injured mice (n=3 animals), mice treated with 2.5 mg/kg DBCO-IgG liposomes (n=3 animals), mice treated with 5 mg/kg DBCO-IgG liposomes (n=3 animals), and mice treated with 10 mg/kg DBCO-IgG liposomes (n=3 animals). Blood sampled 22 hours after liposome treatment and 24 hours after induction of LPS injury. (b) Complete blood count quantification of circulating red cell concentrations and properties as derived from data in (a). RBC = red blood cell concentration, HGB = hemoglobin concentration, HCT = red blood cell hematocrit, MCV = mean red blood cell volume, MCH = mean red blood cell hemoglobin content, MCGH = mean red blood cell hemoglobin concentration, RDWc = width of the red blood cell size distribution. (c) Platelet concentrations and properties for the same experimental groups as depicted in (b). PLT = platelet concentration, PCT = platelet hematocrit, MPV = mean platelet volume, PDWc = width of the platelet size distribution. All error bars indicate mean ± SEM.

Supplementary Figure 45
Dose-Response for Weight Change Over the Course of Model ARDS in Mice Treated with DBCO-IgG Liposomes. Data indicates no significant change from untreated values (n=9 animals) for all tested doses of DBCO-IgG liposomes (n=3 animals for all tested doses). All error bars indicate mean ± SEM.

References (Supplementary Figures)

1. Williams, A. E. & Chambers, R. C. The mercurial nature of neutrophils: still an enigma in ARDS? *Am. J. Physiol. Lung Cell Mol. Physiol.* **306,** L217-30 (2014).
2. Wright, H. L., Moots, R. J., Bucknall, R. C. & Edwards, S. W. Neutrophil function in inflammation and inflammatory diseases. *Rheumatology* **49,** 1618–1631 (2010).
3. Grommes, J. & Soehnlein, O. Contribution of neutrophils to acute lung injury. *Mol Med* **17,** 293–307 (2011).
4. Mantovani, A., Cassatella, M. A., Costantini, C. & Jaillon, S. Neutrophils in the activation and regulation of innate and adaptive immunity. *Nat. Rev. Immunol.* **11,** 519–531 (2011).
5. Downey, G. P., Worthen, G. S., Henson, P. M. & Hyde, D. M. Neutrophil sequestration and migration in localized pulmonary inflammation. Capillary localization and migration across the interalveolar septum. *Am. Rev. Respir. Dis.* **147,** 168–176 (1993).
6. Craig, A., Mai, J., Cai, S. & Jeyaseelan, S. Neutrophil recruitment to the lungs during bacterial pneumonia. *Infect. Immun.* **77,** 568–575 (2009).
7. Yipp, B. G. *et al.* The Lung is a Host Defense Niche for Immediate Neutrophil-Mediated Vascular Protection. *Sci. Immunol.* **2,** (2017).

Supplementary Discussion

Due to space limitations, the discussion in the main text could not include a full description of the immunological implications for NAP administration. Therefore, below we discuss several topics related to immunological implications, including how NAPs interact with other immune cells, whether similar effects are seen in inflammation outside the lungs, and the potential immunological side effects of NAPs.

This study focused on nanoparticle tropism for neutrophils in the pulmonary vasculature. In response to inflammation, neutrophils and other leukocytes marginate in vascular beds.[1] During many types of systemic inflammation, such as sepsis and ARDS, the pulmonary vasculature retains the largest amount of marginated neutrophils.[2–5] Pulmonary marginated neutrophils are therefore important in many diseases. The clinical importance and abundance of pulmonary neutrophils motivated our focus on the lungs in studies of nanoparticle tropism for neutrophils. However, marginated neutrophils can appear in other vascular beds during more localized inflammation.[6] Indeed, NAPs have tropism for neutrophils accumulating in the foot following footpad CFA injection (Supplementary Figures 8-9). Therefore, NAP tropism for neutrophils, demonstrated extensively in the lungs, may apply to other niches and disorders in which marginated neutrophils are prominent. Just as the lungs are an important, but not necessarily unique, niche for NAP tropism, NAPs may accumulate in or affect leukocytes other than neutrophils. For instance, ~10% of DBCO-IgG liposome uptake in the lungs is attributable to non-neutrophil leukocytes (Figure 5e, Supplementary Figure 21d). Neutrophils are numerically dominant in acute inflammation, but marginated leukocyte populations can include monocytes and even B cells. Future studies exploring applicability of NAPs in different cell types and niches will advance the engineering of NAP-based therapeutics.

The above being said, DBCO-IgG liposomes also have systemic effects that aren't confined to neutrophils. Namely, the liposomes suppress cytokine IL-6 levels in plasma and chemokine CXCL2 levels in the alveoli and liver, relative to elevated values induced by LPS injury. Both of these signaling molecules are linked to neutrophil function. However, CXCL2 is secreted by macrophages and monocytes, so CXCL2 suppression may reflect NAP effects on these other cell types.[7,8] Additionally, IL-6 has broad effects in macrophages, hepatocytes, and endothelial cells, so IL-6 suppression by DBCO-IgG liposomes may have a range of consequences.[9] Further indicating a breadth of systemic effects, DBCO-IgG liposomes altered circulating concentrations of lymphocytes, platelets, and red blood cells. As with effects on IL-6 and CXCL2, DBCO-IgG liposome effects on circulating cells reversed changes induced by LPS.

While potentially beneficial in a disease like ARDS, NAP-induced changes to neutrophil function, inflammatory signaling, and circulating blood cell concentrations should be understood as side effects that may also have deleterious repercussions. For instance, neutrophils are critical to host defense and displacement of neutrophils from the lungs may worsen the effects of a bacterial infection. These side effects were noted for DBCO-IgG liposomes, but not NGs.

Many nanoparticles share properties with NAPs, so future studies will likely show that other NAP-like nanoparticles accumulate in the lungs following inflammatory insult. For such nanoparticles, targeting profiles documented in naïve or, for instance, tumor

model studies, may be greatly changed by, for instance, bacterial infection. Our study can thus be taken as an exhortation to reevaluate the biodistributions of nanoparticles with NAP-like properties, to assess their tendency to behave like NAPs and redistribute to marginated neutrophils during acute inflammation.

References (Supplementary Discussion)

1. Brown, K. A. *et al.* Neutrophils in development of multiple organ failure in sepsis. *Lancet* **368,** 157–169 (2006).
2. Wright, H. L., Moots, R. J., Bucknall, R. C. & Edwards, S. W. Neutrophil function in inflammation and inflammatory diseases. *Rheumatology* **49,** 1618–1631 (2010).
3. Mayadas, T. N., Cullere, X. & Lowell, C. A. The multifaceted functions of neutrophils. *Annu. Rev. Pathol.* **9,** 181–218 (2014).
4. Mantovani, A., Cassatella, M. A., Costantini, C. & Jaillon, S. Neutrophils in the activation and regulation of innate and adaptive immunity. *Nat. Rev. Immunol.* **11,** 519–531 (2011).
5. Yipp, B. G. *et al.* The Lung is a Host Defense Niche for Immediate Neutrophil-Mediated Vascular Protection. *Sci. Immunol.* **2,** (2017).
6. Liew, P. X. & Kubes, P. The neutrophil's role during health and disease. *Physiol. Rev.* **99,** 1223–1248 (2019).
7. De Filippo, K. *et al.* Mast cell and macrophage chemokines CXCL1/CXCL2 control the early stage of neutrophil recruitment during tissue inflammation. *Blood* **121,** 4930–4937 (2013).
8. Qin, C.-C., Liu, Y.-N., Hu, Y., Yang, Y. & Chen, Z. Macrophage inflammatory protein-2 as mediator of inflammation in acute liver injury. *World J. Gastroenterol.* **23,** 3043–3052 (2017).
9. Tanaka, T., Narazaki, M. & Kishimoto, T. IL-6 in inflammation, immunity, and disease. *Cold Spring Harb. Perspect. Biol.* **6,** a016295 (2014).

Supplementary Methods

Lysozyme-Dextran Nanogel Synthesis

Lysozyme-dextran nanogels (LDNGs) were synthesized as previously described.[1,2] 70 kDa rhodamine-dextran or FITC-dextran (Sigma) and lysozyme from hen egg white (Sigma) were dissolved in deionized and filtered water at a 1:1 or 2:1 mol:mol ratio, and pH was adjusted to 7.1 before lyophilizing the solution. For Maillard reaction between lysozyme and dextran, the lyophilized product was heated for 18 hours at 60°C, with 80% humidity maintained via saturated KBr solution in the heating vessel. Dextran-lysozyme conjugates were dissolved in deionized and filtered water to a concentration of 5 mg/mL, and pH was adjusted to 10.70 or 11.35. Solutions were stirred at 80°C for 30 minutes. Diameter of LDNGs was evaluated with dynamic light scattering (DLS, Malvern) after heat gelation. Particle suspensions were stored at 4°C.

Crosslinked Protein Nanoparticle Synthesis

Crosslinked protein nanoparticles and nanorods were prepared using previously reported electrohydrodynamic jetting techniques.[3] The protein nanoparticles were prepared using bovine serum albumin, human serum albumin, human lysozyme, human transferrin, or human hemoglobin (all proteins were purchased from Sigma). Protein nanorods were prepared using chemically modified human serum albumin. For electrohydrodynamic jetting, protein solutions were prepared by dissolving the protein of interest at a 7.5 w/v% (or 2.5 w/v% for protein nanorods) concentration in a solvent mixture of DI water and ethylene glycol with 4:1 (v/v) ratio. The homo-bifunctional amine-reactive crosslinker, O,O′-bis[2-(N-succinimidyl-succinylamino)ethyl]polyethylene glycol with molecular weight of 2kDa (NHS-PEG-NHS, Sigma) was mixed with the protein solution at 10 w/w%. Protein nanoparticles were kept at 37°C for 7 days for completion of the crosslinking reaction. The as-prepared protein nanoparticles were collected in PBS buffer and their size distribution was analyzed using dynamic light scatting (DLS, Malvern).

To label albumin NPs for fluorescence tracing, NHS ester Alexa Fluor 488 was incubated with nanoparticles at 1:25 mass:mass fluorophore:nanoparticle ratio for two hours on ice. Excess fluorophore was removed from nanoparticles by 3-fold centrifugation at 16000xg for 15 minutes followed by washing with PBS.

Glutamate-Tagged Green Fluorescent Protein Nanoparticle Synthesis

Glutamic acid residues (E20-tag) were inserted at the C-terminus of enhanced green fluorescent protein (E-GFP) through restriction cloning and site-directed mutagenesis as previously reported.[4] Proteins were expressed in *E. coli* BL21(DE3) strain (Millipore #694513) using standard protein expression protocol. Briefly, protein expression was carried out in 2xYT media with an induction condition of 1 mM IPTG and 18°C for 16 h. At this point, the cells were harvested, and the pellets were lysed using 1% Triton-X-100 (30 min, 37°C)/DNase-I treatment (10 minutes). Proteins were purified using HisPur cobalt columns. After elution, proteins were preserved in PBS buffer. The purity of native proteins was determined using 8% SDS–PAGE gel.

Polymers (PONI) were synthesized by ring-opening metathesis polymerization using third generation Grubbs' catalyst as previously described.[5] In brief, solutions in dichloromethane of guanidium functionalized monomer and Grubbs' catalyst were placed under freeze thawing cycles for degassing. After warming the solutions to room temperature, the degassed monomer solutions were administrated to degassed catalyst solutions and allowed to stir for 30 minutes. The polymerization reaction was terminated by the addition of excess ethyl vinyl ether. The reaction mixture was further stirred for another 30 min. The resultant polymers were precipitated from excess hexane or diethyl ether anhydrous, filtered, washed, and dried under vacuum to yield a light-yellow powder. polymers were characterized by ^{1}H NMR and gel permeation chromatography (GPC) to assess chemical compositions and molecular weight distributions, respectively. Subsequent to deprotection of Boc functionalities, polymer was dissolved in the DCM with the addition of TFA at 1:1 ratio. The reaction was allowed to stir for 4 hours and dried under vacuum. Excess TFA was removed by azeotropic distillation with methanol. Afterwards, the resultant polymers were re-dissolved in DCM and precipitated in anhydrous diethyl ether, filtered, washed and dried. Polymers were then dissolved in

water and transferred to Biotech CE dialysis tubing membranes with a 3000 g/mol cutoff and dialyzed against RO water (2–3 days). The polymers were then lyophilized dried to yield a light white powder.

PONI polymer/E-tag protein nanocomposites (PPNCs) were prepared in polypropylene microcentrifuge tubes (Fisher) through a simple mixing procedure. 0.5625 nmol of 54 kDa PONI was incubated with 0.45 nmol of EGFP at room temperature for 10 minutes prior to dilution to 200 μL in sterile PBS and subsequent injection. Similarly, 0.9 nmol of Arginine-tagged gold nanoparticles, prepared as described,[6] were combined with 0.45 nmol of EGFP to prepare EGFP/gold nanoparticle complexes. Particle sizes were evaluated with dynamic light scatting (DLS, Malvern).

Liposome Preparation

Azide-functionalized liposomes were prepared by thin film hydration techniques, as previously described.[7] The lipid film was composed of 58 mol% DPPC (1,2-dipalmitoyl-sn-glycero-3-phosphocholine), 40 mol% cholesterol, and 2 mol% azide-PEG_{2000}-DSPE (all lipids from Avanti). 0.5 mol% Top Fluor PC (1-palmitoyl-2-(dipyrrometheneboron difluoride) undecanoyl-sn-glycero-3-phosphocholine) was added to prepare fluorescent liposomes. 0.2 mol% DTPA-PE (1,2-distearoyl-sn-glycero-3-phosphoethanolamine-N-diethylenetriaminepentaacetic acid) was added to prepare liposomes with capacity for radiolabeling with ^{111}In. Lipid solutions in chloroform, at a total lipid concentration of 20 mM, were dried under nitrogen gas, then lyophilized for 2 hours to remove residual solvent. Dried lipid films were hydrated with Dulbecco's phosphate buffered saline (PBS). Lipid suspensions were passed through 3 freeze–thaw cycles using liquid N_2/50°C water bath then extruded through 200 nm cutoff track-etched polycarbonate filters in 10 cycles. DLS assessed particle size after extrusion and after each subsequent particle modification. Liposome concentration following extrusion was assessed with Nanosight nanoparticle tracking analysis (Malvern).

For conjugation to liposomes, rat IgG was modified with dibenzylcyclooctyne-PEG_4-NHS ester (DBCO, Jena Bioscience). IgG solutions (PBS) were adjusted to pH 8.3 with 1 M $NaHCO_3$ buffer and reacted with DBCO for 1 hour at room temperature at molar ratios of 2.5:1, 5:1, 10:1, or 20:1 DBCO:IgG. Unreacted DBCO was removed after reaction via centrifugal filtration against 10 kDa cutoff filters (Amicon). Efficiency of DBCO-IgG reaction was assessed optically, with absorbance at 280nm indicating IgG concentration and absorbance at 309nm indicating DBCO concentration. Spectral overlap of DBCO and IgG absorbance was noted by correcting absorbance at 280nm according to $Abs_{280C} = Abs_{280} - 1.089 \times Abs_{309}$. Molar IgG concentration was determined according to $[IgG] = \frac{Abs_{280C}}{\varepsilon_{280,IgG}}$, where $\varepsilon_{280,IgG}$ is the IgG extinction coefficient at 280 nm, 204,000 L mol^{-1}cm^{-1}. Molar DBCO concentration was determined according to $[DBCO] = \frac{Abs_{309}}{\varepsilon_{309,DBCO}}$, where $\varepsilon_{309,DBCO}$ is the DBCO extinction coefficient at 309 nm, 12,000 L mol^{-1}cm^{-1}. Number of DBCO per IgG was determined as the ratio $\frac{[DBCO]}{[IgG]}$. DBCO-modified IgG was incubated with azide liposomes at 200 IgG per liposome overnight at room temperature. Unreacted antibody was removed via size exclusion

chromatography, and purified liposomes were concentrated to original volume against centrifugal filters (Amicon).

Maleimide liposomes were also prepared via lipid film hydration.[8] Lipid films comprised 54% DPPC, 40% cholesterol, and 6% MPB-PE (1,2-dioleoyl-sn-glycero-3-phosphoethanolamine-N-[4-(p-maleimidophenyl) butyramide]), with lipids prepared, dried, resuspended, and extruded as described above for azide liposomes.

IgG was prepared for conjugation to maleimide liposomes by one-hour reaction of 10 SATA (N-succinimidyl S-acetylthioacetate) per IgG at room temperature in 0.5 mM EDTA in PBS. Unreacted SATA was removed from IgG by passage through 7 kDa cutoff gel filtration columns. SATA-conjugated IgG was deprotected by one-hour room temperature incubation in 0.05 M hydroxylamine in 2.5 mM EDTA in PBS. Excess hydroxylamine was removed and buffer was exchanged for 0.5 mM EDTA in PBS via 7 kDa cutoff gel filtration column. SATA-conjugated and deprotected IgG was added to liposomes at 200 IgG per liposomes for overnight reaction at 4°C. Excess IgG was removed by size exclusion column purification, as above for azide liposomes.

Polystyrene Nanoparticle Preparation

150 nm carboxylate nanoparticles (Phosphorex) were exchanged into 50 mM MES buffer at pH 5.2 via gel filtration column. N-Hydroxysulfosuccinimide (sulfo-NHS) was added to the particles at 0.275 mg/mL, prior to incubation for 3 minutes at room temperature. EDCI was then added to the particles at 0.1 mg/mL, prior to incubation for 15 minutes at room temperature. IgG was added to the particle mixture at 200 IgG per nanoparticle, prior to incubation for 3 hours at room temperature while vortexing. For radiotracing, ^{125}I-labeled IgG was added to the reaction at 5% of total IgG mass. The IgG/particle mixture was diluted with 10-fold volume excess of pH 5.2 MES buffer and the diluted mixture was centrifuged at 12000xg for 3 minutes. Supernatant was discarded and PBS with 0.05% BSA was added at desired volume before resuspending the particles via sonication probe sonication (three pulses, 30% amplitude). Particle size was assessed via DLS after resuspension, and particles were used immediately after DLS assessment.

Protein, Nanoparticle, and Bacteria Iodination

Protein, horse spleen ferritin nanocages (Sigma), or adeno-associated virus (empty capsids, serotype 8) were prepared in PBS at concentrations between 1 and 2 mg/mL in volumes between 100 and 200 μL. Films of oxidizing agent were prepared in borosilicate tubes by drying 300 μL of 0.5 mg/mL Iodogen (Perkin-Elmer, chloroform solution) under nitrogen gas. Alternatively, Iodobeads (Perkin-Elmer) were added to borosilicate tubes (one per reaction). Protein solutions were added to coated or bead-containing tubes before addition of Na$^{125/131}$I at 25 μCi per 100 μg of protein. Protein was incubated with radioiodine at room temperature for 5 minutes under parafilm in a ventilated hood. Iodide-protein reacottions were terminated by purifying protein solutions through a 7 kDa cutoff gel column (Zeba). Additional passages through gel filtration columns or against centrifugal filters (Amicon, 10 kDa cutoff) were employed to remove free iodine, assuring that >95% of radioactivity was associated with protein.

Lysozyme-dextran nanogels, crosslinked protein nanoparticles, *E. coli*, or adenovirus were similarly iodinated. At least 100 μL of particle suspension was added to a borosilicate tube containing two Iodobeads, prior to addition of 100 μCi of $Na^{125}I$ per 100 μL of suspension. Particles were incubated with radioiodine and Iodobeads for 30 minutes at room temperature, with gentle shaking every 10 minutes. To remove free iodine, particle suspensions were moved to a centrifuge tube, diluted in ~1 mL of buffer and centrifuged to pellet the particles (16000xg/30 minutes for nanogels, 16000xg/30 minutes for crosslinked protein particles, 10000xg/30 minutes for adenovirus, and 1000xg/10 minutes for *E. coli*). Supernatant was removed and wash/centrifugation cycles were repeated to assure >95% of radioactivity was associated with particles. Particles were resuspended by probe sonication (three pulses, 30% amplitude) for nanogels or crosslinked protein nanoparticles or pipetting for adenovirus or *E. coli*.

Nanoparticle Labeling with ^{111}In

^{111}In labeling of nanoparticles followed previously described methods, with adaptation for new particles.[7] All radiolabeling chelation reactions were performed using metal free conditions to prevent contaminating metals from interfering with chelation of ^{111}In by DTPA or DOTA. Metals were removed from buffers using Chelex 100 metal affinity resin (Biorad, Laboratories, Hercules CA).

Lysozyme-dextran nanogels were prepared for chelation to ^{111}In by conjugation to S-2-(4-Isothiocyanatobenzyl)-1,4,7,10-tetraazacyclododecane tetraacetic acid (p-SCN-Bn-DOTA, Macrocyclics). NGs were moved to metal free pH 8.3 1 M $NaHCO_3$ buffer by three-fold centrifugation (16000xg for 15 minutes) and pellet washing with metal free buffer. p-SCN-Bn-DOTA was added to NGs at 1:25 mass:mass ratio, prior to reaction for 30 minutes at room temperature. Free p-SCN-Bn-DOTA was removed by three-fold centrifugal filtration against 10 kDa cutoff centrifugal filters, with resuspension of nanogels in metal-free pH 4 citrate buffer after each centrifugation. Preparation of ^{111}In-labeled NGs is represented in schematic form in Supplementary Figure 31.

DOTA-conjugated nanogels or DTPA-containing liposomes in pH 4 citrate buffer were combined with $^{111}InCl_3$ for one-hour chelation at 37°C. Nanoparticle/$^{111}InCl_3$ mixtures were treated with free DTPA (1 mM final concentration) to remove ^{111}In not incorporated in nanoparticles. Efficiency of ^{111}In incorporation in nanoparticles was assessed by thin film chromatography (aluminum/silica strips, Sigma) with 10 μM EDTA mobile phase. Chromatography strips were divided between origin and mobile front and the two portions of the strip were analyzed in a gamma counter to assess nanoparticle-associated (origin) vs. free (mobile front) ^{111}In. Free ^{111}In was separated from nanoparticles by centrifugal filtration and nanoparticles were resuspended in PBS (liposomes) or saline (nanogels). For SPECT/CT imaging experiments (see *SPECT/CT Imaging* methods below) with nanogels, 80 μCi of ^{111}In-labeled nanogels, used within one day of ^{111}In labeling as described above, were administered to each mouse. For tracing ^{111}In-labeled liposomes in biodistribution studies, liposomes were labeled with 50 μCi ^{111}In per μmol of lipid.

Mass Spectrometry

Samples were analyzed on a QExactive HF mass spectrometer (Thermofisher) coupled with an Ultimate 3000 nano UPLC system and an EasySpray source. Peptides were separated by reverse phase (RP)-HPLC on an Easy-Spray RSLC C18 (2 μm) 75 μm inner diameter x 50 cm length column at 50°C. Mobile phase A consisted of 0.1% formic acid in water and mobile phase B of 0.1% formic acid in acetonitrile. Peptides were eluted into the mass spectrometer at 300 nL/min with each RP-LC run comprising a 95-minute gradient from 1 to 3% B in 5 min and 3-45% B in 90 min. The mass spectrometer was set to repetitively scan m/z from 300 to 1400 (R = 240,000) followed by data-dependent MS/MS scans on the twenty most abundant ions, minimum automatic gain control (AGC) 10^4, dynamic exclusion with a repeat count of 1, repeat duration of 30 s, (R=15000) and a normalized collision energy (NCE) of 27. Fourier transform mass spectrometry (FTMS) full scan AGC target value was $3x10^6$, while MS^n AGC was 10^5. MS^n injection time was 160 ms; microscans were set at one. Rejection of unassigned, 1, 6-8 and >8 charge states was set.

For online monitoring of the QExactive HF instrument, parallel reaction monitoring (PRM) analysis for the spiked-in iRT peptides was performed though Skyline AutoQC, and the data were uploaded and accessed in Skyline Panorama.[9] Meanwhile, as a measure for QC/QA, we injected standard E. coli protein digest in between samples (one injection after every four injections). The collected DDA data were analyzed in MaxQuant. The MaxQuant output was subsequently visualized using the PTXQC package to track the quality of the instrumentation.[10]

MS/MS raw files for the data dependent acquisition were searched against a reference mouse protein sequence database including reviewed isoforms from the Uniprot database using MaxQuant version 1.6.1.0. Trypsin was specified as enzyme with two possible missed cleavages. Carbamidomethyl of cysteine was specified as fixed modification and protein N-terminal acetylation and oxidation of methionine were considered variable modifications. The MS/MS tolerance FTMS was set to 20 ppm. False discovery rates were set to 1. The rest of search parameters were set to the default values.

Scaffold (Proteome Software) was used to validate MS/MS based peptide and protein identifications. Peptide identifications were accepted if they could be established at greater than 90.0% probability by the Scaffold Local FDR algorithm. Protein identifications were accepted if they could be established at greater than 95.0% probability and contained at least 1 identified peptide. Protein probabilities were assigned by the Protein Prophet algorithm.[11] Proteins that contained similar peptides and could not be differentiated based on MS/MS analysis alone were grouped to satisfy the principles of parsimony. Proteins sharing significant peptide evidence were grouped into clusters.

SPECT/CT Imaging

Thirty minutes after injection of 80 μCi of ^{111}In-labeled nanogels, anesthetized mice were sacrificed by cervical dislocation. Mice were placed into a MiLabs U-SPECT (Utrecht, Netherlands) scanner bed. A region covering the entire body was scanned for 90 min using listmode acquisition. The animal was then moved, while maintaining

position, to a MiLabs U-CT (Utrecht, Netherlands) for a full-body CT scan using default acquisition parameters (240 μA, 50 kVp, 75 ms exposure, 0.75° step with 480 projections). For naïve mice and mice imaged after cardiogenic pulmonary edema, CT data was acquired as above without SPECT data. The SPECT data was reconstructed using reconstruction software provided by the manufacturer, with 400 μm voxels. The CT data were reconstructed using reconstruction software provided by the manufacturer, with 100 μm voxels.

Background signal was removed from SPECT images by thresholding limits determined by applying Renyi entropic filtering, as implemented in ImageJ, to a SPECT image slice containing NG-associated ^{111}In in the liver. Background-subtracted pseudo-color SPECT images were overlayed on CT images and axial slices depicting lungs were selected for display, with CT thresholding set to emphasize negative contrast in the airspace of the lungs. ImageJ's built-in 3D modeling plugin was used to co-register background-subtracted pseudo-color SPECT images with CT images in three-dimensional reconstructions. CT image thresholding was set in the 3D modeling tool to depict skeletal structure alongside SPECT signal. For three-dimensional reconstructions of lung CT images, thresholding was set, as above, for contrast emphasizing the airspace of the lungs, with thresholding values standardized between different CT images (*i.e.* identical values were used for naïve and edematous lungs). Images were cropped in a cylinder to exclude the airspace outside of the animal, then contrast was inverted, allowing airspace to register bright CT signal and denser tissue to register as dark background. Three-dimensional reconstructions of the lung CT data, and co-registrations of SPECT data with lung CT data, were generated as above with ImageJ's 3D plugin applied to CT data cropped and partitioned for lung contrast. Quantification of CT attenuation employed ImageJ's measurement tool iteratively over axial slices, with measurement fields of view manually set to contain lungs and exclude surrounding tissue.

Effects of Nanoparticles in Nebulized LPS Model

To obtain bronchoalveolar lavage samples, mice were anesthetized with ketamine-xylazine (10 mg/kg ketamine, 100 mg/kg xylazine, intramuscular administration). The trachea was isolated and a tracheostomy was performed with a 22-gauge catheter. The mice were euthanized via exsanguination. 0.8 mL of cold BAL buffer (0.5 mM EDTA in PBS) was injected into the lungs over ~1 min via the tracheostomy and then aspirated from the lungs over ~1 min. Injections/aspirations were performed three times for a total of 2.4mL of fluid added to the lungs. Recovery of BAL fluid typically amounted to ~2.0mL.

BAL samples were centrifuged at 300xg for 4 minutes. The supernatant was collected and stored at -80°C for further analysis. Protein concentration was measured using Bio-Rad DC Protein Assay, per manufacturer's instructions. The cell pellet was fixed for flow cytometry as follows. 333 μL of 1.6% PFA in PBS was added to each sample. Samples were incubated in the dark at room temperature for 10 minutes, then 1 mL of BAL buffer was added. Samples were centrifuged at 400xg for 3min, the supernatant was aspirated, and 1 mL of FACS buffer (2% fetal calf serum and 1 mM

EDTA in PBS) was added. At this point, samples were stored at 4°C for up to 1 week prior to flow cytometry analysis.

For chemokine CXCL2 and cytokine IL-6 measurement in BALF, plasma, and lung and liver homogenates, lung and liver tissue were homogenized in 1 mL of PBS containing protease inhibitor cocktail (1×). Lysis buffer was added to tissue homogenates, BALF, or plasma, and the mixtures were incubated at 4°C for one hour. The lysate mixtures were centrifuged at 16000xg for 10 minutes at 4°C. CXCL2 and IL-6 were assessed in the natants with ELISA kits according to manufacturer protocols (DuoSet ELISA kits, R and D systems).

Software used in Acquisition and Analysis of Data

Flow cytometry data were acquired in BD Accuri C6 software. Histological imaging data were obtained with SlideBook 6 digital microscopy software. Gamma counter data were obtained as comma separated variable data tables through Perkin Elmer Wizard2 software. Dynamic light scattering and zeta potential data were collected in Malvern Zetasizer Nano software v3.30. Mass spectrometry data were obtained with Skyline AutoQC and Skyline Panorama. SPECT and CT data were obtained as NIFTI files with MIIabs integrated acquisition software. Ultraviolet/visible and fluorescence spectroscopy data were obtained with Molecular Devices Spectramax plate reader/spectrophotometer SoftMax Pro 7 control software. Circular dichroism spectra were obtained with Aviv control software v3.44.

Flow cytometry data were analyzed with FCS Express 6 Flow and FCS Express 7 Research. Histological, CT, and SPECT imaging data were processed in ImageJ (FIJI distribution, version 2.1.0/1.53c). Mass spectrometry data were analyzed in MaxQuant version 1.6.1.0 and Scaffold 4 with the Protein Prophet algorithm. Circular dichroism spectra were analyzed in CDNN (Circular Dichroism analysis using Neural Networks). All other data were saved as tabulated values in collection software (as listed above) for subsequent analysis in Microsoft Excel for Mac version 16.50. Bar, scatter, and line plots were all generated in Excel and arranged as figures in Microsoft PowerPoint for Mac version 16.50. Statistical analyses were performed in Excel using the Real Statistics Resource Pack and in GraphPad Prism 8. Principal component analysis and linear discriminant analysis were performed in Gnu Octave 6.1.0, using scripts adapted from https://www.bytefish.de/blog/pca_lda_with_gnu_octave/, and included below.

References (Supplementary Methods)

1. Li, J., Yu, S., Yao, P. & Jiang, M. Lysozyme-dextran core-shell nanogels prepared via a green process. *Langmuir* **24,** 3486–3492 (2008).
2. Myerson, J. W. *et al.* Flexible nanoparticles reach sterically obscured endothelial targets inaccessible to rigid nanoparticles. *Adv. Mater. Weinheim* **30,** e1802373 (2018).
3. Roh, K., Martin, D. C. & Lahann, J. Biphasic Janus particles with nanoscale anisotropy. *Nat. Mater.* **4,** 759–763 (2005).
4. Mout, R. *et al.* Direct Cytosolic Delivery of CRISPR/Cas9-Ribonucleoprotein for Efficient Gene Editing. *ACS Nano* **11,** 2452–2458 (2017).

5. Lee, Y.-W. *et al.* Direct Cytosolic Delivery of Proteins through Coengineering of Proteins and Polymeric Delivery Vehicles. *J. Am. Chem. Soc.* **142,** 4349–4355 (2020).
6. Lee, Y. *et al.* In Vivo Editing of Macrophages through Systemic Delivery of CRISPR-Cas9-Ribonucleoprotein-Nanoparticle Nanoassemblies. *Adv. Therap.* **2,** 1900041 (2019).
7. Hood, E. D. *et al.* Vascular Targeting of Radiolabeled Liposomes with Bio-Orthogonally Conjugated Ligands: Single Chain Fragments Provide Higher Specificity than Antibodies. *Bioconjug. Chem.* **29,** 3626–3637 (2018).
8. Hood, E. D. *et al.* Antioxidant protection by PECAM-targeted delivery of a novel NADPH-oxidase inhibitor to the endothelium in vitro and in vivo. *J. Control. Release* **163,** 161–169 (2012).
9. Bereman, M. S. *et al.* An Automated Pipeline to Monitor System Performance in Liquid Chromatography-Tandem Mass Spectrometry Proteomic Experiments. *J. Proteome Res.* **15,** 4763–4769 (2016).
10. Bielow, C., Mastrobuoni, G. & Kempa, S. Proteomics quality control: quality control software for maxquant results. *J. Proteome Res.* **15,** 777–787 (2016).
11. Nesvizhskii, A. I., Keller, A., Kolker, E. & Aebersold, R. A statistical model for identifying proteins by tandem mass spectrometry. *Anal. Chem.* **75,** 4646–4658 (2003).

Supplementary Table 1. *Zeta Potentials of Tested Nanoparticles*

	Zeta Potential	Standard Error
75nm NGs	7.1	0.5
130nm NGs	-0.3	0.1
200nm NGs	-0.2	0.2
275nm NGs	-0.4	0.1
Human Albumin NPs	-13.6	0.6
Bovine Albumin NPs	-11.2	0.5
Lysozyme NPs	-0.2	0.7
Hemoglobin NPs	-6.6	0.8
Transferrin NPs	-5.6	0.8
Bare Azide Liposomes	-2.2	0.2
SATA-IgG Liposomes	-2.1	0.5
D2.5-IgG Liposomes	-1.3	0.1
D5-IgG Liposomes	-1.2	0.1
D10-IgG Liposomes	-1.3	0.2
D20-IgG Liposomes	-4.1	0.2
IgG-PS Beads	-4.0	0.8
Au/eGFP NPs	-6.4	0.5

PONI/eGFP NPs	18.3	0.5
Horse Spleen Ferritin	-21.7	0.2
AAV	-9.2	Ref. 1
Adenovirus	-20	Ref. 2

Reference 1: Fein, D.E. et al. Cationic lipid formulations alter the *in vivo* tropism of AAV2/9 vector in lung. *Mol. Ther*. **17**, 2078-2087 (2009).
Reference 2: Kim, S.Y. et al. Electrostatic interaction of tumor-targeting adenoviruses with aminoclay acquires enhanced infectivity to tumor cells inside the bladder and has better cytotoxic activity. *Drug Deliv.* **25**, 49-58 (2018).

Supplementary Table 2. *Lysozyme-Dextran Nanogel and Crosslinked Albumin Nanoparticle Concentration in Lungs*

Nanoparticle Concentration in Lungs		
	Naïve	IV-LPS
Lysozyme-Dextran Nanogels	5.25 %ID/g	116.43 %ID/g
Albumin Nanoparticles	6.34 %ID/g	87.62 %ID/g

Supplementary Table 3. *Flow Cytometric Assessment of Nanoparticle Selectivity for Neutrophils*

	Proportion of Neutrophils Containing Nanoparticles		Proportion of Nanoparticle Uptake Accounted for by Neutrophils	
	Naïve	IV-LPS	Naive	IV-LPS
Lysozyme-Dextran Nanogels	18.5%	82.5%	49.2%	74.0%
Albumin Nanoparticles	11.4%	73.7%	50.6%	70.6%

Supplementary Table 4. *Lysozyme-Dextran Nanogel Variants: Selectivity for Injured Lungs*

Lysozyme-Dextran Nanogels: Enhancement of Lung Uptake Following Injury				
	75nm LDNGs	130nm LDNGs	200nm LDNGs	275nm LDNGs
Uptake in Injured Lungs	122.27 %ID/g	116.43 %ID/g	156.05 %ID/g	110.54 %ID/g
Lung Uptake (LPS):Lung Uptake (Naïve)	16.32	22.18	12.82	4.94

Supplementary Table 5. *Crosslinked Protein Nanoparticle Variants: Selectivity for Injured Lungs*

Crosslinked Protein Nanoparticles: Enhancement of Lung Uptake Following Injury					
	Human Albumin NPs	Human Albumin Nanorods	Bovine Albumin NPs	Human Hemoglobin NPs	Human Transferrin NPs
Uptake in Injured Lungs	87.62 %ID/g	117.82 %ID/g	39.42 %ID/g	27.98 %ID/g	16.73 %ID/g

Lung Uptake (LPS):Lung Uptake (Naïve)	13.82	18.91	10.16	3.23	3.17

Supplementary Table 6. *Viruses and Nanocages Lack Selectivity for Injured Lungs*

Viruses and Nanocages: No Enhancement of Lung Uptake Following Injury			
	Horse Spleen Ferritin	Adeno-Associated Virus	200nm LDNGs
Uptake in Injured Lungs	4.45 %ID/g	10.00 %ID/g	8.94 %ID/g
Lung Uptake (LPS):Lung Uptake (Naïve)	1.15	0.80	1.01

Supplementary Table 7. *Isolated Proteins Lack Selectivity for Injured Lungs*

Isolated Proteins: No Enhancement of Lung Uptake Following Injury			
	Bovine Serum Albumin	Hen Egg White Lysozyme	Human Transferrin
Uptake in Injured Lungs	9.22 %ID/g	8.92 %ID/g	9.69 %ID/g
Lung Uptake (LPS):Lung Uptake (Naïve)	1.19	1.31	1.10

Supplementary Table 8. *Cyclooctyne Copper-Free Click Chemistry Confers Immunoliposomes with Selectivity for Injured Lungs*

IgG Liposomes: Enhancement of Lung Uptake Following Injury for Copper-Free Click Liposomes			
	Bare Liposomes	SATA-IgG Liposomes	DBCO-IgG Liposomes
Uptake in Injured Lungs	16.89 %ID/g	22.26 %ID/g	117.16 %ID/g
Lung Uptake (LPS):Lung Uptake (Naïve)	1.14	1.63	11.89

Supplementary Table 9. *DBCO-IgG Liposome Selectivity for Injured Lungs is Dependent on Cyclooctyne Concentration*

Increasing DBCO:IgG = Increased Enhancement of DBCO-IgG Liposome Lung Uptake Following Injury				
	DBCO(2.5X)-IgG Liposomes	DBCO(5X)-IgG Liposomes	DBCO(10X)-IgG Liposomes	DBCO(20X)-IgG Liposomes
Uptake in Injured Lungs	16.91 %ID/g	17.79 %ID/g	31.35 %ID/g	117.16 %ID/g

Supplementary Table 10. *Flow Cytometric Assessment of DBCO-IgG Liposome Selectivity for Neutrophils*

Proportion of Neutrophils Containing DBCO-IgG Liposomes		Proportion of Liposome Uptake Accounted for by Neutrophils	
Naïve	IV-LPS	Naive	IV-LPS
9.7%	49.5%	48.4%	88.5%

Supplementary Table 11. *De-Identified Information on Transplant-Rejected Human Donor Lungs*

	Tracing #1	Tracing #2	Tracing #3	Tracing #4	Tracing #5	*In Vitro* #1	*In Vitro* #2	Histology #1
Age	71	47	17	63	76	60	17	69
Sex	F	M	F	F	F	M	F	F
COD	CVA/Brain Death	Unknown	Anoxia	CVA	CVA	Trauma	Anoxia	CVA/ICH

(COD: Cause of death, CVA: Cerebrovascular accident, ICH: Intracranial hemorrhage)

Supplementary Movie Legend

Supplementary Movie 1
Intravital Imaging of Lysozyme-Dextran Nanogel Uptake in IV-LPS-Injured Mouse Lungs.

Supplementary Movie 2
Three-Dimensional Reconstruction of Chest CT Images of Naïve Mouse Lungs.

Supplementary Movie 3
Three-Dimensional Reconstruction of Chest CT Images of Edematous Mouse Lungs.

Supplementary Movie 4
Three-Dimensional Reconstruction of SPECT-CT Imaging of Lysozyme-Dextran Nanogel Uptake in IV-LPS-Injured Mouse Lungs.

Supplementary Movie 5
Three-Dimensional Reconstruction of SPECT-CT Imaging of Lysozyme-Dextran Nanogel Uptake in Naïve Mouse Lungs.

Supplementary Movie 6
Three-Dimensional Reconstruction of SPECT-CT Imaging of Lysozyme-Dextran Nanogel Biodistribution in an IV-LPS-Injured Mouse.

Supplementary Movie 7
Three-Dimensional Reconstruction of SPECT-CT Imaging of Lysozyme-Dextran Nanogel Biodistribution in a Naïve Mouse.

4-Dimensional Linear Discriminant Analysis Gnu Octave Script

```
%Input of normalized/weighted LPS:naïve shift data, definition of nanoparticle classes
XCnorm_all;
C=[1;1;1;1;1;2;2;2;2;2;2;3;3;3;4;4;4;5;5;6;6;6;7;7;7;7];
```

```
dimension=columns(XCnorm_all);
labels=unique(C);
C_LDA=length(labels);
Sw_LDA=zeros(dimension, dimension);
Sb_LDA=zeros(dimension, dimension);
mu_LDA=mean(XCnorm_all);
for i=1:C_LDA
   Xi_LDA=XCnorm_all(find(C == labels(i)),:);
   n_LDA=rows(Xi_LDA);
   mu_i_LDA=mean(Xi_LDA);
   XMi_LDA=bsxfun(@minus,Xi_LDA,mu_i_LDA);
   Sw_LDA=Sw_LDA + (XMi_LDA'*XMi_LDA);
   MiM_LDA=mu_i_LDA-mu_LDA;
   Sb_LDA = Sb_LDA + n_LDA*MiM_LDA'*MiM_LDA;
endfor
[W_LDA,D_LDA]=eig(Sw_LDA\Sb_LDA);
[D_LDA,i]=sort(diag(D_LDA),'descend');

%Output of eigenvectors and eigenvalues
W_LDA = W_LDA(:,i);
W_LDA(:,1)
W_LDA(:,2)
W_LDA(:,3)
W_LDA(:,4)
D_LDA

%Output of data projections along the different eigenvectors
XCnorm_all_proj_LDA=XCnorm_all*W_LDA(:,1:4)';
XCnorm_all_proj_LDA(:,1)
XCnorm_all_proj_LDA(:,2)
XCnorm_all_proj_LDA(:,3)
XCnorm_all_proj_LDA(:,4)
```

2-Dimensional Principal Component Analysis Gnu Octave Script

```
%Input of normalized LPS biodistribution data
XLnorm;

%Determine eigenvectors of the covariance matrix
CLnorm=cov(XLnorm);
[V,D]=eig(CLnorm);
[D,i]=sort(diag(D),'descend');

%Output of eigenvectors and eigenvalues
```

V=V(:,i)
D
cumsum(D)/sum(D)

%Output of data projections along the different eigenvectors
*ZLnorm1=XLnorm*V(:,1);*
*ZLnorm2=XLnorm*V(:,2);*
*PLnorm1=ZLnorm1*V(:,1)';*
*PLnorm2=ZLnorm2*V(:,2)';*
PLnorm1(:,1)
PLnorm1(:,2)
PLnorm2(:,1)
PLnorm2(:,2)

Tabulated Analyses of Statistical Power for all Figures and Tables Containing Statements of Statistical Significance

Figure 1b: Comparison of 130nm NG Biodistributions in LPS+ and Naïve Mice

	Blood	Heart	Lungs	Liver	Spleen	Kidneys	Lungs:Liver
Power	0.00528963	0.8093402	0.99999443	0.00210252	0.00850434	0.99982557	1

Figure 1c: Comparison of ANP Biodistributions in LPS+ and Naïve Mice

	Blood	Heart	Lungs	Liver	Spleen	Kidneys	Lungs:Liver
Power	0.00466268	0.00964856	0.9999835	0.00439539	0.00149331	0.20380477	0.99983213

Figure 1g-h: Comparison of 130nm NG Flow Cytometry in LPS+ and Naïve Mice

	%Neutrophils that are NG+	%NG+ that are Neutrophils
Power	1	0.999998

Figure 1j-k: Comparison of ANP Flow Cytometry in LPS+ and Naïve Mice

	%Neutrophils that are ANP+	%ANP+ that are Neutrophils
Power	0.99993008	0.94183744

Figure 2a: Comparison of NG Biodistributions in LPS+ and Naïve Mice

75nm	Blood	Lungs	Liver
Power	0.66821582	1	0.99591295
130nm	Blood	Lungs	Liver
Power	0.00528963	0.99999443	0.00210252
200nm	Blood	Lungs	Liver
Power	0.81621681	0.99041658	0.56481419

Figure 2b: Comparison of Crosslinked Protein NP Biodistributions in LPS+ and Naïve Mice

HSA-NPs	Blood	Lungs	Liver
Power	0.00466268	0.9999835	0.00439539

HSA-Rods	Blood	Lungs	Liver
Power	0.07338989	0.99999772	0.86486499
BSA-NPs	Blood	Lungs	Liver
Power	0.00290356	0.9889909	0.00135207

Figure 2c: Comparison of Charge-Associated Protein NP Biodistributions in LPS+ and Naïve Mice

PONI/GFP	Blood	Lungs	Liver
Power	0.08010048	0.99951925	0.92964454
PONI/GFP	Blood	Lungs	Liver
Power	0.02449357	0.98936462	0.90568663
Au/GFP	Blood	Lungs	Liver
Power	0.2421965	0.99843531	0.00112121

Figure 2d: Comparison of Virus/Nanocage Biodistributions in LPS+ and Naïve Mice

Adenovirus	Blood	Lungs	Liver
Power	0.00102743	0.00119706	0.00134352
AAV	Blood	Lungs	Liver
Power	0.00355339	0.00224373	0.00570058
Ferritin	Blood	Lungs	Liver
Power	0.00919621	0.00941719	0.00415498

Figure 2e: Comparison of Liposome and Polystyrene Biodistributions in LPS+ and Naïve Mice

Bare Liposomes	Blood	Lungs	Liver
Power	0.35323013	0.01291866	0.42389764
PS NPs	Blood	Lungs	Liver
Power	0.01019452	0.17725013	0.00497605

Figure 3b: Comparison of Liposome Biodistributions in LPS+ Mice

DBCO-IgG vs. Bare	Blood	Heart	Lungs	Liver	Spleen	Kidneys
Power	1	0.96966111	0.99996718	0.6408312	0.00232251	0.00872313
DBCO-IgG vs. SATA-IgG	Blood	Heart	Lungs	Liver	Spleen	Kidneys
Power	0.43114948	0.0032429	0.99985651	0.04382646	0.32766418	0.00770372
SATA-IgG vs. Bare	Blood	Heart	Lungs	Liver	Spleen	Kidneys
Power	1	0.02121477	0.08514622	0.99995503	0.99999313	0.30882702

Figure 3e: Comparison of DBCO-IgG Liposome Flow Cytometry in LPS+ and Naive Mice

	%Neutrophils that are NP+	%NP+ that are Neutrophils
Power	0.99988974	1

Figure 3f: Comparison of Liposome Biodistributions in LPS+ Mice

DBCO(10x)-IgG vs. Bare	Blood	Heart	Lungs	Liver	Spleen	Kidneys

Power	0.99999999	0.96894207	0.88200879	1	0.99976936	0.01231404
DBCO(5x)-IgG vs. Bare	Blood	Heart	Lungs	Liver	Spleen	Kidneys
Power	0.99999998	0.03111932	0.001597	0.00102239	0.16219004	0.00145571
DBCO(2.5x)-IgG vs. Bare	Blood	Heart	Lungs	Liver	Spleen	Kidneys
Power	0.99999999	0.01139596	0.00100023	0.02960348	0.99998473	0.01836838

Figure 4a: NG Uptake in Neutrophils: Serum-free vs. Serum

Beta	3.0106E-76
Power	1

Figure 4d: NG Uptake in Neutrophils: Stimulated/Naïve in Untreated Serum vs. Heat- and Cobra Venom Factor-Treated Serum

	Untreated vs. HT	Untreated vs. CVF	Untreated vs. HT (Stimulated)	Untreated vs. CVF (Stimulated)
Beta	8.7824E-118	1.7165E-105	6.00809E-18	3.34314E-16
Power	1	1	1	1

Figure 4e/S31: Comparison of NG Biodistributions in LPS+ and LPS+/CVF+ Mice

	Blood	Heart	Lungs	Liver	Spleen	Kidneys	Lungs:Liver
Power	0.987768	0.7640914	0.95722868	0.25774063	0.79308198	0.03543638	0.9998527

Figure 5b: Comparison of NG Biodistributions in LPS+, Cardiogenic Pulmonary Edema, and Naïve Mice

LPS vs. Naive	Blood	Heart	Lungs	Liver	Spleen	Kidneys	Lungs:Liver
Power	0.81621681	0.02512977	0.99041658	0.56481419	0.24963289	0.70542484	0.93573661
CPE vs. Naive	Blood	Heart	Lungs	Liver	Spleen	Kidneys	Lungs:Liver
Power	0.00690011	0.00105798	0.00149282	1	0.44241089	0.01093827	0.02203619

Figure 6a: Comparison of NP Effects on Protein Extravasation in LPS Injury

DBCO-IgG Liposomes	vs. Naive	vs. Untreated	
Power	0.9904608	1	
NGs	vs. Naive	vs. Untreated	vs. DBCO-IgG Liposomes
Power	0.98810168	0.00173295	0.99205641
Bare Liposomes	vs. Naive	vs. Untreated	vs. DBCO-IgG Liposomes
Power	1	0.0366588	0.99999999

Figure 6b: Comparison of NP Effects on Leukocyte Extravasation in LPS Injury

DBCO-IgG Liposomes	vs. Naive	vs. Untreated	
Power	1	1	
NGs	vs. Naive	vs. Untreated	vs. DBCO-IgG Liposomes
Power	0.99783378	0.00186147	0.99022335
Bare Liposomes	vs. Naive	vs. Untreated	vs. DBCO-IgG Liposomes

Power	0.99994962	0.00903603	0.99398415

Figure 6e: DBCO-IgG Liposome Effects on BAL CXCL2 in LPS Injury

BALF	2.5 mg/kg vs. Untreated	5 mg/kg vs. Untreated	10 mg/kg vs. Untreated
Power	0.98907329	0.86065462	0.92611317

Figure 6f: DBCO-IgG Liposome Effects on Neutrophil Extravasation in LPS Injury

DBCO-IgG Liposomes	vs. Naive	vs. Untreated
Power	1	1

Figure 6g: DBCO-aICAM Liposome Effects on Neutrophil Margination in LPS Injury

Liposome-Treated (1h) vs. Naive	Blood	Heart	Lungs	Liver	Spleen	Kidneys
Power	0.99998423	0.96353264	0.99999988	0.44664206	0.76672348	0.99927243
Liposome-Treated (22h) vs. Naive	Blood	Heart	Lungs	Liver	Spleen	Kidneys
Power	0.69998083	0.89753738	0.01325182	0.38171644	0.0112917	0.99159168
Liposome-Treated (1h) vs. LPS	Blood	Heart	Lungs	Liver	Spleen	Kidneys
Power	0.58398514	0.34723289	0.95545809	0.20625804	0.97537578	0.99990716
Liposome-Treated (22h) vs. LPS	Blood	Heart	Lungs	Liver	Spleen	Kidneys
Power	0.99865224	0.09625872	0.99999993	0.87343798	0.06449908	0.9607995

Figure 6h: DBCO-IgG Liposome Effects on Circulating White Blood Cells in LPS Injury

Liposome-Treated vs. Untreated	Total WBCs	Lymphocytes	Monocytes	Neutrophils
Beta	0.03939388	1.1148E-05	0.96605884	0.63313776
Power	0.96060612	0.99998885	0.03394116	0.36686224
Liposome-Treated vs. Naive	Total WBCs	Lymphocytes	Monocytes	Neutrophils
Beta	0.01075886	0.00133611	0.97893733	0.0739337
Power	0.98924114	0.99866389	0.02106267	0.9260663

Figure S1a: Comparison of Ly6G Biodistributions in LPS+ and Naïve Mice

	Blood	Heart	Lungs	Liver	Spleen	Kidneys	Lungs:Liver
Power	0.993454907	0.157985468	1	0.19364082	0.00165543	0.146446368	0.9397812

Figure S1c: Comparison of Neutrophil Flow Cytometry in LPS+ and Naïve Mice

	%Leukocytes that are Neutrophils	%Neutrophils that are Intravascular
Power	0.99986283	0.99848333

Figure S3: Comparison of E. coli Biodistributions in LPS+ and Naïve Mice

	Blood	Heart	Lungs	Liver	Spleen	Kidneys	Lungs:Liver
Power	0.15899696	0.1450473	0.99993123	0.00331571	0.9999862	0.99940687	0.99998338

Figure S6a: Comparison of NG Flow Cytometry in LPS+ and Naïve Mice

Beta	2.9467E-05
Power	0.99997053

Figure S7a: Comparison of HSA NP Flow Cytometry in LPS+ and Naïve Mice

Beta	2.9467E-05
Power	0.99997053

Figure S7d-e: Comparison of Leukocyte Uptake of HSA NPs in LPS+ and Naïve Mice

HSA+ that are Leukocytes	
Power	0.00405935
Leukocytes that are HSA+	
Power	0.99999157

Figure S8: Comparison of NG Biodistributions in Intratracheal LPS and Naïve Mice

	Blood	Heart	Lungs	Liver	Spleen	Kidneys	Lungs:Liver
Power	0.93987775	0.19986467	0.95925659	0.75325915	0.6630986	0.93142032	0.9999999

Figure S9: Comparison of NG Biodistributions in Footpad LPS vs. Naïve Mice

LPS+ 24hrs	Blood	Heart	Lungs	Liver	Spleen	Kidneys
Power	0.48937476	0.11733971	1	0.00216054	0.99996763	0.99940991

LPS+ 24hrs	Upper Leg (Ipsi)	Upper Leg (Contra)	Knee (Ipsi)	Knee (Contra)	Tibia (Ipsi)	Tibia (Contra)	Foot (Ipsi)	Foot (Contra)
Power	0.20061865	0.17384965	0.81666813	0.99997735	0.9898568	0.90312874	1	0.53253318

LPS+ 6hrs	Blood	Heart	Lungs	Liver	Spleen	Kidneys
Power	0.03721648	0.07142114	0.57640231	0.01762129	0.29808061	0.33003797

LPS+ 6hrs	Upper Leg (Ipsi)	Upper Leg (Contra)	Knee (Ipsi)	Knee (Contra)	Tibia (Ipsi)	Tibia (Contra)	Foot (Ipsi)	Foot (Contra)
Power	0.90485329	0.30040207	0.09318698	0.01591801	0.00201613	0.00562408	0.0329617	0.03457304

Figure S10b-c: Comparison of NG Biodistributions in Footpad Complete Freund's Adjuvant vs. Naïve Mice

CFA vs. Sham	Blood	Heart	Lungs	Liver	Spleen	Kidneys
Power	0.22867351	0.18720872	0.05160349	0.05536088	0.04190037	0.28888144

CFA vs. Sham	Contra. Fore Paw	Ipsi. Fore Paw	Contra. Hind Paw	Ipsi. Hind Paw
Power	0.03178749	0.01067447	0.08095023	0.96199741

Figure S13: Comparison of NG Biodistributions in LPS+ and Naïve Mice

75nm	Blood	Heart	Lungs	Liver	Spleen	Kidneys	Lungs:Liver
Power	0.66821582	0.10726264	1	0.99591295	0.9779797	0.98944487	1
130nm	Blood	Heart	Lungs	Liver	Spleen	Kidneys	Lungs:Liver
Power	0.00528963	0.8093402	0.99999443	0.00210252	0.00850434	0.99982557	1

200nm	Blood	Heart	Lungs	Liver	Spleen	Kidneys	Lungs:Liver
Power	0.81621681	0.02512977	0.99041658	0.56481419	0.24963289	0.70542484	0.93573661
275nm	Blood	Heart	Lungs	Liver	Spleen	Kidneys	Lungs:Liver
Power	0.01590265	0.04667329	0.99708368	0.99999997	0.17174088	0.42971232	0.99492198

Figure S15: Comparison of Crosslinked Protein NP Biodistributions in LPS+ and Naïve Mice

HSA NPs	Blood	Heart	Lungs	Liver	Spleen	Kidneys	Lungs:Liver
Power	0.00466268	0.00964856	0.9999835	0.00439539	0.00149331	0.20380477	0.99983213
HSA Rods	Blood	Heart	Lungs	Liver	Spleen	Kidneys	Lungs:Liver
Power	0.07338989	1	0.99999772	0.86486499	0.00352142	0.00152545	0.99997218
BSA NPs	Blood	Heart	Lungs	Liver	Spleen	Kidneys	Lungs:Liver
Power	0.00401167	0.99999586	0.99998209	0.00153475	0.67061156	0.30384963	0.98871325
HgB NPs	Blood	Heart	Lungs	Liver	Spleen	Kidneys	Lungs:Liver
Power	0.0118408	0.01403062	1	0.00228487	1	0.00648095	0.99999201
Tf NPs	Blood	Heart	Lungs	Liver	Spleen	Kidneys	Lungs:Liver
Power	0.83026767	0.00288324	0.99999999	0.00441125	0.12673858	0.00100011	0.98524881
Lys NPs	Blood	Heart	Lungs	Liver	Spleen	Kidneys	Lungs:Liver
Power	0.00129181	0.00997496	0.08325438	0.00162263	0.00102644	0.04934747	0.04768237

Figure S16: Comparison of Charge-Associated Protein NP Biodistributions in LPS+ and Naïve Mice

PONI/GFP (PONI)	Blood	Heart	Lungs	Liver	Spleen	Kidneys	Lungs:Liver
Power	0.18196488	0.09698039	0.9975295	0.9968486	0.37645494	0.14410789	0.99939642
PONI/GFP (GFP)	Blood	Heart	Lungs	Liver	Spleen	Kidneys	Lungs:Liver
Power	0.05143594	0.30332193	0.99990261	0.99493751	0.75517703	0.84993086	0.99967955
Au/GFP	Blood	Heart	Lungs	Liver	Spleen	Kidneys	Lungs:Liver
Power	0.39862593	0.12337701	0.99996766	0.00118263	0.37247127	0.86571549	0.91084006

Figure S17: Comparison of Virus/Nanocage Biodistributions in LPS+ and Naïve Mice

Adenovirus	Blood	Heart	Lungs	Liver	Spleen	Kidneys	Lungs:Liver
Power	0.01009083	0.17076808	0.01064368	0.01110949	0.39134479	0.88355704	0.0108519
AAVs	Blood	Heart	Lungs	Liver	Spleen	Kidneys	Lungs:Liver
Power	0.03200513	0.02628936	0.02096988	0.04923224	0.14038055	0.05042992	0.01000106
AAVs	Blood	Heart	Lungs	Liver	Spleen	Kidneys	Lungs:Liver
Power	0.03200513	0.02628936	0.02096988	0.04923224	0.14038055	0.05042992	0.01000106

Figure S18: Comparison of Liposome and Polystyrene Biodistributions in LPS+ and Naïve Mice

Lipos	Blood	Heart	Lungs	Liver	Spleen	Kidneys	Lungs:Liver
Power	0.7664483	0.603527	0.00597361	0.39716382	1	0.02971236	0.08215525
IgG-PS	Blood	Heart	Lungs	Liver	Spleen	Kidneys	Lungs:Liver
Power	0.02552467	0.00735821	0.56508069	0.0102002	0.00284647	0.12070781	0.52984108

Figure S19: Comparison of Protein Biodistributions in LPS+ and Naïve Mice

BSA	Blood	Heart	Lungs	Liver	Spleen	Kidneys	Lungs:Liver
Power	0.04878318	0.0586952	0.23082316	0.86424694	0.03282261	0.6674331	0.04669254
Lys	Blood	Heart	Lungs	Liver	Spleen	Kidneys	Lungs:Liver
Power	0.95905364	0.56195022	0.74570017	0.00472479	0.2799422	0.7369454	0.53124905
Tf	Blood	Heart	Lungs	Liver	Spleen	Kidneys	Lungs:Liver
Power	0.00402365	0.16561543	0.00278414	0.37458209	0.02005868	0.57341139	0.00147074

Figure S20: Comparison of Liposome Biodistributions in Naïve Mice

SATA-IgG vs. Bare	Blood	Heart	Lungs	Liver	Spleen	Kidneys	Lungs:Liver
Power	1	0.98707342	0.96862641	1	0.98329866	0.93424489	1
DBCO-IgG vs. Bare	Blood	Heart	Lungs	Liver	Spleen	Kidneys	Lungs:Liver
Power	0.92526453	0.01879247	1	0.99995384	0.73072337	0.9997527	1

Figure S21: Comparison of Liposome Biodistributions in IT-LPS vs. Naïve Mice

IT-LPS + 1hrs	Blood	Heart	Lungs	Liver	Spleen	Kidneys	Lungs:Liver
Power	0.02871731	0.00638317	1	0.66723891	0.0031979	0.00126238	1
IT-LPS + 2hrs	Blood	Heart	Lungs	Liver	Spleen	Kidneys	Lungs:Liver
Power	0.02107885	0.00103302	1	0.04715089	0.11987468	0.03372982	0.99371093
IT-LPS + 6hrs	Blood	Heart	Lungs	Liver	Spleen	Kidneys	Lungs:Liver
Power	0.06095489	0.00393114	0.99999474	0.00205866	0.85226274	0.42811613	0.45967646

Figure S22a: Comparison of DBCO-IgG Liposome Lung Uptake via Flow Cytometry in LPS+ and Naïve Mice

Beta	0.00284954
Power	0.99715046

Figure S22d-e: Comparison of Leukocyte Uptake of DBCO-IgG Liposomes in LPS+ and Naïve Mice

NP+ that are Leukocytes	
Power	0.07464123
Leukocytes that are NP+	
Power	0.9171063

Figure S22f-g: Comparison of Endothelial Cell Uptake of DBCO-IgG Liposomes in LPS+ and Naïve Mice

NP+ that are Endothelia	
Power	0.01112316
Endothelia that are NP+	
Power	0.90335255

Figure S24: Comparison of DBCO-IgG Biodistributions in LPS+ and Naïve Mice

	Blood	Heart	Lungs	Liver	Spleen	Kidneys	Lungs:Liver
Power	0.00201824	0.12251791	0.00982638	0.00728957	0.00616453	0.00936788	0.02500038

Figure S29d: NG Uptake in Neutrophils: Stimulated/Naïve Neutrophils with Serum from CVF-Treated Mice Included

	Untreated Serum vs. CVF Mouse Serum	Untreated Serum vs. CVF Mouse Serum (Stimulated)
Beta	2.12904E-88	1.11901E-23
Power	1	1

Figure S30a: Mass Spectrometry Characterization of NG vs. Adenovirus Opsonins

NGs vs. Adenovirus	Complement C3	Spectrin α-chain	Spectrin β-chain	Complement C5	Filamin-A
Power	0.99890727	0.99996038	1	1	0.04591965
NGs vs. Adenovirus	Murinoglobulin-1	A-2-Macroglobulin	Complement C4	Serum Albumin	Inter α-Trypsin Inhibitor
Power	0.97183392	1	0.58718136	0.46398753	0.84734818

Figure S30b: Mass Spectrometry Characterization of NG vs. Adenovirus Opsonins

NGs vs. Adenovirus	Complement C3	Clathrin	Fibronectin; Anastellin	Stress-70 Protein	Endoplasmin
Power	0.99890727	1	0.50816729	1	1
NGs vs. Adenovirus	Filamin-A	Heat Shock Protein	Na/K-Transport ATPase	ATP Synthase	Trans. ER ATPase
Power	0.04591965	1	1	0.99999996	1

Figure S34e: Comparison of NG and Ferritin Uptake in Human Lungs

Beta	1.1679E-05
Power	0.99998832

Figure S37a: Comparison of NP Effects on Protein Extravasation in LPS Injury

DBCO-IgG Liposomes	vs. Naive	vs. Untreated	
Power	0.99907639	1	
NGs	vs. Naive	vs. Untreated	vs. DBCO-IgG Liposomes
Power	0.99130676	0.0719322	0.99526609
Bare Liposomes	vs. Naive	vs. Untreated	vs. DBCO-IgG Liposomes

Power	1	0.0374698	1

Figure S37b: Comparison of NP Effects on Leukocyte Extravasation in LPS Injury

Bare Liposomes	vs. Naive	vs. Untreated	vs. DBCO-IgG Liposomes
Power	1	0.0374698	1
NGs	vs. Naive	vs. Untreated	vs. DBCO-IgG Liposomes
Power	0.99784356	0.07809219	0.99740296
Bare Liposomes	vs. Naive	vs. Untreated	vs. DBCO-IgG Liposomes
Power	0.99995023	0.01792928	0.99949023

Figure S39: Comparison of DBCO-IgG Liposome Effects on CXCL2 in LPS Injury

BALF	2.5 mg/kg vs. Untreated	5 mg/kg vs. Untreated	10 mg/kg vs. Untreated
Power	0.98907329	0.86065462	0.92611317
Lung Tissue	2.5 mg/kg vs. Untreated	5 mg/kg vs. Untreated	10 mg/kg vs. Untreated
Power	0.05122364	0.05029888	0.83703331
Plasma	2.5 mg/kg vs. Untreated	5 mg/kg vs. Untreated	10 mg/kg vs. Untreated
Power	0.05110202	0.23664885	0.05141489
Liver	2.5 mg/kg vs. Untreated	5 mg/kg vs. Untreated	10 mg/kg vs. Vehicle
Power	0.77698414	0.91846908	0.98143887

Figure S40: Comparison of DBCO-IgG Liposome Effects on IL6 in LPS Injury

Liver	2.5 mg/kg vs. Untreated	5 mg/kg vs. Untreated	10 mg/kg vs. Vehicle
Power	0.77698414	0.91846908	0.98143887
Lung Tissue	2.5 mg/kg vs. Untreated	5 mg/kg vs. Untreated	10 mg/kg vs. Untreated
Power	0.83449129	0.07381842	0.23109819
Plasma	2.5 mg/kg vs. Untreated	5 mg/kg vs. Untreated	10 mg/kg vs. Untreated
Power	0.06616322	0.97624332	0.99999995
Liver	2.5 mg/kg vs. Untreated	5 mg/kg vs. Untreated	10 mg/kg vs. Untreated
Power	0.80797923	0.31122961	0.64479103

Figure S41a: Comparison of NP Effects on Neutrophil Extravasation in LPS Injury (%Protection)

DBCO-IgG Liposomes	vs. Naive	vs. Untreated	
Power	1	0.99999967	
NGs	vs. Naive	vs. Untreated	vs. DBCO-IgG Liposomes
Power	0.99826086	0.00163149	0.94750078
Bare Liposomes	vs. Naive	vs. Untreated	vs. DBCO-IgG Liposomes
Power	0.99996232	0.00463762	0.96511734

Figure S41b: Comparison of NP Effects on Neutrophil Extravasation in LPS Injury (#Neutrophils)

DBCO-IgG Liposomes	vs. Naive	vs. Untreated	
Power	1	0.99960446	
NGs	vs. Naive	vs. Untreated	vs. DBCO-IgG Liposomes
Power	0.99826607	0.04308019	0.99293619
Bare Liposomes	vs. Naive	vs. Untreated	vs. DBCO-IgG Liposomes
Power	0.99996262	0.0078601	0.99817174

Figure S43b: DBCO-IgG Liposome Effects on Circulating White Blood Cells in LPS Injury

Liposome-Treated (2.5 mg/kg) vs. Naive	Total WBCs	Lymphocytes	Monocytes	Neutrophils
Beta	0.68969925	0.23205375	0.96007391	0.9521151
Power	0.31030075	0.76794625	0.03992609	0.0478849
Liposome-Treated (2.5 mg/kg) vs. Untreated	Total WBCs	Lymphocytes	Monocytes	Neutrophils
Beta	0.7342137	0.62743934	0.98831079	0.89057393
Power	0.2657863	0.37256066	0.01168921	0.10942607

Liposome-Treated (5 mg/kg) vs. Naive	Total WBCs	Lymphocytes	Monocytes	Neutrophils
Beta	0.96566399	0.84853958	0.9764884	0.91301167
Power	0.03433601	0.15146042	0.0235116	0.08698833
Liposome-Treated (5 mg/kg) vs. Untreated	Total WBCs	Lymphocytes	Monocytes	Neutrophils
Beta	0.14048866	0.17257948	0.96913245	0.87647897
Power	0.85951134	0.82742052	0.03086755	0.12352103

Liposome-Treated (10 mg/kg) vs. Naive	Total WBCs	Lymphocytes	Monocytes	Neutrophils
Beta	0.03939388	1.1148E-05	0.96605884	0.63313776
Power	0.96060612	0.99998885	0.03394116	0.36686224
Liposome-Treated (10 mg/kg) vs. Untreated	Total WBCs	Lymphocytes	Monocytes	Neutrophils
Beta	0.01075886	0.00133611	0.97893733	0.0739337
Power	0.98924114	0.99866389	0.02106267	0.9260663

Figure S44b-c: DBCO-IgG Liposome Effects on Circulating Red Blood Cells and Platelets in LPS Injury

Liposome-Treated (2.5 mg/kg) vs. Naïve

	RBC	HGB	HCT	MCV	MCH	MCHC	RDWc
Power	0.01084551	0.01133225	0.01024778	0.01673992	0.01416344	0.01216472	0.17870213
	PLT	PCT	MPV	PDWc			
Power	0.02389947	0.01245942	0.12280932	0.03439994			

Liposome-Treated (2.5 mg/kg) vs. Untreated

	RBC	HGB	HCT	MCV	MCH	MCHC	RDWc
Power	1	0.9999999	0.999974	0.06022413	0.04352414	0.03164756	0.962072
	PLT	PCT	MPV	PDWc			
Power	0.95006649	0.80756897	0.06347932	0.01360276			

Liposome-Treated (5 mg/kg) vs. Naïve

	RBC	HGB	HCT	MCV	MCH	MCHC	RDWc
Power	0.01179895	0.01284706	0.01498471	0.03956763	0.01855163	0.02440735	0.02393594
	PLT	PCT	MPV	PDWc			
Power	0.05340269	0.03826795	0.06750852	0.02058134			

Liposome-Treated (5 mg/kg) vs. Untreated

	RBC	HGB	HCT	MCV	MCH	MCHC	RDWc
Power	0.99143875	0.99447586	0.91795359	0.09432179	0.01326841	0.07084098	0.51722861
	PLT	PCT	MPV	PDWc			
Power	0.99999997	0.99331618	0.03164756	0.01141309			

Liposome-Treated (10 mg/kg) vs. Naïve

	RBC	HGB	HCT	MCV	MCH	MCHC	RDWc
Power	0.02142702	0.02345856	0.01885281	0.01	0.10633192	0.10369666	0.01774077
	PLT	PCT	MPV	PDWc			
Power	0.11788942	0.06095334	0.41968648	0.07005327			

Liposome-Treated (10 mg/kg) vs. Untreated

	RBC	HGB	HCT	MCV	MCH	MCHC	RDWc
Power	0.76927798	0.75260519	0.54243344	0.03956763	0.42477681	0.93205702	0.11969078
	PLT	PCT	MPV	PDWc			
Power	1	0.99985492	0.09432179	0.01660054			